Combinatorial Study of Process Parameters, Microstructure and Mechanical Properties in Inconel 718 Parts Produced by Additive Manufacturing

Master Thesis
by
Sabine Bodner, BSc.

Department Materialphysics
Montanuniversität Leoben
Jahnstraße 12
8700 Leoben

This thesis was written in the cooperation with Resch GmbH, Glojach, Austria.

Leoben, November 2017

Affidavit / Eidesstattliche Erklärung

I declare in lieu of oath, that I wrote this thesis and performed the associated research myself, using only literature cited in this volume.

Ich erkläre an Eides statt, dass ich diese Arbeit selbständig verfasst, andere als die angegebenen Quellen und Hilfsmittel nicht benutzt und mich auch sonst keiner unerlaubten Hilfsmittel bedient habe.

Leoben, 17th November 2017 _____

Sabine Bodner

Matrikelnummer: 01135132

Acknowledgement

This thesis would not have been possible without the help of many people. Here I want to spend some words on them.

First, I want to thank my supervisor Assoc. Prof. Dr. Jozef Keckes. He provided his support in different ways. The encouragement of my ideas for this thesis and the kind of guidance to realize this work, motivated me from the initial to the final level in a unique way.

I acknowledge the great collaboration with Ing. Gerald Resch and his team. The manner of developing new ideas and techniques has been inspiring me since we've been working together.

Michael Meindlhumer and Dr. Juraj Todt supported me with their knowledge and provided their time and experience for discussion whenever I asked them. I am very grateful for their time.

I am grateful for the help of the people at Erich-Schmid-Institute in Leoben at some stage of my work. At this position I also would like to thank Bernhard Sartory from Materials Center Leoben.

This is also the right place to thank my friends, who I met during my time at the university. Throughout my studies we've passed good and tough times. Resi Rath, Christian Weindl, Peter Kronberger, Nadja Piskernik, Julia Winter, Julia Samer and Markus Alfreider– thank you for all the hours of studying, laughing and discussing together.
Beyond university there are Melanie, Emma, Nino and Carmen who are enriching my life.

Finally, I want to thank all the people, who were at my side some time in my life. I am glad to consider several people as my family. I thank my parents and my aunt in law for their encouragement.
I cannot find words to express my gratitude to my partner Markus and my daughter Elena. As they have been supporting me in an outstanding way for all the years, I want to dedicate this work to them.

Kurzfassung

Beim selektiven Laserschmelzen der Ni-Basis-Legierung Inconel 718, werden die funktionellen Eigenschaften der Bauteile durch eine Vielzahl von Prozessparametern beeinflusst. Diese Arbeit analysiert die Auswirkungen von Laserleistung, Scangeschwindigkeit und Schichtdicke auf die Oberflächenqualität, die Gefügeentwicklung, sowie die mechanischen Eigenschaften und die Eigenspannungsfelder. Zunächst wurden 41 Prozessparameterkombinationen mit Hilfe statistischer Versuchsplanung systematisch zusammengestellt. Dies bildete die Basis zur generativen Fertigung von Mikrozugproben. Die Auswertung der Daten zeigte einen komplexen Zusammenhang zwischen den Parametern und den gebauten Strukturen. Die mittleren Oberflächenrauigkeiten konnten auf bis zu 14µm für vertikale und unter 45° nach oben orientierte (upskin) Flächen, sowie bis zu 19µm für unter 45° nach unten orientierte (downskin) Flächen optimiert werden. Die maximalen Zugfestigkeiten der Proben im „wie gebaut“ Zustand, lag bei rund 670 MPa bei Bruchdehnungen von bis zu 33,5 %.

Basierend auf den Ergebnissen der Zugversuche wurden in einem weiteren Schritt sechs produktähnliche Geometrien erzeugt und an der Synchrotron Beamline P07 am DESY in Hamburg charakterisiert. Drei der Synchrotrongeometrien wurden unter konstanten Abscheidebedingungen synthetisiert. Bei den anderen drei Proben wurde die volumetrische Energiedichte während des Fertigungsprozesses variiert. Aus den Synchrotrondaten wurden die horizontalen und vertikalen Eigenspannungsverläufe ermittelt und der Texturverlauf in den Proben analysiert. Die Auswertungen ermöglichen neben der Charakterisierung der Zusammenhänge von Zugversuchsdaten, Synchrotronexperimenten und Gefügeuntersuchungen auch den Rückschluss auf die konkreten Einflüsse der einzelnen Parameterkombinationen.

So ergibt sich aus dieser Multiparameterstudie, dass es möglich ist, die funktionalen Eigenschaften innerhalb eines Produktes aus Inconel 718 im „wie gebaut“ Zustand alleine durch die Veränderung der Prozessbedingungen während des selektiven Laserschmelzens nach Bedarf anzupassen.

Schlagwörter:

generative Fertigung; additive Fertigung; selektives Laserschmelzen; Pulverbett; Inconel 718; Nickel-Basis Legierung; Eigenspannungsverlauf; statistische Versuchsplanung; Multiparameterstudie

Abstract

Functional properties of Ni-basis Inconel 718 alloy components synthetized using selective laser melting depend on a variety of process parameters. In this thesis, the effects of the laser power, the scanning velocity and the layer thickness on the surface quality, the mechanical properties, the microstructure and the residual stress gradients in a variety of as-built structures are analyzed.

Based on an experimental design schema, first, 41 process parameter combinations were systematically selected and applied to manufacture the structures. The combinatorial study has indicated complex correlations between the process and the sample parameters. Surfaces roughnesses were optimized to mean values of ~14 and 19 µm for vertical, 45°-upskin and 45°-downskin oriented surfaces, respectively. A maximal ultimate tensile strength of ~670 MPa and a strain at fracture of up to ~33.5 % were obtained in the as-built structures without further surface post-processing.

Secondly, the results were used to select representative conditions for the production of six near-product sample geometries, which were further analyzed at the synchrotron beamline P07 of DESY in Hamburg. Three specimens were produced using constant deposition conditions and, for another three geometries, the volumetric energy density was varied during the building process. Horizontal and vertical synchrotron scanning experiments were performed to characterize stress and texture evolutions across the samples.

The correlation of the experimental data allowed the understanding of the influence of the specific process parameters on the mechanical properties, the microstructure, the residual stress distributions and the surface quality. Finally, this multi-parameter study based on a variety of experimental techniques and applied process conditions demonstrate that it is actually possible to perform knowledge-based design of the functional properties and the corresponding microstructure of as-built components by applying purposefully selected input parameters during the additive manufacturing process.

Keywords:

additive manufacturing; selective laser melting; powder bed; Inconel 718; nickel-basis alloy; residual stress distribution; design of experiments; multi-parameter study

Table of Contents

1 Introduction 1
1.1 Manufacturing Processes 1
1.2 Additive manufacturing of metals 2
1.3 Inconel alloy 718 9
1.4 Initial situation of this work 9
1.5 Motivation of this work 10
1.6 Methodological procedure 10
1.7 Structure of this thesis 10

2 Experimental procedures 11
2.1 Sample manufacturing 11
2.1.1 Design of synthesis experiments 11
2.1.2 Additive Manufacturing of samples for tensile and synchrotron experiments 13
2.2 Measurement conditions 17
2.2.1 SEM analysis of the powder 17
2.2.2 Tensile tests 17
2.2.3 Synchrotron experiments 18
2.2.4 Laser microscopy and determination of surface roughness 18
2.2.5 Preparation of metallographic specimens 19
2.2.6 Hardness measurement 20
2.2.1 EBSD analysis 20

3 Theoretical Approach 21
3.1 Analysis of tensile test data 21
3.2 Evaluation of synchrotron data 23
3.2.1 Phase analysis 24
3.2.2 Texture analysis 25
3.2.3 Stress analysis 25
3.3 Analysis of the metallurgical sample preparation 27

4 Experimental Results and Discussion 30
4.1 Analysis of powder particle size and distribution 30
4.2 Additive manufacturing of tensile specimens 32
4.3 Roughnesses of 45° upskin, 45° downskin and vertical oriented surfaces 34
4.4 Tensile tests 40
4.4.1 Analysis of R_m, $R_{p0.2}$, A and E 40

4.4.2 Statistic impact of P, v and s on R_m 43
4.4.3 Influence of energy input on mechanical strength 45
4.5 Synchrotron experiments 48
4.5.1 Phase analysis 48
4.5.2 Horizontal and vertical stress distributions 50
4.5.3 Texture characteristics of the synchrotron samples 54
4.6 EBSD and EDX analysis 57
4.7 Correlation of the results 60

5 Conclusion 62

Table of Figures

Figure 1: A general classification of the manufacturing processes according to DIN 8580:2003-09 with examples. The second level presents the six main classes of the manufacturing processes. 1

Figure 2: Metal-based additive manufacturing techniques, classified by particular mechanisms of laser-metal interaction, based on [5]..... 3

Figure 3: A schematic diagram of a selective laser melting process. 5

Figure 4: Characteristic features of the SLM process. h represents the hatch distance, v the scanning velocity, s the layer thickness and P the laser power… 6

Figure 5: SEM micrograph shows the Inconel718 powder used in this thesis. Basic requirements for AM techniques are globular shape, small amount of satellites and narrow size distribution. 8

Figure 6: A schematic description of the experimental design scheme to optimize tensile strength, fracture strain and surface roughnesses. The input factors P, v and s were varied in 11, 9 and 3 levels. The region of full factorial analysis (cube) was limited to $\boldsymbol{p = jk = 33 = 27}$ samples… 12

Figure 7: Dimensions of the tensile sample's geometry. 14

Figure 8: Dimensions of the synchrotron sample's geometry. 15

Figure 9: A schematic sketch of the synchrotron specimen with VED gradient. The material with the parameter combination corresponding to the highest VED magnitude was deposited on the surface of the base plate. The VED magnitude decreases in Z-direction. 16

Figure 10: Micro-tensile test setup with a specimen in the center. 17

Figure 11: The additively manufactured structure was scanned 1 mm above the base plate horizontally and in the middle of the structure vertically with step sizes of 500 and 100 or 200 µm, respectively. 18

Figure 12: The load-displacement curve can be transformed into the stress-strain diagram with the characteristic $R_{p0.2}$, R_m, E and A parameters. 22

Figure 13: A schematic sketch of the experimental setup used for the synchrotron experiments. The x-ray beam diffraction on lattice planes within the polycrystalline AM structure results in the occurrence of Debye-Scherrer-rings on the 2D detector. 24

Figure 14: The radial and azimuthal integrations of the Debye-Scherrer-rings allow for the evaluations of phases (phase plot – 14a), strains and texture (texture plot – 14b). 25

Figure 15: Histogram of the size distribution and the corresponding SEM image of the raw powder (200 times magnified). 31

Figure 16: The variation of P, v and s lead to energy densities VED in the range of 5 to 87J/mm³. A small number beneath each symbol indicates its specific

VED. Different colors and symbols belong to different applied layer thicknesses: 20µm – green triangles; 50µm – red circles; 80µm – black squares. 32

Figure 17: Variation of VED resulted in visible differences in sample roughness. Specific combinations of different notch types and their positions enabled the identification of the specimens during the further experiments at any time. 33

Figure 18: A super position of a laser microscope image and the corresponding topographical analysis image. Yellow-greenish areas correspond to a neutral height level, blueish regions are lowered and reddish are elevated. This sample was produced with the second highest VED of 83 J/mm³. The built-direction is indicated by an arrow at the top of the image. 34

Figure 19: Main effects plot of average R_a values for the vertical surface roughness. The trend of this analysis indicates that an improvement in the surface quality can be obtained by high laser power, slow scanning velocity and small layer thickness, resulting in a higher VED. 36

Figure 20: Main effects plot of average R_a values for the upskin surface roughness. The trend of this analysis indicates that an improvement in the surface quality can be obtained by increasing the laser power, lowering scanning velocity and decreasing layer thickness, resulting in higher VED. 36

Figure 21: Main effects plot of average R_a values for the downskin surface roughness. The trend of this analysis indicates that an improvement in the surface quality can be obtained by decreasing the laser power, the layer thickness and therefore VED. 37

Figure 22: Interaction effects plot of average R_a values for the vertical surface roughness. The statistical analyses revealed, that these interactions are not significant. 38

Figure 23: Interaction effects plot of average R_a values for the 45° oriented upskin surface roughness. The statistical analyses revealed, that these interactions are not significant. 38

Figure 24: Interaction effects plot of average R_a values for the 45° oriented downskin surface roughness. The statistical analyses revealed, that these interactions are not significant. 39

Figure 25: Stress-strain plots of three test series of the specimens with the highest ductility (25a) and the maximum R_m (25b) and (25c) and maximum performance of R_m and A with only half of the time of production (25d). 41

Figure 26: Sequence of sample numbers with an average R_m of more than 550 MPa. The layer thicknesses s are indicated by different symbols and colours: 20 µm – green triangles; 50 µm – red circles; 80 µm – black squares. The sample numbers are written next to the symbols. 42

Figure 27: The main effect plot illustrates the response of the ultimate tensile strength on the variation of P, v and s. R_m increases with the increasing laser power and decreasing scanning velocity and layer thickness. 43

Figure 28: The almost parallel developments of the lines in the interaction effects plots indicate that the there is no significant interaction of the input factors. Also, the statistical analysis revealed that it is acceptable to interpret only the main effect diagram. 44

Figure 29: The one-dimensional, one-factor-at-time-test with a constant layer thickness of 50µm shows a non-linear progress of R_m. 45

Figure 30: The graphic course of R_m as a function of VED indicates, that the mechanical strength of a SLM part is strongly influenced by the VED during the deposition. The shape and size of the pores, illustrated by the representative optical microscopy images, allows for the correlation between the mechanical properties and reasonable VED range. Different symbols and colours identify the three layer thicknesses. ... 46

Figure 31: Phase plot from the sample S4 show the evolution of the diffraction peaks hkl as a function of the sample height Z. 49

Figure 32: Detail of the Inconel718 200 reflections obtained by in-plane(left) and out-of-plane Debye-Scherer-ring integrations as a function of the sample height. The peak-shift of the in-plane orientation is more pronounced, as the in-plane stresses acting along Y direction are dominant. 49

Figure 33: Horizontal stress distributions in Inconel718 structures that were deposited with one constant parameter set. Maximal compressive and tensile stresses are similar for the samples with the layer thickness of 20 µm (green triangles - parameter set of sample number 12) and the standard EOS-performance parameter set (s = 40 µm – blue dot-shells), whereas the sample produced with parameter set resulting in the maximal fracture strain (s=50 µm – red dots) shows the lowest tensile stress level from all synchrotron samples. 50

Figure 34: The stress dependencies obtained from the horizontal scanning experiments on Inconel718 gradient structures indicate the insufficient fusion of powder particles in the s = 80 µm structure (black squares). The stress distribution in the 20 µm gradient specimen (green triangles) differs from the course of the 50 µm structure (orange dots). 51

Figure 35: The vertical stress distributions across Inconel718 structures deposited using constant process parameters show a similar course for the standard EOS parameter set (blue dot-shells) and the set that indicated A_{max} (red dots). Stresses in sample number 12 (green triangles) remain relatively constant towards the top end of the structure. 52

Figure 36: The vertical stress profiles from the gradient structures should be interpreted with respect to texture measurements and horizontal stress profiles. 53

Figure 37: The course of the vertical stress distribution in the gradient structure of specimen S6 (corresponding to the sample produced with 20µm layer

thickness in Figure 34) documents the effect of the sample geometry. 54

Figure 38: Sample height dependent texture plots indicate the intensity distributions of 111 and 200 diffraction peaks of Inconel718 sample and document the presence of <100> fibre texture. 55

Figure 39: Texture plots of 200 diffraction peaks of the structures that were deposited with energy gradients and varying layer thicknesses of a) 20 µm, b) 50 µm and c) 80 µm. The degree of the preferred orientation depends on the energy input. The minor inner tick labels at the left edge of the images indicate the thresholds of the VED changes. 56

Figure 40: EBSD image and the corresponding inverse pole figure map of the interface between Inconel718 substrate and deposited structure in “as-built” condition. Within a transformation zone T, the orientation of the grains changes from random in the substrate to <100>-textured in the deposited structure. The building direction is indicated by arrows at the sides of the micrographs. 58

Figure 41: Overlay of an EBSD image with the inverse pole map of the SLM structure. If the energy input is high enough, large grains will grow epitaxially over several deposited layers. The building direction is indicated by an arrow. 59

Figure 42: EBSD image of a single layer junction recorded with a magnification of 10.000 times. Cb segregates at low angle grain boundaries in the preceding layers. The interface between the two layers is marked at the sides of the image by white curves. The building direction is indicated by an arrow. 59

Figure 43: Combined display of tensile test results (strain at fracture A in continuous black line and ultimate tensile strength R_m in dashed black line), Inconel718 200 diffraction peak texture analysis, hardness values and optical microscopy for the gradual sample deposited using a VED. The sample was produced using a constant layer thickness s = 20 µm, whereas laser power P and scanning velocity v were varied during the deposition. 61

Index of Tables

Table 1: Variation of input factors for experimental design scheme 12
Table 2: Additional process parameters used for the preparation of the specimens. These parameters were applied for all specimens. 14
Table 3: Parameter sets for the preparation of the synchrotron samples 16
Table 4: Parameter sets for the preparation of metallographic sections..... 19
Table 5: Ingredients of V2A-etchant. 20
Table 6: Nominal chemical composition of Inconel718 [12] 27
Table 7: Maximum, minimum and average values of the input factors P, v and s used to fabricate the tensile samples. 32
Table 8: Minimal and maximal mean roughnesses R_a for vertical, upskin and downskin oriented raw surfaces. 35

Index of Abbreviations

AM	Additive Manufacturing
CAD	Computer Aided Design
cf.	lat. “*confere*”
CLOM	Confocal Laser Optical Microscopy
DoE	Design of Experiments
EBSD	Electron Backscatter Diffraction
EDX	Energy Dispersive X-Ray Spectroscopy
EDM	Electrical Discharge Machining
Eq.	Equation
fcc	face centered cubic
hcp	hexagonal close packed
LM	Laser Melting
LS	Laser Sintering
MAM	Metal Additive Manufacturing
OM	Optical Microscopy
P	Laser Power
s	layer thickness
Sec.	Section
SEM	Scanning Electron Microscopy
SLM	Selective Laser Melting
T	base plate temperature
TCP	Topological Close Packed
v	scanning velocity
VED	Volumetric Energy Density
XRD	X-Ray Diffraction

1 Introduction

Additive manufacturing is the hypernym for a young manufacturing technique that is used to fabricate three dimensional products by a bottom up approach. The following section includes a short review of manufacturing processes in general, common additive manufacturing techniques for metals in detail and introduces terms and definitions. Typical properties of Inconel alloy 718, the material that was used for the production of the samples studied in this thesis, are described. Furthermore, the initial situation and the motivation are presented.

1.1 Manufacturing Processes

All manufacturing processes used in metal industry can be classified according to DIN 8580:2003-09. Beside techniques like thermoforming of polymers, blow moulding of glass and some methods to fabricate paper, six main classes of manufacturing are defined. Every production process in metal industry can be associated with one of these six classes.

Classification of different manufacturing processes is based on the cohesion mechanism of particles in a manufactured workpiece. The cohesion can either be

- created (primary shaping)
- maintained (forming)
- released (cutting) or
- increased (jointing, coating, changing substances properties) [1].

Referring to Ref [1], Figure 1 gives a review of the six main classes with some examples of the manufacturing processes.

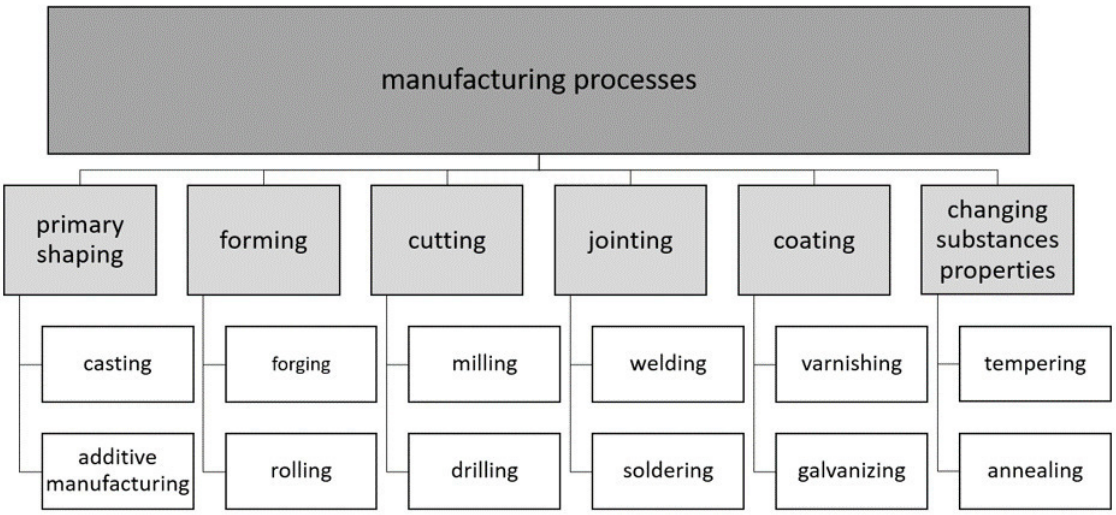

Figure 1: A general classification of the manufacturing processes according to DIN 8580:2003-09 with examples. The second level presents the six main classes of the manufacturing processes.

Another way of classifying manufacturing processes is the concept of how products are fabricated. One can distinguish between top-down versus bottom-up approaches.

Top-down processes are subtractive processes, in detail all forms of cutting like e.g. milling, turning, drilling and grinding. To gain the product, parts of a solid piece are selectively removed, until a desired geometrical shape is achieved.

Bottom-up processes represent the contrast to this way of parts production. Examples are all forms of primary shaping, jointing and coating.

Top-down products are fabricated at least in two production steps:

i) generation of a semi-finished product;
ii) further machining by top-down processes to reach the final shape.

As a result, it is obvious, that bottom-up processes like e.g. casting have a longer tradition in metal industry.

While the synthesis of functional components by controlled self-assembly of micro- and nanostructures is common in nature since ever, the fabrication of technological components using a bottom-up procedure is relatively young in metal industry. The manufacturing processes that are described below have been existing not even for 50 years.

1.2 Additive manufacturing of metals

As described in the previous section, the idea of producing parts by bottom up approach is not new. It was developed in the late 1970's in two dimensions and in the 1980's extended to three-dimensions. Other scopes like cartography (creation of architectural landscape models layer by layer) used bottom up building processes already since longer [2].

The selective building up of metal components by layer-by-layer deposition process required the application of additional techniques, which had not been available for long time – in particular automated systems controlled by computers. As a consequence, the technique of what we understand today as additive manufacturing (AM) or rapid prototyping (RP) can be considered as young.

It all began in the early 1970's, when researchers started to develop processes for the fabrication of printed circuits. It was the first time when metal layers were deposited selectively onto a base. This way of building up a desired part would not have been possible without computer-controlled machining.

AM techniques working with metals require the possibility to control the component dimensions using at least two-dimensional or usually three-dimensional computer-aided design (CAD) systems.

Furthermore, it was necessary to design suited laser systems. The method of selective laser sintering (SLS) was developed in the late 1980's in the USA and Germany. DTM Corporation and EOS GmbH offered the first additive manufacturing equipment for sale in 1993 and 1995, respectively [3].

Nowadays, several classifications of laser AM processes are known. Asides from the techniques, where the type of the basis material are sheets that are cut and stuck together layer by layer, or the processes, in which a 3D shape is gained by selectively 3D welding, the raw material for the techniques, that are discussed hereafter, are metal powders.

The main difference between the processes lies in the interaction of the laser and the metal powder [4], [5]. The chart in Figure 2 could be further extended to the left side by including other materials like plastics, that can be also produced by AM, or by including other energy sources, like electron beam- or arc welding- based technologies. To the right side, it could be extended, by including further subclasses of the presented techniques as described in more detail in [5].

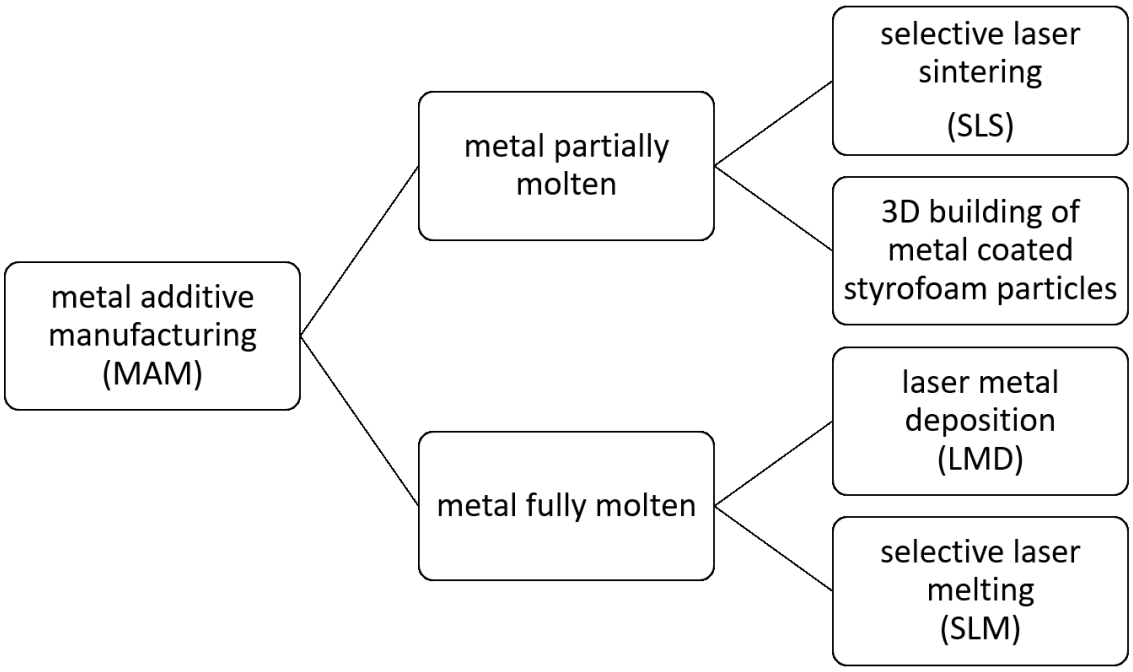

Figure 2: Metal-based additive manufacturing techniques, classified by particular mechanisms of laser-metal interaction, based on [5]

Laser sintering (LS) describes a synthesis technique, where in the first step, a powder is spread on a building platform, before it is being selectively laser sintered (SLS) layer by layer to build up a 3D workpiece shape. In contrast to the melting methods, the raw material is heated below the melting temperature in the case of the sintering processes. In a sintered solid, the metal particles adhere to each other, due to the diffusion driven processes occurring at the elevated (sintering) temperatures.

Another possibility to create sintered solids is the build-up of single, metal-coated styrofoam particles to a 3D shape by a robot assistance system. In the heating process, the sytrofoam burns away and the sintered metal shells built a cellular structure. The main advantages of these products are their low weight and specific mechanical properties, comparable with the metallic foams [6].

Metal powder is being molten completely in the laser melting (LM) and laser metal deposition (LMD) processes. In the latter technique, metal powder is fed via a coaxial

powder feed nozzle array directly into the laser beam, where it is molten. The 3D shape of the product is gained as the work piece is being moved by a computer-controlled driving system just below the powder interaction zone. A more detailed description of LS and LMD techniques with the explanation of further subclasses is provided in [5].

The investigated samples in this thesis were produced by a LM process, in particular by selective laser melting (SLM) of layer-by-layer deposited powder in a powder bed. Like the previously presented techniques, SLM allows for the production of three dimensional components. Their size is geometrically limited by the building volume of the device. Depending on the machine manufacturer, the actual generation of SLM machines offer building volumes from 60x60x30mm³ (DMP64 by 3D-Microprint, Germany) up to 1100x1100x0.3mm³ (Project A.T.L.A.S. by Concept Laser, Germany). The larger the building volume, the smaller is usually the building accuracy of the device.

Independent of the building volume, the SLM manufacturing process itself includes usually the following steps (see Figure 3):

a) The support plate moves down.
b) The recoating unit spreads the metal powder continuously all over the baseplate and the preceding layers.
c) The support plate moves up to the level that corresponds to the zero position minus the desired layer thickness.
d) In the recoating step, the coating unit removes the surplus powder in order to define the desired layer thickness.
e) By moving the mirror, the laser beam is being guided over the powder bed to melt a certain contour slice, according to the 3D CAD solid.
f) Subsequently, the procedure is being repeated from step 1.

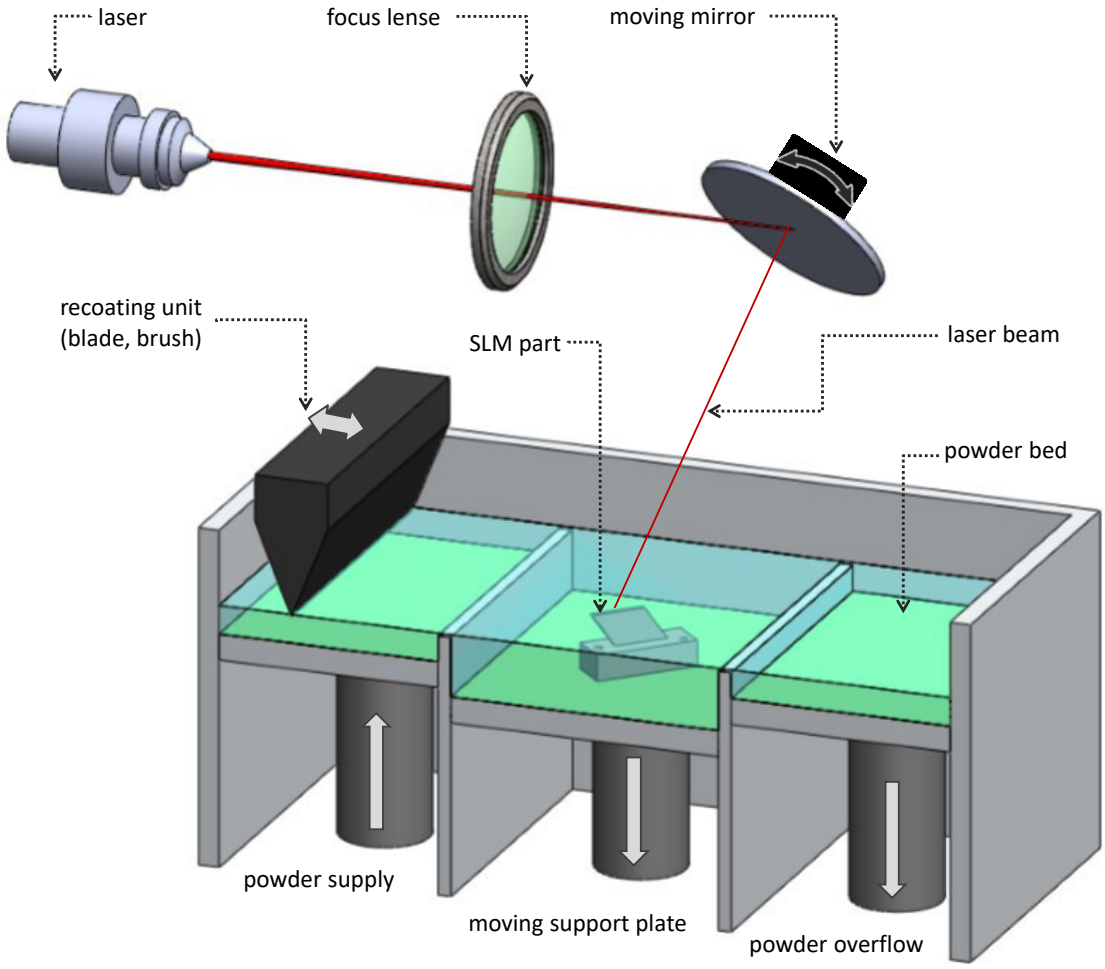

Figure 3: A schematic diagram of a selective laser melting process.

Before starting the building job, process parameters are at first assigned to the 3D CAD solid and then time dependent process data are transcribed to the SLM machine. Standard software usually enables the variation of the following process parameters (denoted in Sec. 3 as variable input factors):

- Heating temperature of the base plate T
- Laser power P
- Scanning velocity v
- Layer thickness s
- Hatch distance h
- Hatch style
- Number of performing lasers (for machines with more than one laser)

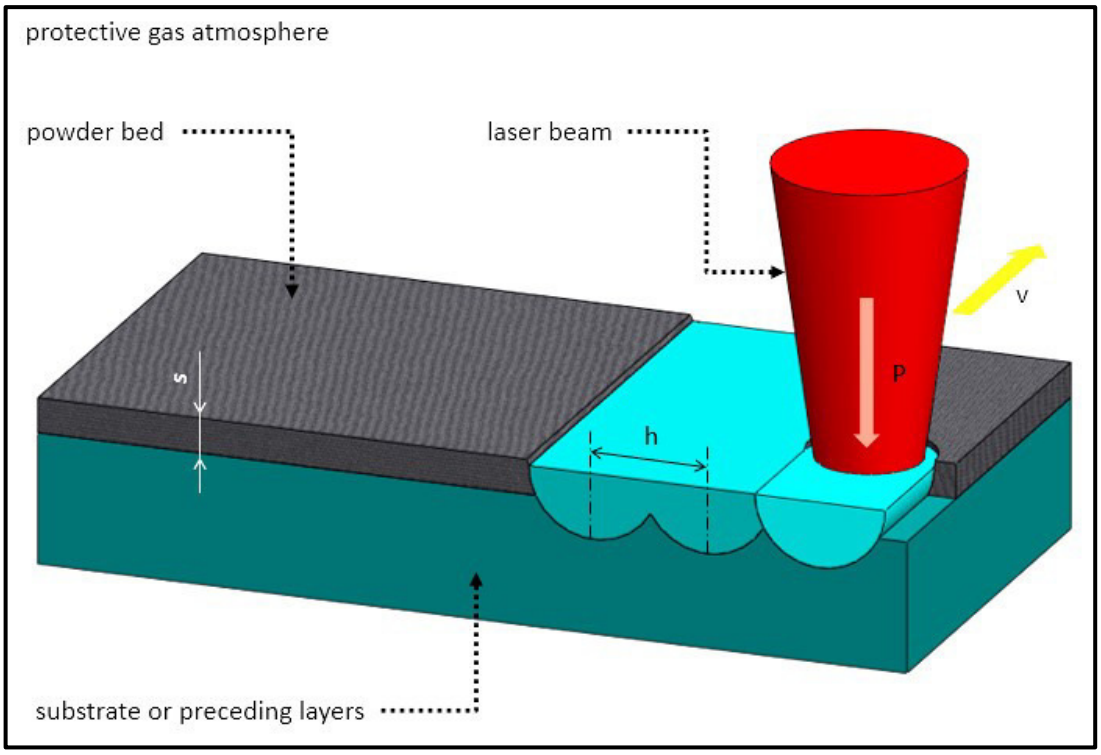

Figure 4: Characteristic features of the SLM process. *h* represents the hatch distance, *v* the scanning velocity, *s* the layer thickness and *P* the laser power.

The particulate parameters of the SLM process can significantly influence the microstructure and functional properties of the components. Hereafter, the mechanisms and the roles of the individual parameters are discussed. Figure 4 presents the process parameters, which influence is studied in this thesis.

Depending on the manufacturer of SLM equipment, currently it is possible to heat the base plate up to 550° Celsius (SLM Solutions Group AG, Germany). The actual *temperature T* of the base plate, however, influences the development of thermal residual stresses formed during the cooling down to the deposition temperature. Even if the base plate and the deposited material are the same, the temperature difference between the base plate substrate, the powder bed and the molten deposited material will result in the formation of a thermal gradient and thermal residual stresses. In certain materials, these stresses can be higher than the build-up yield stress and can result in an undesirable component plastic deformation.

The *laser power P* can be adapted for the material and regulated by the control software. Depending on the material, different types of lasers are being used, e.g. fiber lasers for metals (single fiber Ytterbium) and gas-lasers for polymers (CO_2). The laser wavelength used for metals is in the range of 1000nm (near infrared regime). A proper adjustment of the wavelength to the material, with respect to other influencing factors like temperature, would be a possibility to boost the efficiency factor of the equipment, especially for Al or Cu and their alloys [7].

Like the laser power, also the *scanning velocity v* influences the energy, that is transferred to the powder bed. Ref. [5] describes one possible method to estimate the volumetric energy density *VED* as follows

$$VED = \frac{P}{h \cdot v \cdot s} \quad (1)$$

The discussion on the reliability of this approximate formula is given in Sec. 4.4.3. The scanning is achieved by the movement of the scanner mirrors (Figure 4) and can be up to 11 m/s at commercial machines (TruPrint 3000 TRUMPF GmbH + Co. KG, Germany).

According to Eq. 1**,** another important process parameter is the layer thickness *s*. The quantity of *s* depends mainly on the particle size of the used powder. The applicable *s* range depends on the SLM device. For the production of highly precise features, the parameter *s* needs to be regulated with higher accuracy.

The distance between one and the next parallel laser lines is called hatch distance *h* (Figure 4). *h* predefines the ratio between the amount of the molten powder and the volume of the molten material, which was deposited in the previous step. Therefore, *h* influences decisively microstructural properties like formation of grain microstructure and precipitates.

The applied hatch style defines the patterns that are created when the laser screens the powder bed (Figure 4). Different patterns are selectable - from standard “line by line” or “back and forth” up to checkerboard pattern. [8] proved the influence of the hatch styles on built-up microstructure and residual stresses.

Actually, systems with up to four, simultaneously working lasers are currently available. The number of lasers reduces the building time and enables the larger building volumes. For some multi-laser equipments, it is also possible to switch between the laser types. The operator can choose for instance between a low-power and a high-power laser, but these lasers cannot work at the same time.

In addition to the above adjustable parameters, the following factors influence also the quality and result of the SLM process**.**

The *hatch rotation angle* between one and the following layer is expected to influence the development of residual stresses significantly. With EOS devices, the user can select between 0, 67 and 90 degrees hatch rotation angles, currently, however, particular values of 67 and 73 degrees are mainly used, e.g. with SLM Solutions GmbH device [9], [10]. In the parameter software from Renishaw plc. (Gloucestershire, UK), the hatch rotation angle can be set to any value. The influence of the hatch rotation angle was studied in [11].

Additionally, *protective gas* argon (Ar) and nitrogen (N), protect the molten bath against impurification by air-elements and remove deposits of vaporization.

Another parameter is the *powder quality*, which is predefined by the globularity of the particles, the amount of satellites and the particle size distribution (see Figure 5). The production of the powders used in AM production requires the use of dedicated routes, which differ from those used in the case of pressing and sintering. AM techniques need free-flowing, globular powders, whereas pressed parts require jagged powders with large surface so that the pinnacles hook together. Satellites lower the free-flowing and large

particle size distributions decrease the product's quality, because the fine particles are usually being burned during SLM.

The parameter of *powder humidity* promotes agglomeration and causes oxidation and hydration. Storing and handling of the powder in an Ar-atmosphere help to avoid this issue.

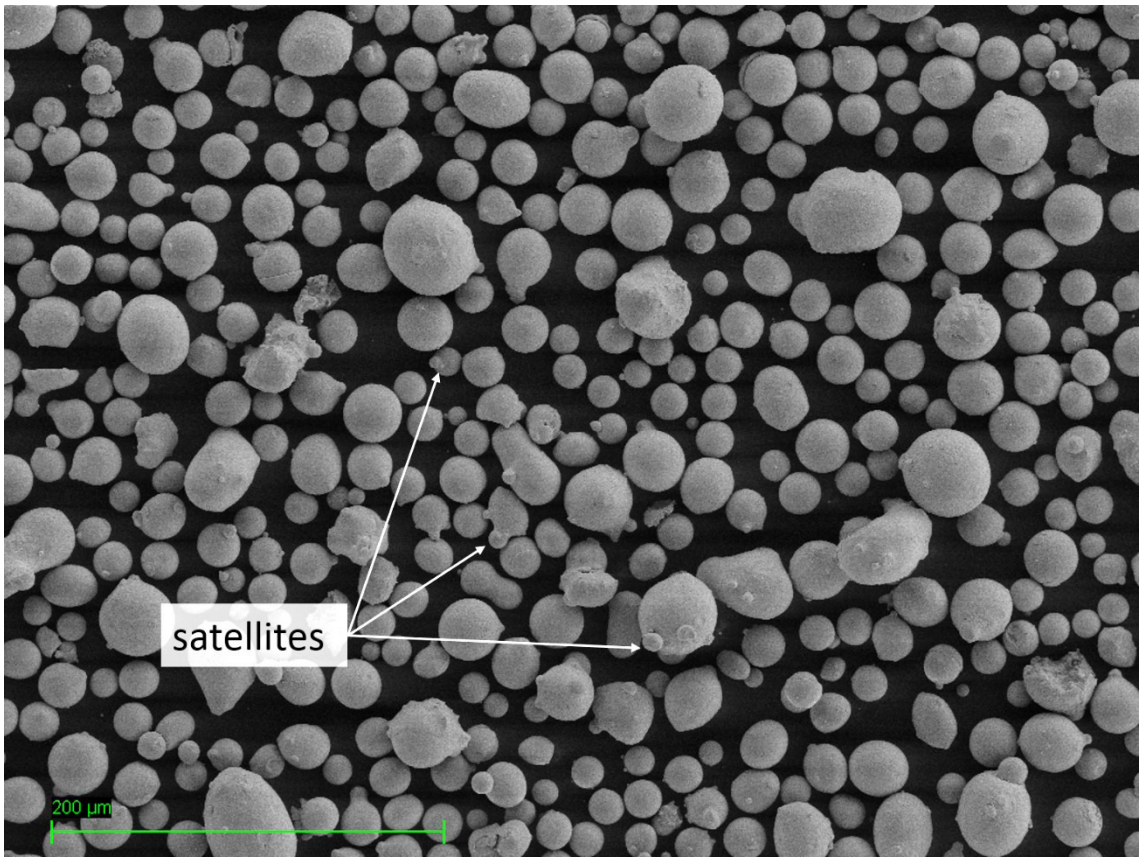

Figure 5: SEM micrograph shows the Inconel718 powder used in this thesis. Basic requirements for AM techniques are globular shape, small amount of satellites and narrow size distribution.

Asides from the technological parameters that can be quantitatively controlled by the operator, the production of complex components, especially with non-trivial geometry, requires an expert knowledge, e.g. in terms of placing the part appropriately in the machine's volume, the design and the disposition of supporting elements.

The functional properties of the components are however primarily defined by the material selection, from which of course also the applied process conditions must be defined. Actually, materials that are available for additive powder technologies by default are either pure metals or just standard wrought or cast alloys that were reprocessed to powders using different powdering techniques. State of the art is the metal additive manufacturing (MAM) of gold-, aluminum-, iron, copper-, titanium-, tungsten-, cobalt- and nickel-base pure metals and alloys, respectively [4]. Due to completely different process conditions (e.g. cooling rates of up to 10^{-6} K/s), the functional and microstructural properties of additively manufactured products differ from bulks, that were produced by standard technologies.

1.3 Inconel alloy 718

In this study, Inconel alloy 718, abbreviated as Inconel718 was used. Inconel718 is the trade name of a high-strength, corrosion resistant nickel-basis alloy, developed by Special Metals Corporation [12]. In 1978, it was available for the first time at the standard market, but had been used also before as an Apollo spacecraft material. Inconel718 has been known as “superalloy” due to its corrosion and creep resistance and structural stability up to 650°C. It is used nowadays in aerospace fields, jet engines, nuclear power reactors and in other high-temperature applications [13]. Products made of Inconel718 can be produced by casting, forging, cutting and welding processes.

1.4 Initial situation of this work

SLM devices are being sold, providing standard parameters for particular materials. While it is currently possible to produce parts with no or low residual stresses in Al-alloys, Inconel718 building-jobs are often interrupted because (i) support structures break and/or (ii) the produced parts deform as a result of residual stresses.

The main difficulty resides in the fact that the offered standard parameters, reflecting a wide range of customer demands, represent actually trade-off as far as the building time and the physical properties are considered. It is however necessary to optimize materials parameters for particular applications and to get a detailed understanding of the influence and interdependency of the process parameters, especially in terms of residual stresses.

1.5 Motivation of this work

In this thesis, the correlation between SLM manufacturing conditions, the properties of Inconel718 components and their microstructure is studied. Primarily, the influence and the interdependency of three adjustable parameters, laser power *P*, scanning velocity *v* and layer thickness *s* on mechanical properties, internal grain microstructure and residual stresses are evaluated.

One of the aims is to understand the formation of residual stresses formed during SLM manufacturing and to develop strategies to control them.

Another aim is the optimization of surfaces roughnesses for the following reasons:

i) Remachining of surfaces takes time and is cost-intensive.
ii) SLM allows for the design of 3D cellular structures. High surface roughness lowers the yield strength, especially in the tensile region due to notch effects. Whereas it is possible to refinish exterior surfaces of a product, surfaces of interior weight reducing, stabilizing grid structures cannot be corrected. Thus, improving the surface quality is essential to get maximum benefit of the enlarging possibilities of additive manufacturing.

1.6 Methodological procedure

Based on the EOS-standard parameters provided for core, skin, upskin, downskin and script of Inconel718-based components, an experimental design schema to vary *P*, *v* and *s* was developed. Tensile samples in 41 different process combinations were produced. Furthermore, six rhombic shaped geometries for the characterization of the residual stress by synchrotron radiation were manufactured. Analysis of the morphology by optical microscopy, hardness measurements and EDX/EBSD measurements completed this study on Inconel718 specimens in the as-build state.

1.7 Structure of this thesis

After this introduction, in Sec. 2 experimental procedures are presented. Sec. 3 introduces the theory of data evaluation. The results are presented and discussed in chapter 4. Milestones and highlights of this thesis are summarized in the conclusion.

2 Experimental procedures

The first section of this chapter describes the processing and the specimen's manufacturing. Afterwards, the measurement methods and conditions are introduced in section 2.2.

2.1 Sample manufacturing

Since several input factors (cf. Sec. 1.2) have an impact on the AM process, it was necessary to limit the number of process parameters, which were further applied in this thesis. The next task was to study the influence of these parameters on the specimens' properties.

2.1.1 Design of synthesis experiments

Arranging the synthesis experiment with the aid of statistical theory is a productive way to investigate a quality process, in which several influencing parameters affect the result. At a designed experiment, dedicated input parameters (factors) are selected in a first step. After this, these input factors are systematically modified to detect causes and effects of the modification. Input parameters can be generally classified in controllable and uncontrollable factors.

An experimental design is a schema that provides parameters combinations for the approach. The results are analysed using statistical analyses methods like the analysis of variances or regression. Thereby it is possible, to analyse the properties of the experimental design in terms of:

a) Determination of the most significant input factors and specification of the intervals of these factors to optimize the response variable.
b) Definition of the most influencing input factor magnitudes to minimize the response variable.
c) Predefinition of controllable factors in order to reduce the influence of the set of the uncontrollable factors.

Increasing the number of the analyzed input factors *j* and number of factor levels *k*, leads to an enlargement of the number of parameter combinations *p* by

$$p = j^k \tag{2}$$

As in this study three input factors *j* (laser power *P*, scanning velocity *v* and layer thickness *s*) were varied in three factor levels *k, p* is 27. Furthermore, *P* and *v* were varied in a larger interval – 11 levels for *P* and 9 levels for *v* - and only in one dimension while keeping *s* constant (cf. Figure 6). Thus, 41 tensile sample series of different parameter combinations were manufactured.

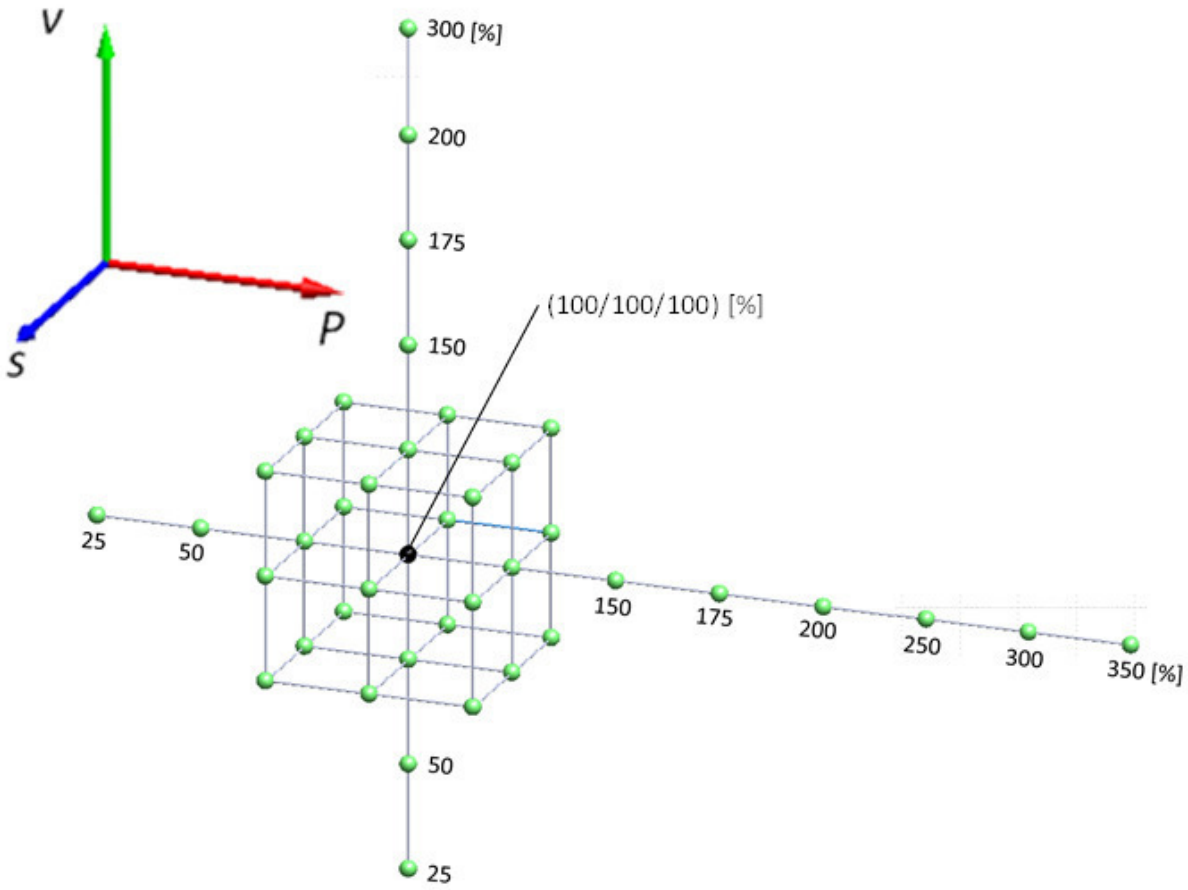

Figure 6: A schematic description of the experimental design scheme to optimize tensile strength, fracture strain and surface roughnesses. The input factors *P*, *v* and *s* were varied in 11, 9 and 3 levels. The region of full factorial analysis (cube) was limited to $p = j^k = 3^3 = 27$ samples.

Table 1 introduces absolute magnitudes of the process parameters, presented in the percentage scale in Figure 6. The values that were determined fully factorial (three-dimensional) are highlighted by a double frame. To cancel out statistical outliners, three test series of every parameter combination (repetitions) were produced and tested. Results of all tensile tests and surface roughness measurements were worked out using Minitab® software [14]. Each value was connected to a certain parameter combination. This allowed for the analysis of each parameter in terms of main effect (one-dimensional) and moreover in terms of interaction (3D) in the full factorial region.

Table 1: Variation of input factors for experimental design scheme

P		*v*		*s*	
%	W	%	mm/s	%	µm
25	25	25	240		
50	50	50	480		
75	75	75	720		

Resumption of Table 1: Variation of input factors for experimental design scheme

P		*v*		*s*	
100	**100**	**100**	**960**	**100**	**20**
125	125	125	1200	250	50
150	150	150	1440	400	80
175	175	175	1680		
200	200	200	1920		
250	250	300	2880		
300	300				
350	350				

2.1.2 Additive Manufacturing of samples for tensile and synchrotron experiments

In order to define the process parameters within the experimental design scheme, at first the standard parameter sets for Inconel718 provided by EOS were analysed. For this reason, from the various process parameter sets, minima, maxima and mean values were determined and then reasonable 100%-level quantities for *P* and *v* were selected. The 100% value of *s* was defined after the particle size and the size-distribution of the raw Inconel718 powder had been analysed. In Table 1, the row of 100% values and the corresponding figures for *P*, *v* and *s* are highlighted in bold.

The production of specimens was realized in two steps:

i) 41 × 3 (number of parameter combinations × number of test series) tensile specimens were prepared and tested
ii) based on the results of the tensile tests, synchrotron samples were fabricated.

Tensile and synchrotron samples were fabricated on an EOS 290M by Resch GmbH in Glojach, Austria. Until the processing, the raw Inconel718 powder had been stored in Ar-atmosphere to avoid moisture absorption.

Production of tensile specimens

The geometry of the tensile specimens is presented in Figure 7. The geometry was decided to be useful, as the results of the tensile tests were used to rank the different parameter sets among each other. Furthermore, the building height of these samples is low, compared to specimen's standards. This geometrical factor makes AM processes costly.

Specimens were built in vertical direction, with respect to the orientation of the Inconel718 base plate. The DoE predefined specific values for laser power, scanning velocity and layer thickness. Further parameters and the corresponding values for the

building jobs are presented in the Appendix. Altogether, 123 tensile samples were prepared.

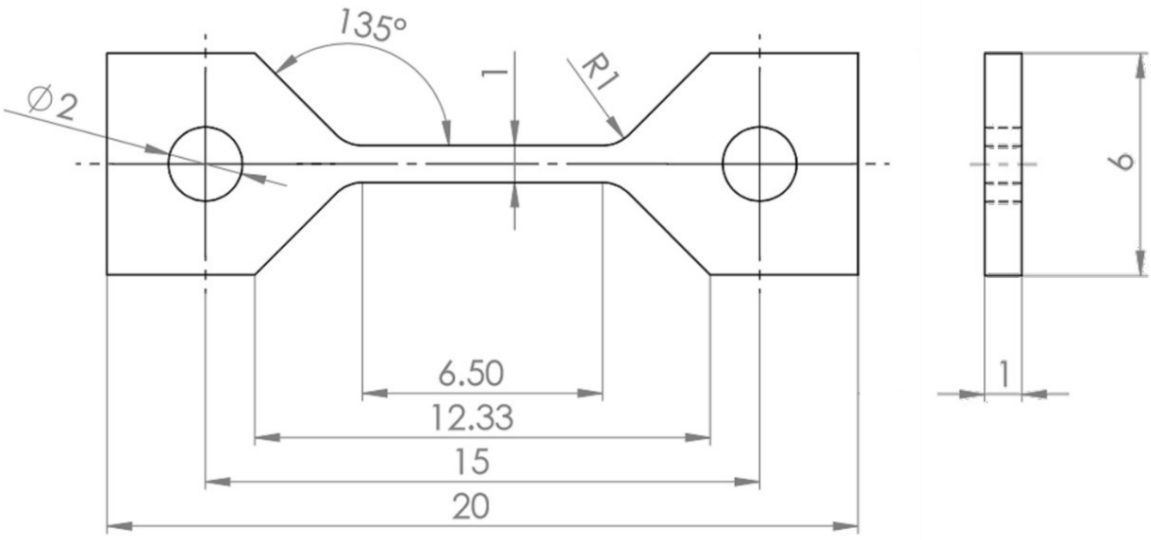

Figure 7: Dimensions of the tensile sample's geometry.

Table 2: Additional process parameters used for the preparation of the specimens. These parameters were applied for all specimens.

base plate temperature *T*	200° Celsius
hatch rotation angle	67 deg
hatch distance	0.1 mm
building orientation referred to the base plate	90 deg
hatch style	back and forth, no difference of skin and core, no contour
band width	5 mm
band overlap	0.12 mm
protective gas	argon
sample orientation on base plate referred to the recoating direction	60 deg
number of tensile samples, built in the same job	27 × 20 µm 69 × 50 µm 27 × 80 µm

Fabrication of synchrotron samples

The geometry of the synchrotron samples is presented in Figure 8. Two different types of synchrotron samples were considered:

i) samples built with constant process parameter magnitudes
ii) gradient samples built up with the varying energy density *VED* (Eq. 1), starting with the highest energy level at the surface of the base plate, decreasing the *VED* upwards (cf. Figure 9)

Like this, three homogenous and three gradient structures for the analysis by synchrotron radiation were prepared.

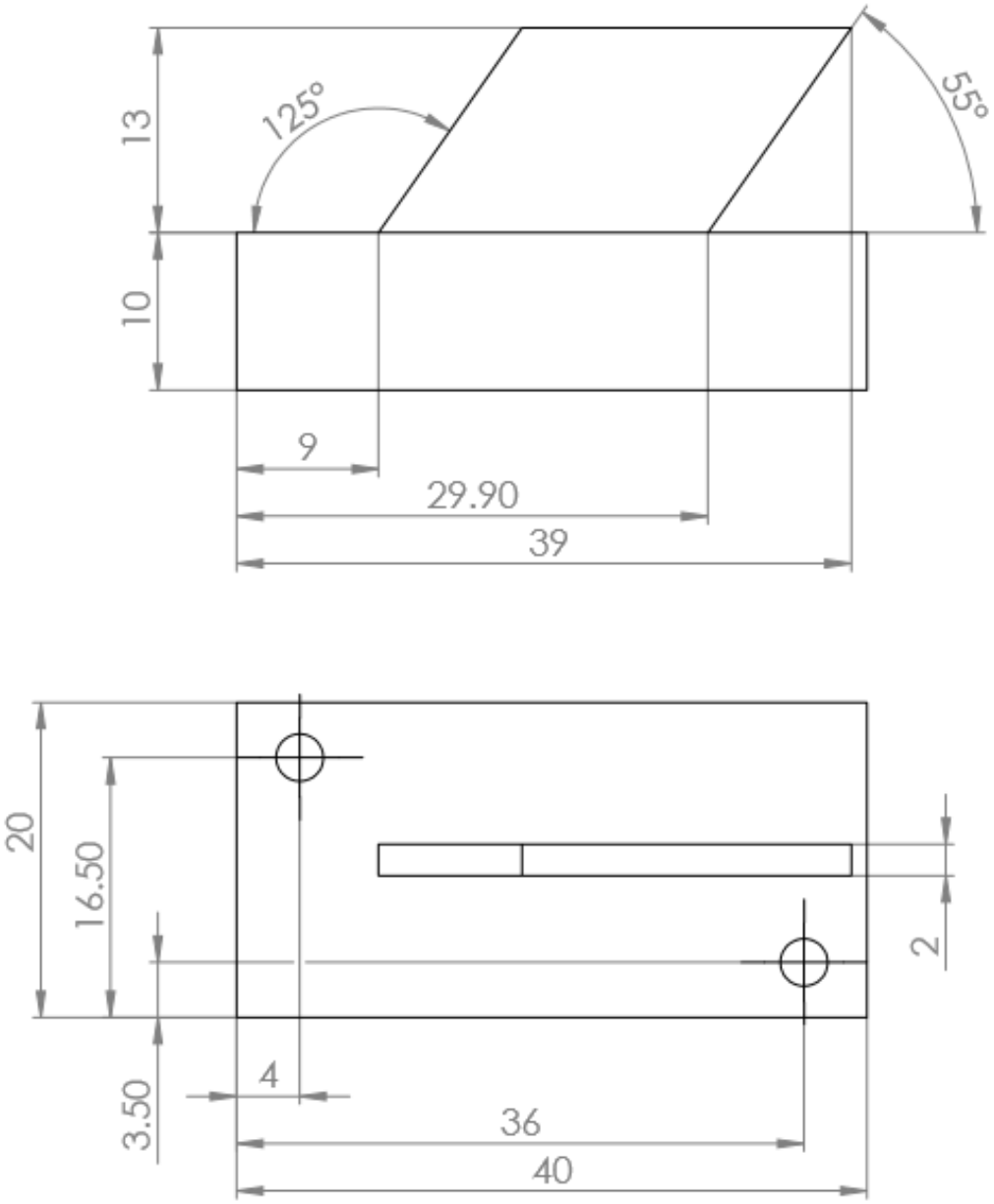

Figure 8: Dimensions of the synchrotron sample's geometry.

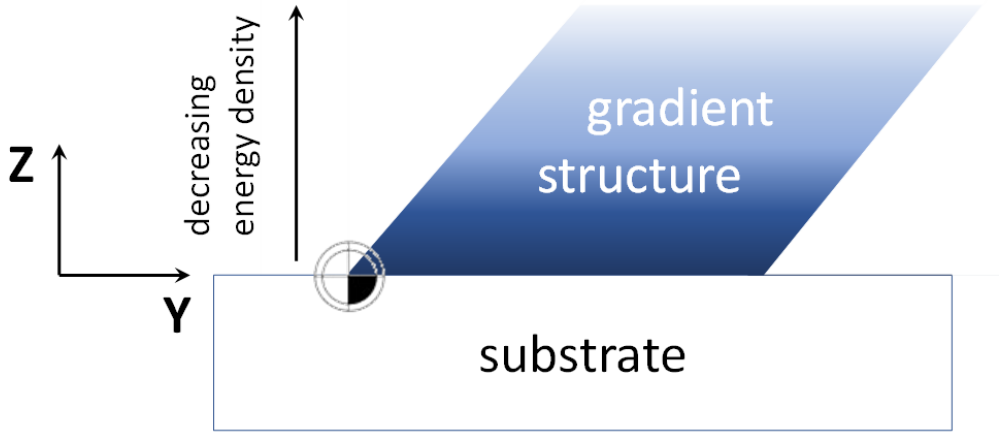

Figure 9: A schematic sketch of the synchrotron specimen with *VED* gradient. The material with the parameter combination corresponding to the highest *VED* magnitude was deposited on the surface of the base plate. The VED magnitude decreases in Z-direction.

The choice of the parameter sets that were used to produce the synchrotron samples was decided on the basis of the tensile tests results. Table 3 presents the parameter variations for *P*, *v* and *s* in detail. Except for sample S1, other parameters were kept constant, according to Table 2. Sample S1 was produced with the original EOS parameter set “Inconel718-performance”, including the contour.

Table 3: Parameter sets for the preparation of the synchrotron samples

sample number / short description of the sample	**laser power *P***	**scanning velocity *v***	**layer thickness *s***
	[W]	**[mm/s]**	**[µm]**
S1	285	960	40
standard parameters EOS (Inconel718 -performance)			
S4	125	960	20
max. ultimate tensile strength			
S5	100	240	50
max. strain at fracture			
S6	variable	variable	20
VED gradient structure			
S7	variable	variable	50
VED gradient structure			
S10	variable	variable	80
VED gradient structure			

2.2 Measurement conditions

This section describes the experimental setups and methods used in this thesis in detail.

2.2.1 SEM analysis of the powder

The used Inconel718 powder was analysed via scanning electron microscopy (SEM). Therefore, a small amount of the powder was stuck onto double coated carbon conductive taps and analysed in a Zeiss LEO1525 Gemini SEM system.

2.2.2 Tensile tests

Yield strength $R_{p0.2}$, ultimate tensile strength R_m and strain at fracture A were evaluated by tensile tests. The experiments were performed on a micro-tensile-test equipment from Kammrath&Weiss, Germany. Figure 10 illustrates the experimental setup.

Before mounting the specimens, the cross-section of each sample had been measured using an outside micrometre. After, the sample was inserted between a fixed and a movable jaw. Via two hard metal bolts, the force was transferred to the specimen. During the experiment, the traction speed was kept constant at 2.5 µm/s. Corresponding force and distance were recorded by a load cell and a position sensor, respectively. The signals were recorded by the supplied software of Kammrath&Weiss.

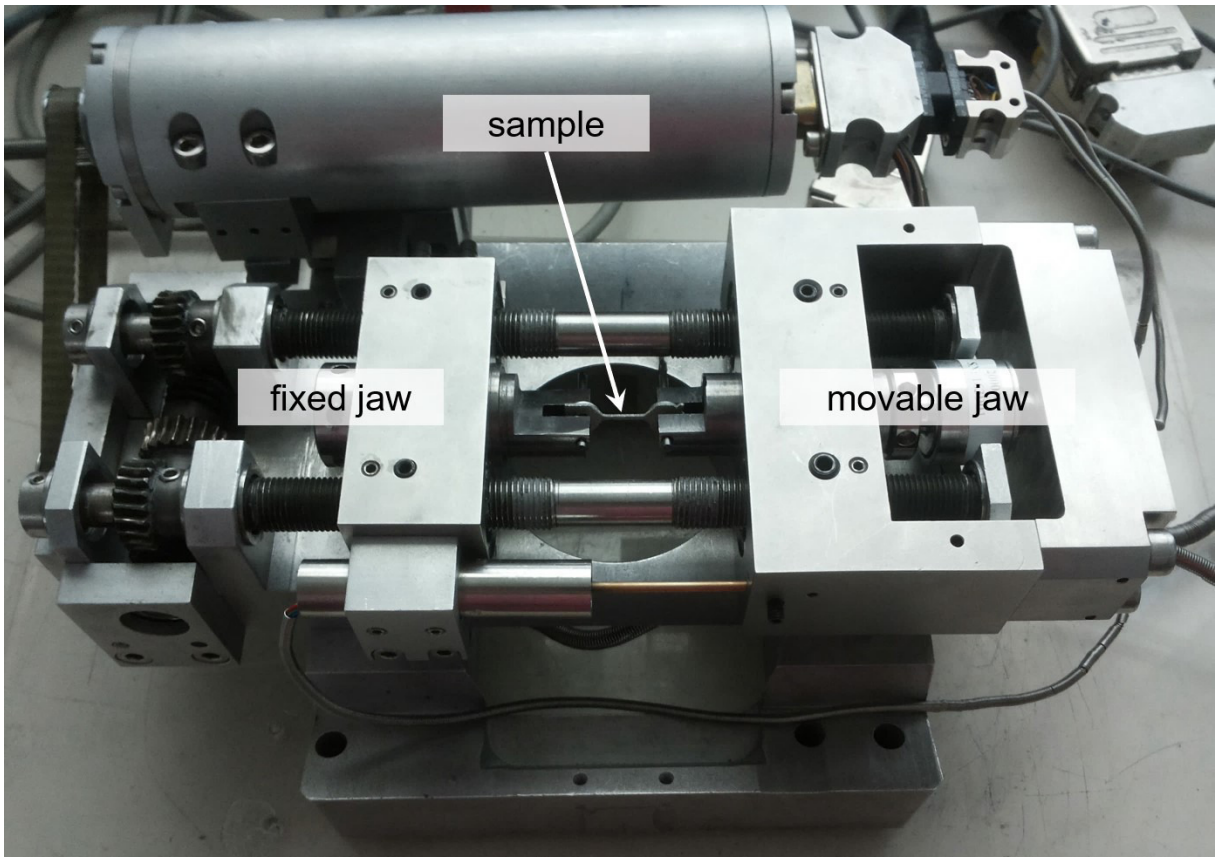

Figure 10: Micro-tensile test setup with a specimen in the center.

An Excel-macro was written to handle the collected data. The data points below a tensile load of 5 N were neglected and the respective path was set to 0. The recorded force-distance diagram was converted into a stress-strain diagram, using Eq. 3 and Eq. 4 that are valid for this one-dimensional experimental condition.

The value of maximum strain is the ultimate tensile strength R_m. The yield strength $R_{p0.2}$ was determined as the point of 0.2% of plastic deformation. The corresponding stress was evaluated by translating a linear fit parallel to an intersection with the point of 0.2% strain. For samples with R_m > 350 MPa, all data points in the range of 200-300 MPa were taken for the linear regression. For samples with R_m < 350 MPa, the linear fit based on the data point numbers between 300 and 500.

2.2.3 Synchrotron experiments

Synchrotron measurements were performed at the P07 side hutch of PETRA III in Hamburg. The samples were scanned in Z and Y directions (cf. Figure 11) by using a synchrotron radiation with a wavelength of 0.014235 nm. The size of the incident beam was set to 20 x 400 µm (in Z and Y directions). For the vertical scan, the scanning steps of 100 µm (sample ID S6, S7, S10) and 200µm (S1, S5, S4) were used, respectively. The point-to-point distance of the horizontal scan was 500 µm for all specimens. The data was analysed in terms of texture and stress distributions. The underlying theory of the analysis is explained in Sec. 3.2.

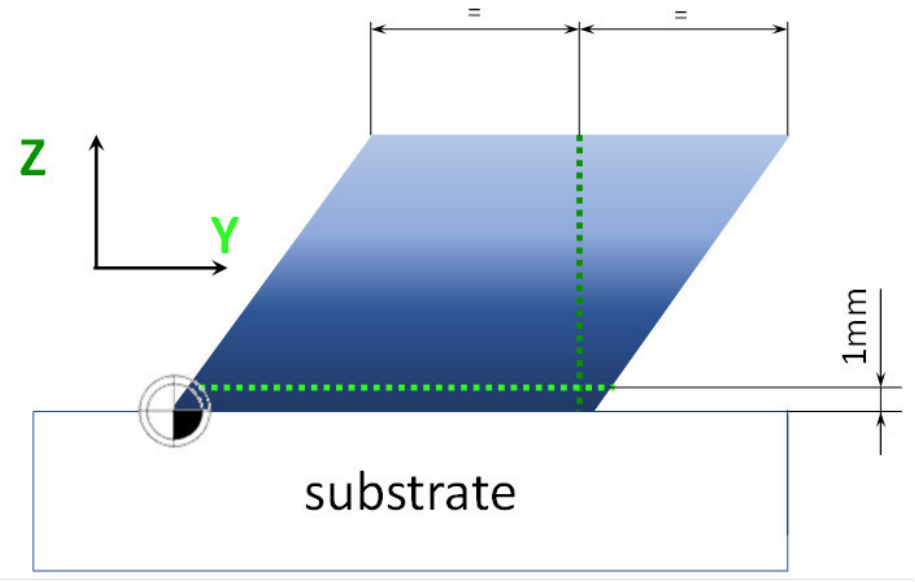

Figure 11: The additively manufactured structure was scanned 1 mm above the base plate horizontally and in the middle of the structure vertically with step sizes of 500 and 100 or 200 µm, respectively.

2.2.4 Laser microscopy and determination of surface roughness

The surfaces roughnesses of vertical, 45° upskin and 45° downskin oriented faces were scanned by an Olympus 3D measuring laser microscope LEXT OLS 4100 within a region of 642x642 µm². This microscope is equipped with a semiconductor laser (wavelength

405nm) and a photomultiplier detection system. The recorded data was analysed using the supplied Olympus software in terms of the average surface roughness magnitude.

2.2.5 Preparation of metallographic specimens

Individual tensile and synchrotron specimens were selected for further morphological investigations by optical microscopy. The samples were cold embedded in a conductive resin (EpoFix by Struers), manually grinded and automatically polished using a TegaPol 11 machine by Struers. The single steps are described in Table 4.

Table 4: Parameter sets for the preparation of metallographic sections

grinding	**grain size**	**r.p.m.**	**force**		**water cooling**	**direction of rotation**
	µm mesh-type	**[min^{-1}]**	**[N]**		**[-]**	**[-]**
	180	300	manually		on	synchronism
	220					
	320					
polishing	**disc type**	**r.p.m.**	**force**	**time**	**suspension**	
	[-]	**[min^{-1}]**	**[N]**	**[min]**	**[-]**	
	Largo	150	10	5.0	DiaPro All / Largo	
	Dac	150	10	5.0	DiaPro Dac	
	Nap	150	10	3.0	DiaPro Nap B	
	Chem	150	10	2.0	OP-S	
	Chem	150	10	1.0	water	

In the next step, the polished samples were etched according to Ref. [15]. Therefore, V2A-etchant (cf. Table 5) was heated up to 80°C and applied to the polished sample by wiping with a cotton ball for 80 to 100 seconds.

Table 5: Ingredients of V2A-etchant.

	ingredients	quantity
	[-]	[ml]
V2A-etchant	H_2O destillated	200
	HCl (37 %)	200
	HNO_3 (65 %)	20
	Dr. Vogels Sparbeize	0.6

2.2.6 Hardness measurement

Selected samples, after they were metallographically prepared, were characterized by hardness experiments. Hardness measurement scans were performed on a Mitutoyo/Buehler Micromet 5104 testing device. A test load of 300 grams - corresponding to $HV_{0.3}$ – was used to indent the metallographic section of the base plates and the AM structures. The experiments were performed, following the guidelines of DIN EN ISO 6507-1:2006. Consequently, the minimum distance between two indents as well as minimum distances to boarders were taken in account.

2.2.1 EBSD analysis

EBSD and EDX analyses were done for the synchrotron sample S6 at two positions:

i) interface of the substrate and the first layer (*VED* = 87 J/mm³)
ii) the structure deposited with *VED* = 69 J/mm³

The measurements were performed on an Auriga 40 scanning electron microscope (by Zeiss SMT), equipped with a Hikari Super EBSD camera and a EDX Apollo XPP with a resolution of up to 112 eV (both by EDAX).

3 Theoretical Approach

This chapter introduces the theoretical basis that is necessary to analyse the data of tensile tests, synchrotron experiments and the information of optical microscopy for structure analysis.

3.1 Analysis of tensile test data

The practice and analysis of tensile experiments are well known. Thus, in this section only the relevant points in stress-strain diagrams for the studied material Inconel718 are depicted.

From the tensile experiment load-displacement curves are acquired, which can be transformed to a stress-strain curve by applying Eqs. 3 and 4, as follows

$$\sigma = \frac{F}{S_0} \tag{3}$$

$$\varepsilon = \frac{\Delta l}{l_0} \tag{4}$$

Within these equations, σ is the stress, F the applied load, S_0 the initial cross section of the sample, ε the strain, Δl the elongation during the experiment, and l_0 the initial length of the specimen. Figure 12 presents a principle sketch of an engineering stress-strain diagram. The plot can be divided into three different sections.

Section I: Elastic deformation

In the section 1 of the stress-strain diagram (denoted in blue in Figure 12), the stress is linearly proportional to the applied strain. The deformation is reversible and thus, this is the region of elastic deformation.

As the stress distribution during tensile experiments complies with a one-dimensional deformation, the simplified form of Hooke's Law is valid (cf. Eq. 5).

$$\sigma_i = \varepsilon_i \cdot E_i \tag{5}$$

Eq. 5. denotes that the stress σ in direction i is the product of the strain ε in the same direction multiplied by the corresponding value of Young's modulus E. Thus, in the stress-strain diagram, the slope corresponds to E.

Section I in Figure 12 is limited by the transition from the elastic to the plastic region. One possible definition to specify an appropriate transition point for this type of stress-strain diagram is the yield strength $R_{p0.2}$. It can be obtained by translating a linear fit of the data points within Section I parallel along the strain-axis from the origin to 0.2% strain.

The corresponding stress at the intersection of the offset-fit and the stress-strain diagram is considered as the yield strength $R_{p0.2}$.

Section II: Proportional plastic deformation

Applying further mechanical strain results in hardening, that is usually caused by the generation of new dislocations. The irreversible plastic deformation is the effect of dislocation movement within the material. Dislocations are hindered in their movement because of precipitations, grain boundaries and increasing density of dislocations. Section II is limited by the ultimate strength R_m, that represents the maximum recorded stress in the stress-strain curve.

Section III: Necking

If the ultimate strength is exceeded, the measured force will usually decrease. As for engineering purposes it is assumed, that the cross section of the specimen does not change during the tensile test, according to Eq. 3, also the corresponding calculated stress decreases, even though in fact, the level of stress is still increasing.

The decrease of the force magnitude is the result of the effect of the geometrical strain softening, which represents local sample necking and the formation of vacancies and micropores and results in reducing the effective sample cross-section. Thus, the engineering stress-strain diagram differs from the true stress-strain curve.

Section III is limited by the point of fracture. The plastic deformation until the point of fracture is known as the value of the strain at fracture *A*.

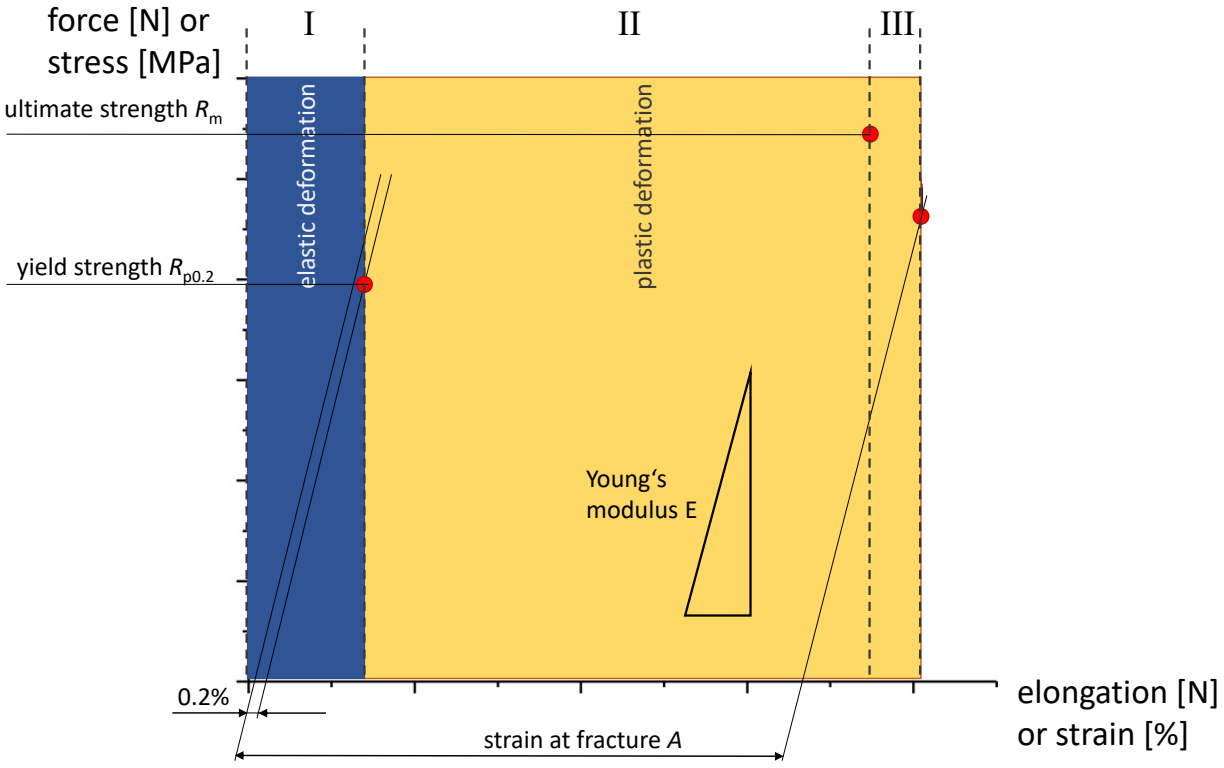

Figure 12: The load-displacement curve can be transformed into the stress-strain diagram with the characteristic $R_{p0.2}$, R_m, E and A parameters.

3.2 Evaluation of synchrotron data

During the synchrotron x-ray diffraction (XRD) experiments, high energetic x-ray photons are scattered elastically by the sample. Electromagnetic radiation with a wavelength λ comparable with the size of the objects can be used to measure the distances between these objects. Therefore, the distances between (*hkl*) crystallographic planes, lying in the sub-nm range, can be determined using the X-ray diffraction experiment.

In a crystalline material, the lattice planes are arranged periodically and the interaction of x-rays with matter will result in constructive interference described by Bragg's Law (Eq. 6).

$$2d_{hkl} \cdot sin\theta = n \cdot \lambda \quad \textbf{(6)}$$

where d_{hkl} is the distance between diffracting planes, θ is the Bragg's angle, n is an integer and λ stands for the wavelength of the x-rays.

Any external stress (due to e.g. external load) or residual stress (due to e.g. contraction of remelted zones at cooling during the SLM process) on the material leads to the deformation of the material and to changes in the lattice spacing d_{hkl}. Similarly, as in the case of macroscopic samples, the deformation will be linear-elastic and reversible, if the stress does not exceed the material's yield limit. Consequently, the distances d_{hkl} between diffracting planes will change accordingly. Therefore, synchrotron x-ray diffraction experiments can be used to determine direction-dependent magnitude of x-ray elastic strain in the material, which is actually *hkl* reflection dependent [16]. Subsequently, the strain data can be used to evaluate stress.

In an ideal polycrystalline material, there are theoretically infinitely many orientations of lattice planes. Again, every grain oriented favourably with a certain crystallographic plane fulfilling Bragg's condition diffracts X-rays, which can be recorded by the detector. Measuring the diffracted signal with a 2D detector leads to the observation of Debye-Scherrer-rings (see Figure 13). The Debye-Scherrer-rings contain information on sample composition, microstructure and residual stresses, as discussed below.

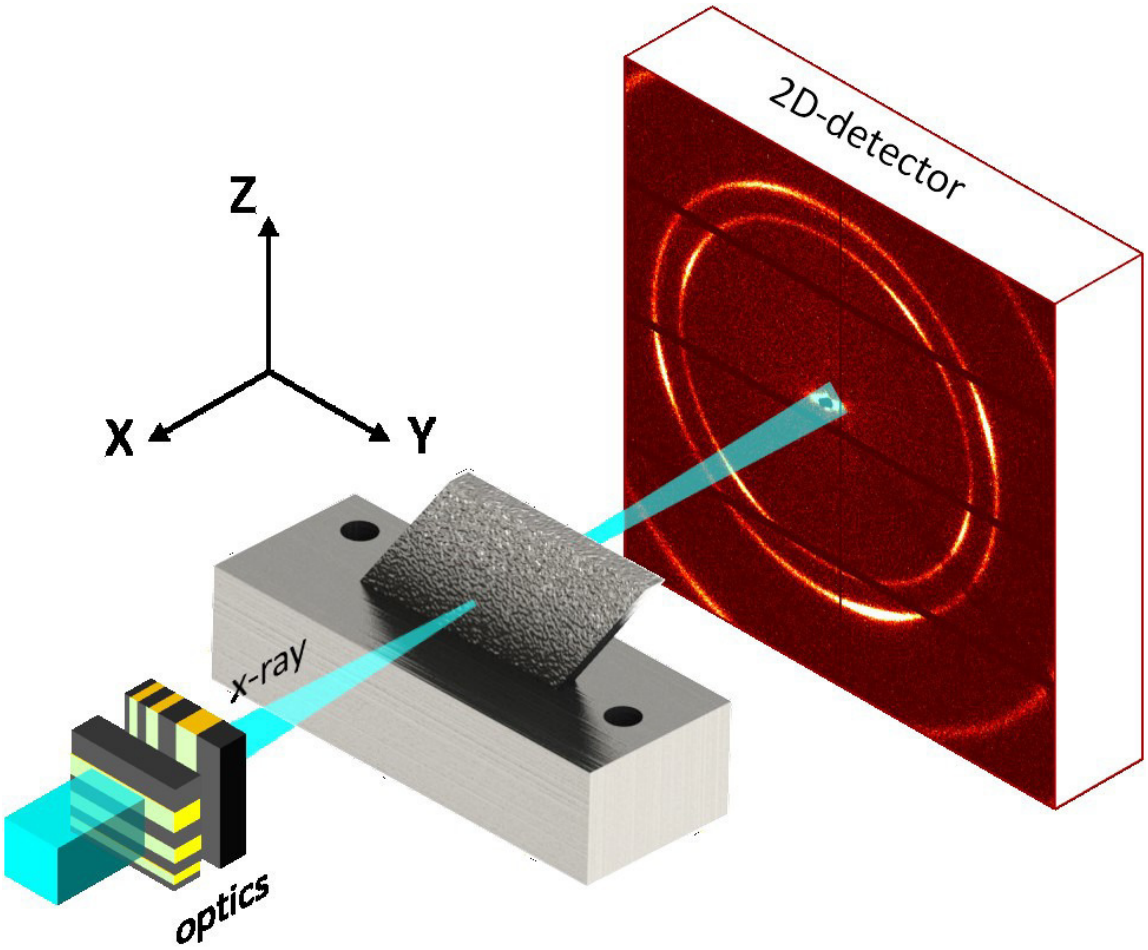

Figure 13: A schematic sketch of the experimental setup used for the synchrotron experiments. The x-ray beam diffraction on lattice planes within the polycrystalline AM structure results in the occurrence of Debye-Scherrer-rings on the 2D detector.

3.2.1 Phase analysis

A radial integration of the Debye-Scherrer-rings yields a phase plot, in which the diffraction intensity is plotted as a function of the scattering angle θ (see Figure 14). The positions and intensities of the diffraction peaks (cf. Figure 14a) depend on the size of the unit cell as well as on the distribution of atoms and their nature within the cell, as described by structure factor. The diffraction signal $I(\theta)$ can be understood as the fingerprint of the samples. The comparison of the measured signal with calculated signals of a database enables the identification of individual phases.

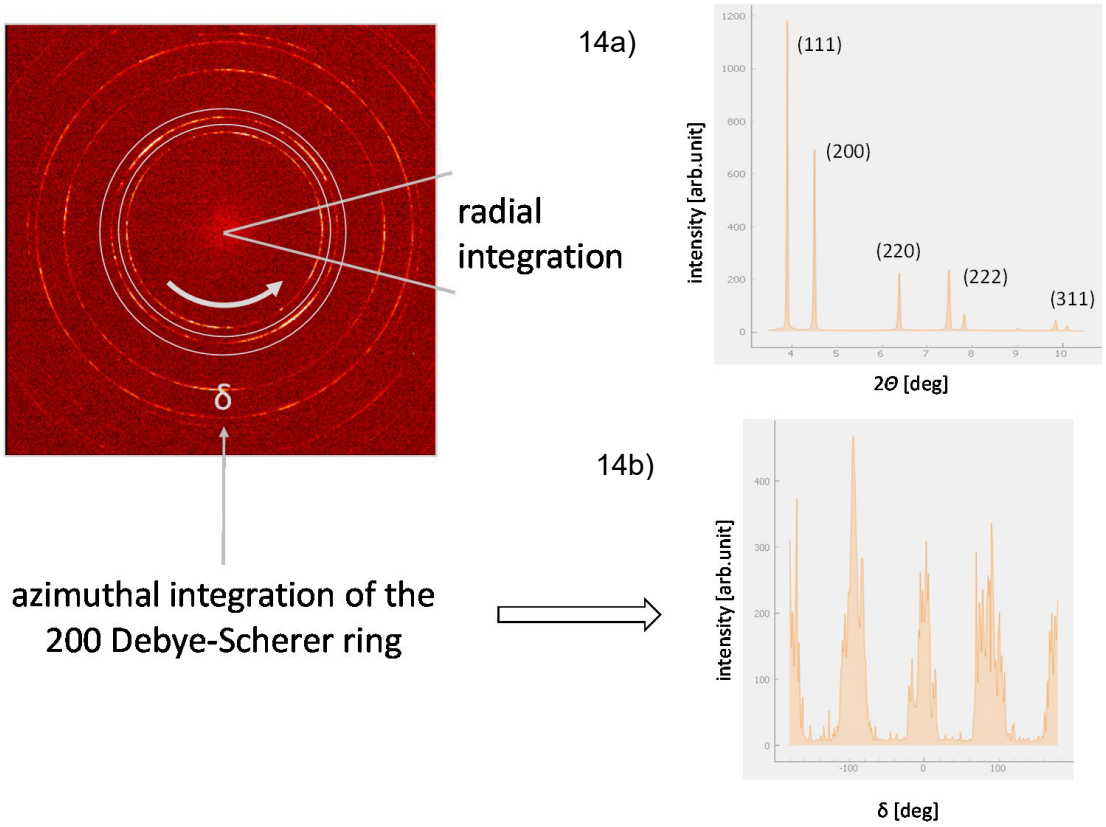

Figure 14: The radial and azimuthal integrations of the Debye-Scherrer-rings allow for the evaluations of phases (phase plot – 14a), strains and texture (texture plot – 14b).

3.2.2 Texture analysis

The texture plot presented in Figure 14b is the result of the azimuthal integration of one 200 Debye-Scherrer-ring. The intensity distribution $I(\delta)$ allows for the determination of the sample preferred orientation. In the case of an ideal powder sample, all grains would be oriented randomly, and the diffraction intensity signal would be constant all over δ.

3.2.3 Stress analysis

The Debye-Scherrer-rings are expected to be perfectly circular for ideal powder samples and stress-free materials. Thus, any azimuth integration provides representative data on the peak positions and the sample composition. In strained materials, however, Debye-Scherrer-rings are either elliptical and/or their diameter is different, compared to the rings of unstressed samples. Thus, a peak shift can be used to evaluate the stress and the strain tensor components of the material.

Synchrotron X-ray diffraction using high energetic photons, as in the present case, can be used to examine a volume of the sample.

The analysis of synchrotron data within this thesis bases on some simplifications:

i) The experiments were used to evaluate only principal strains and stresses.
ii) Due to the geometry of the sample (detailed presented in Figure 8), the stress-component $\sigma_X \rightarrow 0$ in X-direction can be neglected for simplicity.
iii) Due to the layer by layer deposition of the material, the stress in Z-direction $\sigma_Z \rightarrow 0$ can be neglected. The stress relaxation in Z is not assumed to be hindered.
iv) The main stress component influencing the sample strain state in the experiment geometry from Figure 13 is $\sigma_Y \neq 0$
v) The material elastic constants are isotropic.

As a consequence, it is possible to evaluate the stress level in Y-direction by the analysis of the elliptical shape of Debye-Scherrer-rings by considering measured strains in Y and Z direction ε_Y and ε_Z. The derivation of the equation for the evaluation of the stress level is provided below.

$$\varepsilon_Y = \frac{\sigma_Y}{E} \tag{7}$$

$$\varepsilon_Z = \frac{\sigma_Y \cdot \upsilon}{E} \tag{8}$$

σ_i and ε_i are the stress and strain components in X-, Y- and Z-direction, respectively. The Poisson's ratio is υ.

Furthermore, the measured X-ray elastic strain ε_δ^{hkl} at the δ position of the *hkl* Debye-Scherer ring can be expressed as follows:

$$\varepsilon_\delta^{hkl} = \varepsilon_{33}^{hkl} = a_{3i} \cdot a_{3j} \cdot \varepsilon_{ij} = \varepsilon_Y \cdot \sin\delta \cdot \sin\delta + \varepsilon_Z \cdot \cos\delta \cdot \cos\delta \tag{9}$$

And therefore

$$\varepsilon_\delta^{hkl} = \varepsilon_Y \cdot \sin^2\delta + \varepsilon_Y \cdot \cos^2\delta \tag{10}$$

Substitution of ε_Y and ε_Z from Eqs. 7 and 8, expressing $\cos^2\delta$ by (1-$\sin^2\delta$) and by deriving the whole equation with respect to $\sin^2\delta$ leads to

$$\frac{\partial \varepsilon_\delta^{hkl}}{\partial \sin^2\delta} = \sigma_Y \cdot \frac{(1+\upsilon)}{E} \tag{11}$$

Finally, Eq. 11 expresses, that the stress in the direction of Y can be calculated by analyzing the lattice spacing along Z- and Y- directions. Alternatively, Eq.11 can be expressed as

$$\frac{\partial d_\delta^{hkl}}{\partial \sin^2\delta} = \sigma_Y \cdot \frac{(1+\upsilon)}{E}\, d_o^{hkl} \tag{12}$$

3.3 Analysis of the metallurgical sample preparation

The process details of the specimen preparation in terms of embedding, grinding, polishing and etching of selected samples are described in Sec. 2.2.5. To interpret the data of optical microscopy, a detailed knowledge about the phase presence and possible microstructure in the sample is needed. The next section describes the composition, the alloying elements and their influence on the different phases of the Inconel718 samples. Table 6 gives the nominal chemical composition of Inconel718.

Table 6: Nominal chemical composition of Inconel718 [12]

element	Ni	Cr	Fe	Cb	Mo	Ti	Al
m [%]	50-55	17-21	balance	4.75-5.50	2.80-3.30	0.65-1.15	0.20-0.80

element	Co	C	Mn	Si	P	S	B	Cu
max m [%]	1	0.08	0.35	0.35	0.015	0.015	0.006	0.30

The following description of the alloying elements is the summary of the introducing chapters from [13], [17], [18]. Further references are given at the position of their specific use.

Nickel (Ni)

With an amount of up to 55 mass-percent (m-%), face-cubic-centered (fcc) Ni is the matrix component of the material. Substituting single atoms by Chromium (Cr), iron (Fe), Columbium (Cb), Titanium (Ti), Aluminum (Al), Cobalt (Co), the γ-phase is formed.

Chromium (Cr)

A Cr content of more than 17 m-% guarantees the corrosion resistance of the alloy even at elevated temperatures of up to 650°C due to the formation of passivating Cr_2O_3 at the surface. Cr limits the formation of Ni_3Al (γ'-phase). This is even more important for other superalloys, that usually have a higher Al but a lower Cb content. With Carbon (C), Cr aggregates to carbides, mainly $Cr_{23}C_6$ that precipitate often at grain boundaries. The form of the precipitation is important and can be globular, plate-, cell-, lamellae-like or a film. Cr supports the formation of topological closed packed (TCP) phases like σ and Laves. Depending on the precipitation temperature, σ-phase forms in lamellae or acicular shape. TCP phases are undesired as they lower creep strength and ductility significantly.

Iron (Fe)

Even though iron decreases the corrosion resistance, it is used in superalloys to substitute the higher priced Ni. The maximum content is limited because like Cr, also Fe supports the formation of TCP.

Columbium (Cb)

For Inconel718, the elevated content of Cb is typical. Cb reacts with Ni to form Ni_3Cb and therefore, less Ni is disposable to react with Al. Thus, Cb inhibits the coarsening of γ'. Ni_3Cb (γ''-phase; DO_{22} crystal structure; body-centered-tetragonal bct) is the principal strengthening phase in Inconel718. It is metastable and precipitates as partially coherent, disk-shaped particles on the {100} planes with an average diameter of approximately 60nm and a thickness of 5 to 9 nm. As in γ', single atoms in the unit cell can be substituted by other atoms, the lattice constant varies as a function of the actual alloy content [17], [19]. As reported in [19], the formation of a relevant amount and particle size of γ''-phase is sluggish and only after specific heat treatment for several hours. At temperatures exceeding 650°C, up to 980°C, γ'' transforms to the stabile, orthorhombic δ-phase (crystal structure $D0_a$). This phase is incoherent, and the characteristics of its formation are strongly temperature-dependent. The solvus temperature of the brittle δ-phase is approximately 1000°C. Forging below 980°C enables the control and refinement of the grain size and helps to optimize mechanical properties.

Molybdenum (Mo)

Mo forms strong covalent bonds with Ni and strengthens superalloys due to solid solution hardening. It increases the Young's modulus, the solution temperature of strengthening γ'-phase and decreases the coefficient of diffusion. These three effects contribute positively to creeping resistance. With C and Fe, it can form randomly distributed Fe_3Mo_3C. This carbide may appear pinkish. Mo furthermore supports the formation of TCP-phases and decreases corrosion resistance, especially at elevated temperatures.

Titanium (Ti)

Ti substitutes Al in γ' and increases therefore the amount of this phase. Additionally, this element raises the anti-phase-boundary energy and the lattice parameter of γ'. As a result, the γ/γ'-lattice-mismatch is higher and γ'-grains coarsen faster. In contact with C, Ti builds TiC. Higher contents of Ti lead to the formation of Ni_3Ti (brittle η-phase, hexagonal-close-packed (hcp)) that may occur intergranularly in cellular form or as acicular platelets in a Widmanstätten pattern. η-phase has no solubility for other elements. Ti can deteriorate the oxidation resistance.

Cobalt (Co)

In some extend, Co substitutes Ni in γ' and stabilizes therefore γ. It reduces the stacking fault energy (Co ≈ 25 mJ/m²; Ni ≈ 300 mJ/m²). As a result, the creep resistance is increased. While Co reduces the solubility of Al and Ti, the amount of γ' is increased. Moreover, Co delays the coarsening of γ' and counteracts the formation of TCP. A negative aspect is the reduction of γ'-solution temperature. Higher Co contents reduce the high-temperature corrosion resistance.

Further alloying elements

The content of remaining elements in Table 6 is less than 1%. The meanings of the desired alloying elements are the mainly reinforcement of the superalloy (C forms carbides) and pinning of grain boundaries and reduction of grain boundary diffusion (mainly Boron) in order to increase creep stability.

4 Experimental Results and Discussion

This chapter presents the results obtained using the formerly described experimental procedures. The order complies with the chronological order in which the results were obtained. First, the powder had been analysed. In the next step, the tensile samples were produced. Afterwards, the surface roughness of the tensile samples was characterized before the tensile tests were performed. Based on these results, the geometries for the synchrotron tests were prepared and measured. The results of the selected, metallurgically prepared specimens are given and discussed at the respective positions.

Since 123 tensile samples and six synchrotron specimens were produced and analysed, this chapter presents only representative results. The detailed outcomes of the single parameter combinations are presented in the Appendix.

4.1 Analysis of powder particle size and distribution

A histogram showing the particle size distribution and the corresponding SEM image of the raw powder are presented in Figure 15. The form of the particles is mainly spherical, and the amount of satellites is low. Furthermore, a marginal number of particles is misshaped. The mean particle size of ~19µm was determined by the analysis of the SEM image using the ImageJ software [20]. The d_{50} of the particle size was specified to be 50µm by the powder supplier (LPW Technology Ldt, United Kingdom). One reason for the observed difference could be the preparation method used to distribute the powder on the SEM sample holder. In order to avoid this potential drawback, an additional analysis by laser diffraction would be required.

The amount of 11.5 % of powder particles with a diameter between 1 µm and 3 µm is significant. These fine particles should be separated e.g. by sieving, as they tend to be vaporized during the SLM process, thus cause defects and reduce the qualities of the powder and built parts.

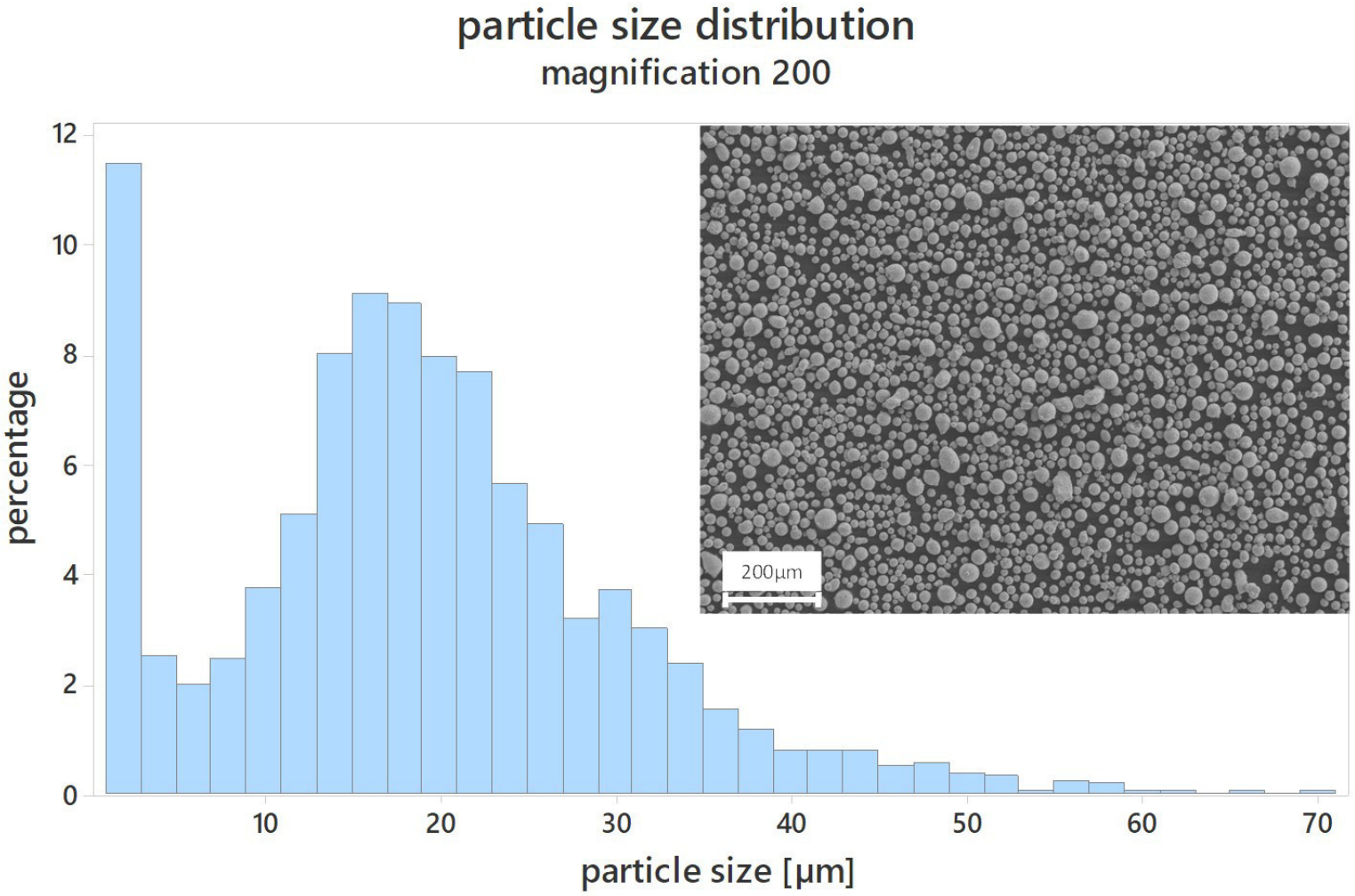

Figure 15: Histogram of the size distribution and the corresponding SEM image of the raw powder (200 times magnified).

4.2 Additive manufacturing of tensile specimens

As explained in Sec. 2.1.1, laser power *P*, scan speed *v* and layer thickness *s* were varied in 41 different combinations. Table 7 presents the minimum, maximum and average values of the three input factors, which studied combinations are presented Figure 6.

These variations led to different volumetric energy densities (see Eq. 1). Figure 16 illustrates the correlation between *VED* and the sample number. Three coloured symbols mark the different layer thicknesses. The sample numbers 1 to 27 represent the fully factorial test region. Specimen's numbers 28 to 41 represent the one-factor-at-time test region (constant layer thickness = 50 µm) where extremes of *P* and *v*, respectively, were examined.

Table 7: Maximum, minimum and average values of the input factors *P*, *v* and *s* used to fabricate the tensile samples.

input factor		minimum	maximum	average
laser power	*P* [W]	25	285	111
scan speed	*v* [mm/s]	300	2000	970
layer thickness	*s* [µm]	20	80	50

It was not possible to build any macroscopic solid sample with the lowest *VED* of 5 J/mm³ - corresponding to sample number 28. All the other samples could be built and most of them could also be investigated.

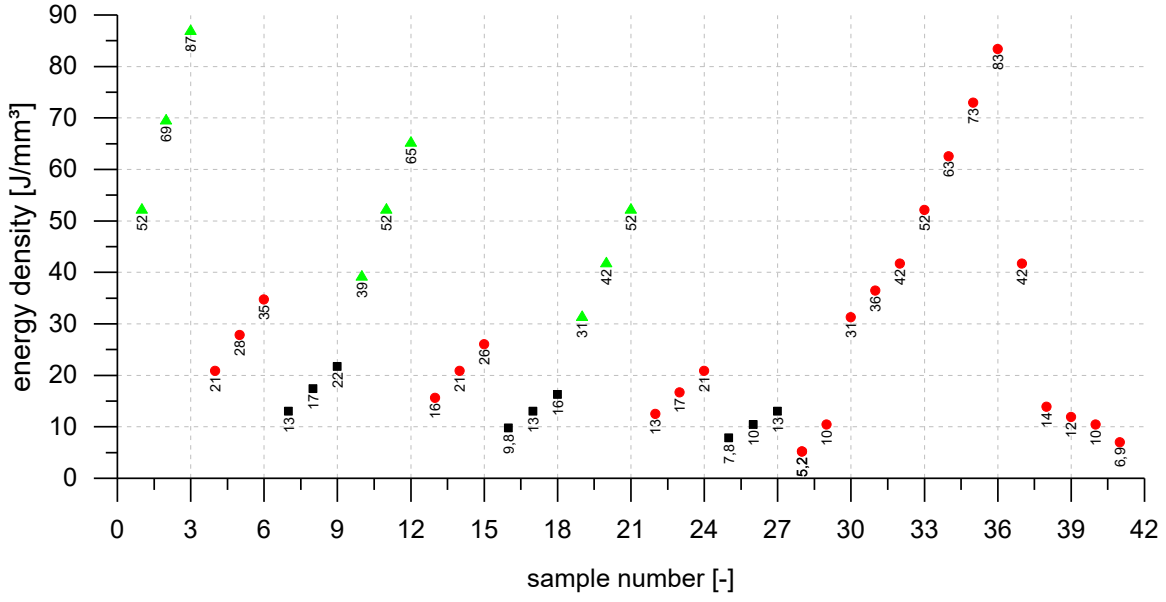

Figure 16: The variation of *P*, *v* and *s* lead to energy densities *VED* in the range of 5 to 87J/mm³. A small number beneath each symbol indicates its specific *VED.* Different colors and symbols belong to different applied layer thicknesses:
20µm – green triangles; 50µm – red circles; 80µm – black squares.

Figure 17 shows three representative tensile samples, produced with low, medium and high *VED*. Further photographs of the tensile samples are presented in the Appendix. A striking feature of the specimens is their varying surface roughness. Some parameter combinations – mostly those with the layer thickness of 20µm – are useful to build geometrical details like sharp edges or notches.

Thus, the output of this study allows for the optimization of mechanical properties and the minimization of the residual stresses as well as for the improvement of surface-relevant parameter sets that are used to build contours and scriptures.

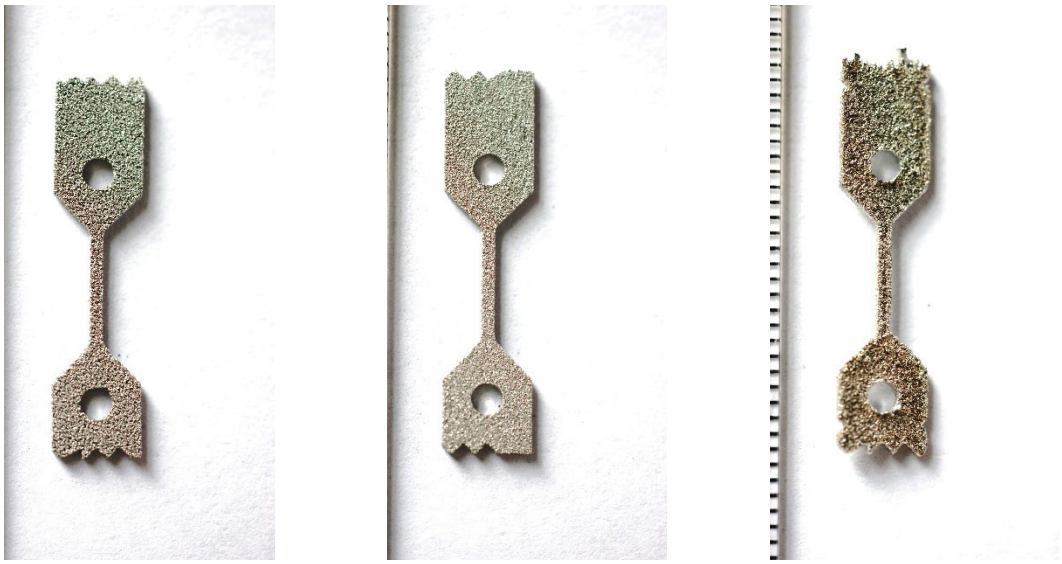

sample number: 25	sample number: 20	sample number: 36
VED = 8 J/mm³	*VED* = 42 J/mm³	*VED* = 83 J/mm³

Figure 17: Variation of *VED* resulted in visible differences in sample roughness. Specific combinations of different notch types and their positions enabled the identification of the specimens during the further experiments at any time.

4.3 Roughnesses of 45° upskin, 45° downskin and vertical oriented surfaces

As a representative example of the sample surface roughness and morphology measurements, the laser microscope image of a 45°-upskin surface (sample number 36: P = 100; v = 240; s = 50µm; VED = 83 J/mm³) is presented in Figure 18. The laser image is superimposed by the semitransparent result of the topographical analysis. Yellow-greenish areas represent a level of the sample height that was considered to be zero. Referred to this, reddish are elevated and bluish are lowered, respectively. The height level at this specific sample can considered to be constant over a width of two hatch lines, corresponding to approximately ~200 µm.

The little number of spatters would be removed during a post-processing treatment like cleaning by carbondioxide blasting, electro-chemical etching or abrasive flow machining.

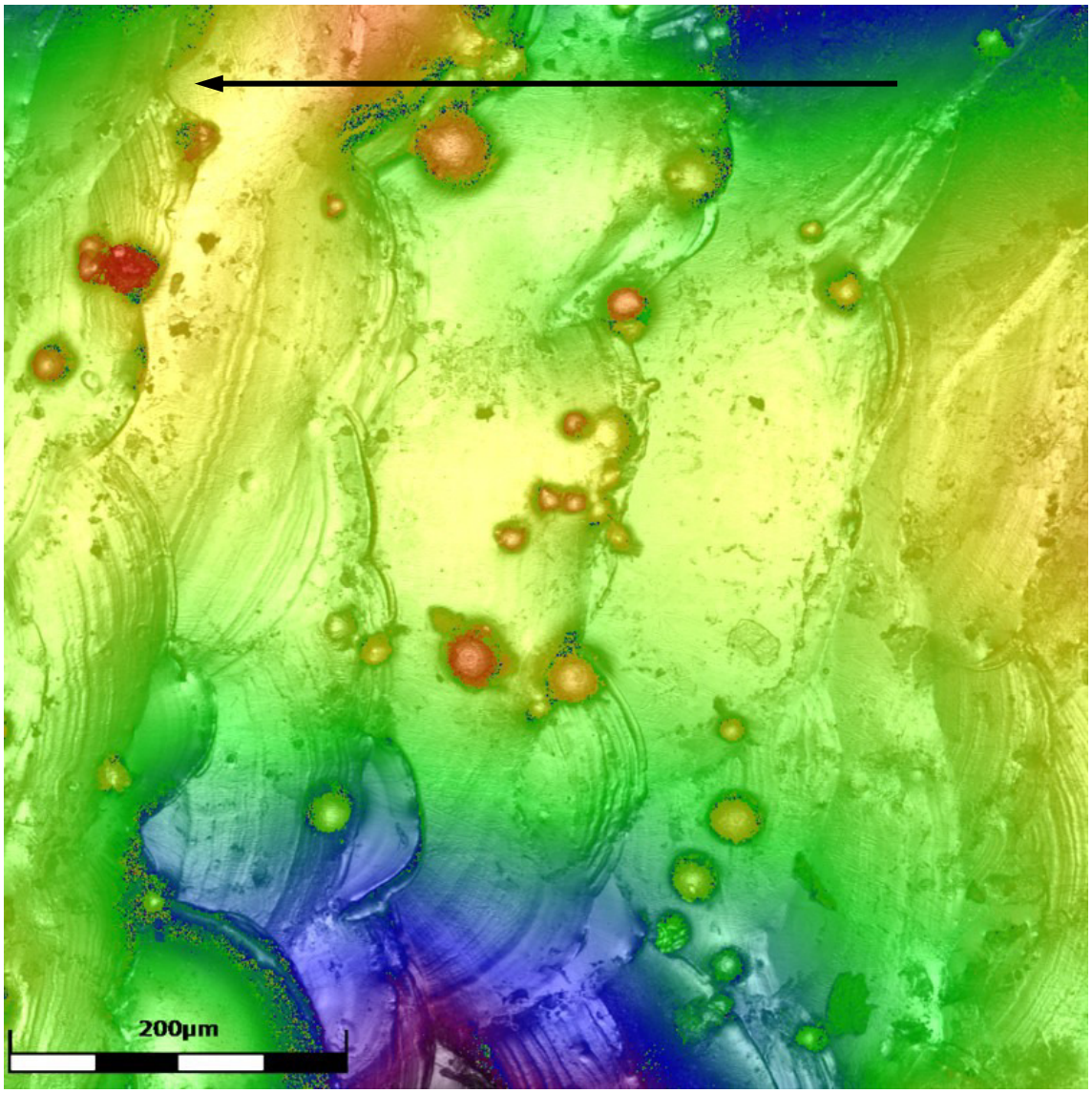

Figure 18: A super position of a laser microscope image and the corresponding topographical analysis image. Yellow-greenish areas correspond to a neutral height level, blueish regions are lowered and reddish are elevated. This sample was produced with the second highest *VED* of 83 J/mm³. The built-direction is indicated by an arrow at the top of the image.

Rounded minimum and maximum values of R_a for the three types of surface (upskin, downskin and vertical) among all samples are indicated in Table 8. The large R_a range documents, that the improvement in surface roughness strongly depends on the energy input during the deposition procedure. Furthermore, it can be noted that for the improvement of the vertical and upskin oriented surfaces, high energy densities are necessary, whereas for the mean downskin surface roughness different effects seem to improve the result.

Table 8: Minimal and maximal mean roughnesses R_a for vertical, upskin and downskin oriented raw surfaces.

surface orientation	type and corresponding sample number	*P*	*v*	*s*	*VED*	R_a
[-]	[-]	[W]	[mm/s]	[µm]	[J/mm³]	[µm]
vertical	minimum / sample number 35	350	960	50	73	14,0
	maximum / sample number 29	50	960	50	10	45,0
45°-upskin	minimum / sample number 3	125	720	20	87	14,0
	maximum / sample number 25	75	1200	80	8	45,0
45°-downskin	minimum / sample number 32	200	960	50	42	19,0
	maximum / sample number 25	75	1200	80	8	54,0

Additional evaluation opportunities were enabled by the statistical design of the experiment. Figure 19 to 21 show the main effects plots of the average R_a values for vertical, upskin and downskin surfaces within the full factorial test region (sample numbers 1 to 27). Even though the statistical theory of the “model of effects” does not allow any data extrapolation between the individual data points, these diagrams enable the estimation of the trends.

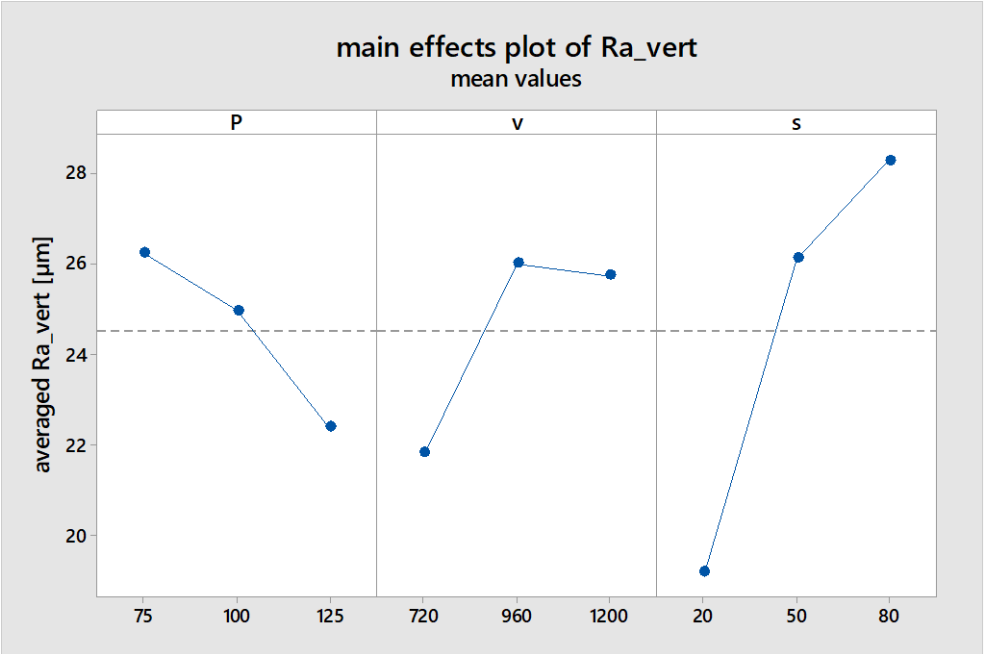

Figure 19: Main effects plot of average R_a values for the vertical surface roughness. The trend of this analysis indicates that an improvement in the surface quality can be obtained by high laser power, slow scanning velocity and small layer thickness, resulting in a higher *VED*.

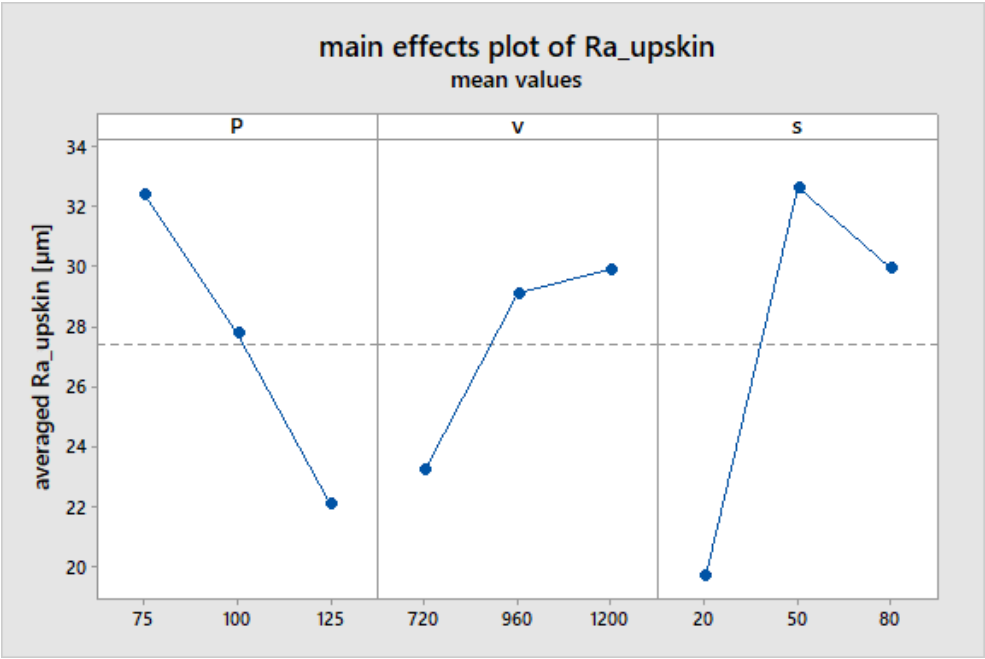

Figure 20: Main effects plot of average R_a values for the upskin surface roughness. The trend of this analysis indicates that an improvement in the surface quality can be obtained by increasing the laser power, lowering scanning velocity and decreasing layer thickness, resulting in higher *VED*.

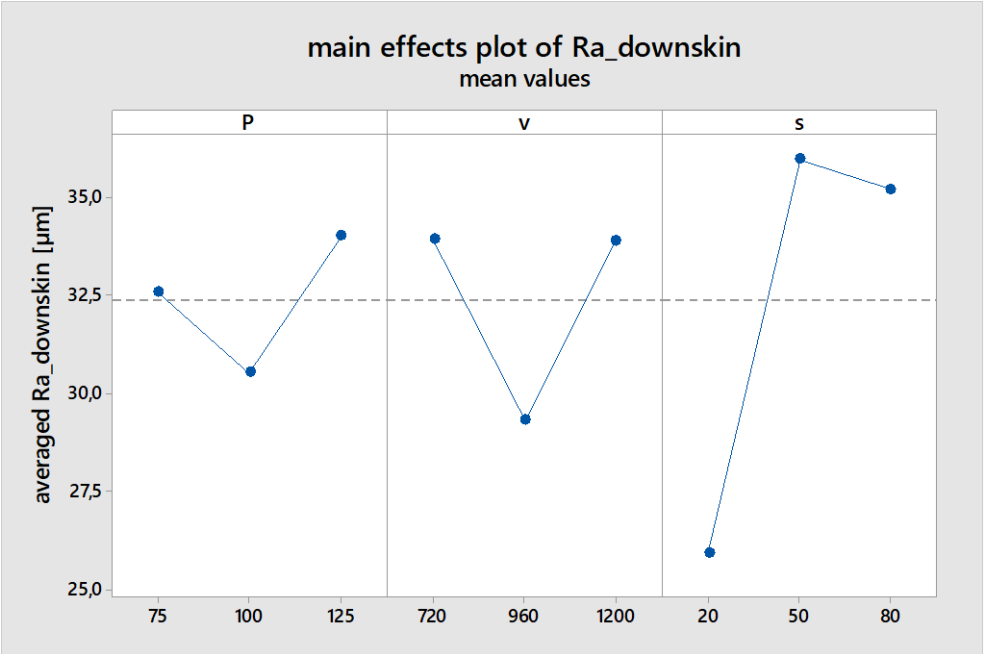

Figure 21: Main effects plot of average R_a values for the downskin surface roughness. The trend of this analysis indicates that an improvement in the surface quality can be obtained by decreasing the laser power, the layer thickness and therefore *VED*.

In contrast to the experiments where only one input factor at time was varied, the main advantage of factor plans is the possibility to determine also the mutual influence of more parameters. Figures 20 to 22 show the interaction plots of *P*, *v* and *s* for vertical, upskin and downskin orientations in relation to the surface roughness. One line for each factor is displayed as a function of the means for the levels of another factor (X-axis). Parallel lines indicate that no interaction occurs between two input factors while antiparallel lines indicate the opposite [14].

For a detailed interpretation of the main effects plot and the interaction plot, the significance of the effect must be taken in account. Non-significant relationships occur by accident and should not be further interpreted. If there exists a meaningful relationship for data from the interaction plot, the main effects diagram must not be interpreted without taking the interaction plot into account. The assessments of significance bases on a confidential interval of 95 %.

For the mean vertical roughness R_{a_vert}, the statistical analysis revealed, that the interaction effects up to the second order are not significant. The splitted course of the different layer thicknesses indicate a kind of jump function development for the layer thickness *s*. The effect of *s* on vertical surface roughness is significant. Further decreasing in the layer thickness is not expedient, as the average particle size is ~19µm. Even though the variation of *P* and *v* were determined to be not significant, the trend of their influence can be deduced by the main effects plot in Figure 19: higher energy input due to increasing the laser power and increasing the scanning velocity improves the vertical surface roughness.

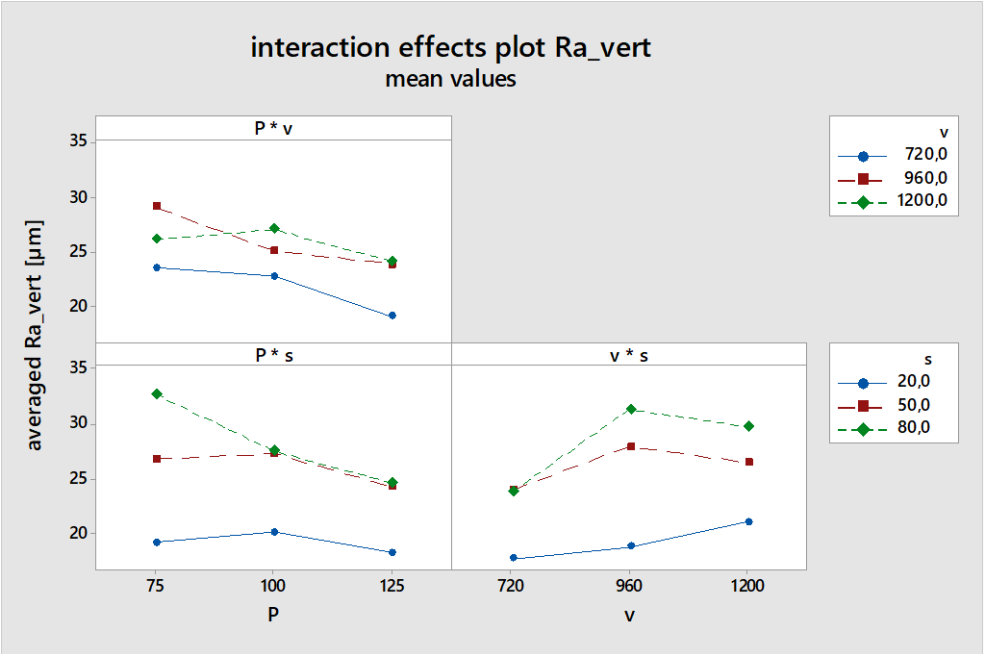

Figure 22: Interaction effects plot of average R_a values for the vertical surface roughness. The statistical analyses revealed, that these interactions are not significant.

The interaction effects for the mean roughness R_{a_upskin} of 45° oriented upskin surfaces were determined to be not significant and thus, the separate interpretation of the main effects plot in Figure 20 is acceptable. Even if the courses of the input factors in the main effects plot are similar to the trends for R_{a_vert}, their influence on the 45°-upskin surface quality is of more importance. It was figured out that the layer thickness *s* has the highest impact factor before *P* and *v*.

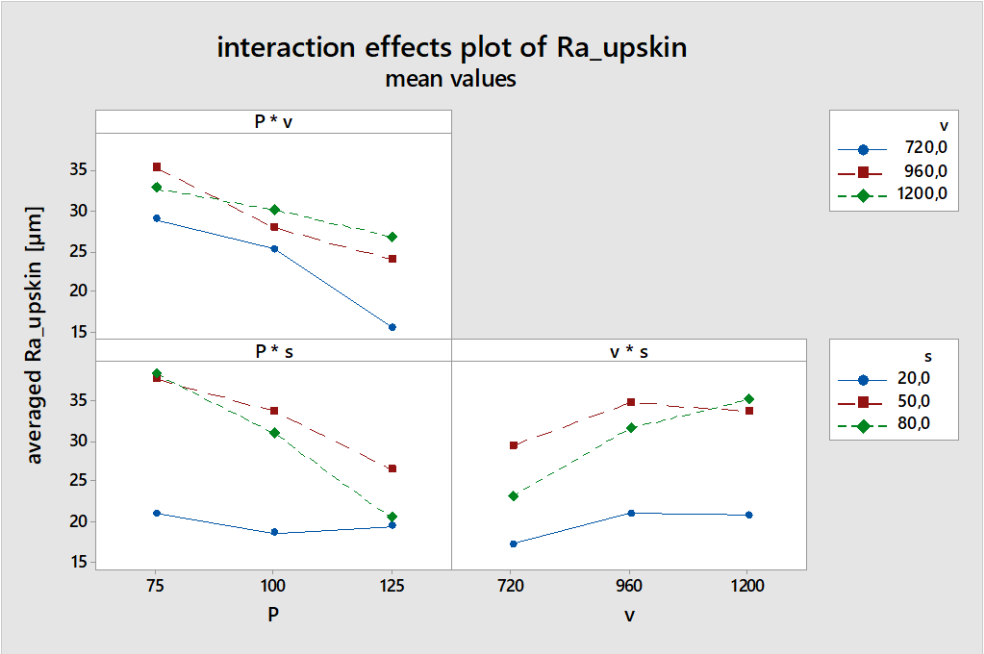

Figure 23: Interaction effects plot of average R_a values for the 45° oriented upskin surface roughness. The statistical analyses revealed, that these interactions are not significant.

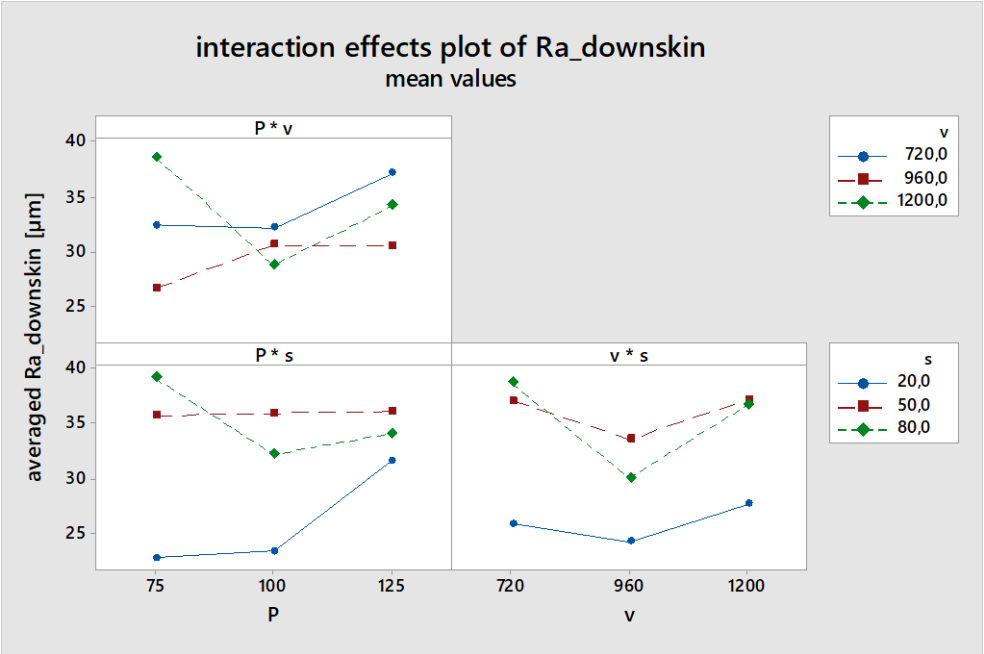

Figure 24: Interaction effects plot of average R_a values for the 45° oriented downskin surface roughness. The statistical analyses revealed, that these interactions are not significant.

For the mean roughness $R_{a_downskin}$ of 45°overhanging surfaces, within the examined parameter's region, the interaction effects are not significant and only *s* was specified to have a remarkable influence. However, in contrast to the vertical and upskin oriented surfaces, where a higher energy input was determined to lower the surface roughness, the quality of downskin surfaces tends to improve with less applied *VED*. It would be considerable to follow the approach of increasing the quality of downskin surfaces by a reducing *P* in combination with a stronger increasing of *v*.

In general, this evaluation of surface quality could be improved, if more than just one area was investigated by laser scanning microscopy. Further effort in an improvement of the surface roughness is important, as post-processing of AM for improving the surface quality is expensive. Moreover, inboard surfaces of mechanical relevant grid structures are not accessible at the finished product and cannot be reworked therefore.

4.4 Tensile tests

As explained in Sec. 2.1.1, for every parameter variation, stress-strain plots of three redundant samples were recorded.

4.4.1 Analysis of R_m, $R_{p0.2}$, A and E

The representative stress-strain plots from sample number 36 (cf. Figure 16), represented by three tensile samples, are illustrated in Figure 25a. A detailed parameter combination for all samples is given in the Appendix. This parameter variation shows the highest average strain at fracture of A_{max}~33.00 ±0.12 %. The mean ultimate yield strength R_m is 555 ±26 MPa and $R_{p0.2}$ is 337 ±14 MPa.

The maximum ultimate tensile strength R_{m_max} of 734 ±102 MPa was measured with the parameter set of sample number 12. The corresponding $R_{p0.2}$ and A are 523 ±75 MPa and 28.43 ±0.55 %, respectively. From Figure 25b it is obvious, that the stress-strain plot of the first test series differs significantly from test series two and three. A reason for this deviation of almost 22 % could be, that the test length of the specimen that was analysed in the first test series, is almost free of defects like pores and the present pores were smaller than the critical size for failure. However, if the result of this first test series was decided to be a statistical outliner, the data of the remaining two tensile experiments would still lead to the highest R_m of 662 ±3 MPa among all combinations together with sample number 3.

Sample number 3 reached also an average R_m of 662 ±10 MPa. The stress-strain plots are depicted in Figure 25c. $R_{p0.2}$ is 452 ±11 MPa and A is 30.53 ±1.16 %.

Even though neither the maximum value of R_m, nor the maximum value of A are topped by the results of sample number 35 (presented in Figure 25d), it should be noted, that using this parameter set, a part can be built in less than half of the production time compared to samples 3 and 12 as the layer thickness here is 50µm. It is remarkable that the mechanical properties can still compete (R_m = 642 ±6 MPa; $R_{p0.2}$ = 422 ±10 MPa; A = 28.40 ±1.50 %).

In literature, comparable values for R_m, $R_{p0.2}$ and A can be hardly found, as the testing conditions (sample geometry, surface roughness requirements) within this study were different from the standards given by ISO 6892-1:2009. While the “as-build”-microstructure differs strongly from wrought or tempered conditions, the results cannot be compared to these data. In Ref. [21], EOS GmbH gives a R_m of 980 ±50MPa, a $R_{p0.2}$ of 634 ±50 MPa and a A of 31 ±5 % for the “as-build” status. To reduce the effect of the geometrical difference, further three samples with the similar of the tensile specimens were produced by wire cut EDM and tested. The analysis revealed a R_m of 674 ±16MPa, a $R_{p0.2}$ of 354 ±12 MPa, a A of 41.8 ±1.13 % and a Young’s modulus E of 190 ±27 GPa (cf. Appendix, page k).

Another distortion of the results bases on the different cross sections of the specimens. Depending on the real energy input during the deposition, the size of the melting pool is different [22]. Thus, the geometrical precision is being influenced. It is possible to take this deviation in account automatically in the software of the SLM device for optimized parameter sets. As described in Sec. 2.2.2, for this study, every cross-section had been measured by an outside micrometer before the tensile tests were performed. The high surface roughness and the measurement zone of the micrometer limited the precision of these measurements.

Therefore, the real load bearing cross-section was smaller, and the analysed values of ultimate tensile strengths are too low.

Considering all the different geometrical and microstructural conditions of specimens and the deviation caused by the real load bearing cross-section, within this thesis, a lower limit for defining the technical relevant ultimate yield strength was decided at 550 MPa. Consequently, the further discussion of results within this section will be devoted only to specimens that exceed this lower limit of R_m.

The Young's modulus E was determined as described in Sec. 2.2.2 for every sample. The average Young's modulus is ~142.0 ±20.0 GPa. This value coincide with the literature value for the as-built-status in reference [21].

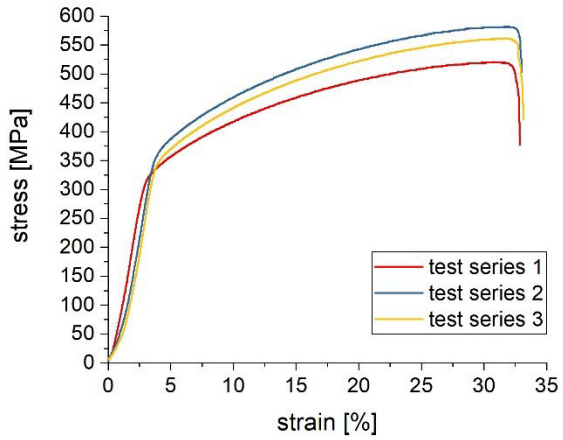

25a) sample number 36 – maximum A

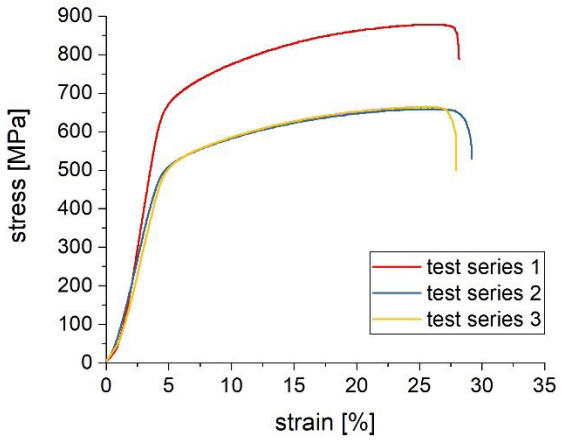

25b) sample number 12 – maximum R_m

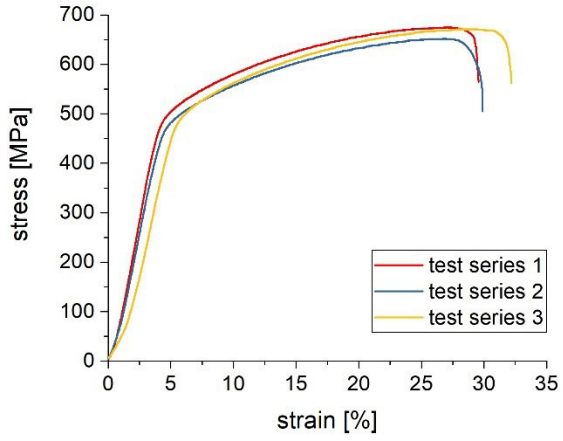

25c) sample number 3

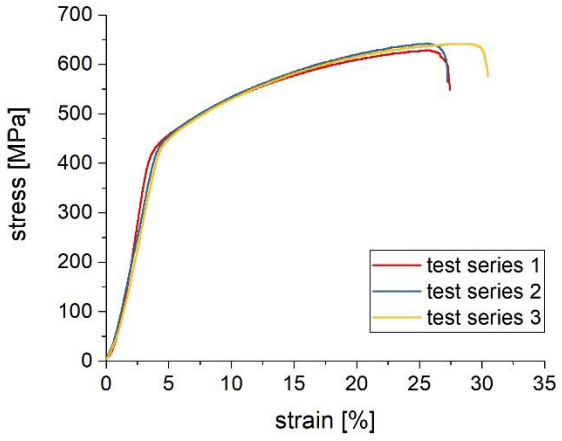

25d) sample number 35 – half production time

Figure 25: Stress-strain plots of three test series of the specimens with the highest ductility (25a) and the maximum R_m (25b) and (25c) and maximum performance of R_m and A with only half of the time of production (25d).

Figure 26 illustrates an overview-sequence of the sample numbers and their corresponding, mean R_m. It is obvious, that the layer thickness *s* of 80 µm does not lead to sufficiently high R_m in combination with the studied ranges of *P* and *v*. Among the 41 basic input factor variations, only 12 led to an average R_m above the lower limit.

A layer thickness of 20 µm results in higher mechanical stabilities than in the case of the thickness of 50 µm. Without further examining, the higher strength can be explained by the higher energy input during SLM for thinner layers and potentially by smaller crystallite size. Therefore, the deposited material of the preceding layer is partly heated up to the melting point or the temperature, at which changes in the microstructure are possible, respectively. In contrast, the energy input for *s* = 50 µm is needed to fuse the powder and not high enough to activate these processes in the preceding layers.

Furthermore, as discussed in the previous section about surface roughness results, the surface quality depends on the layer thickness and improves with decreasing *s*. The vertical surface roughness influences notching effects and thus, smaller layer thicknesses support higher mechanical strength also in this way.

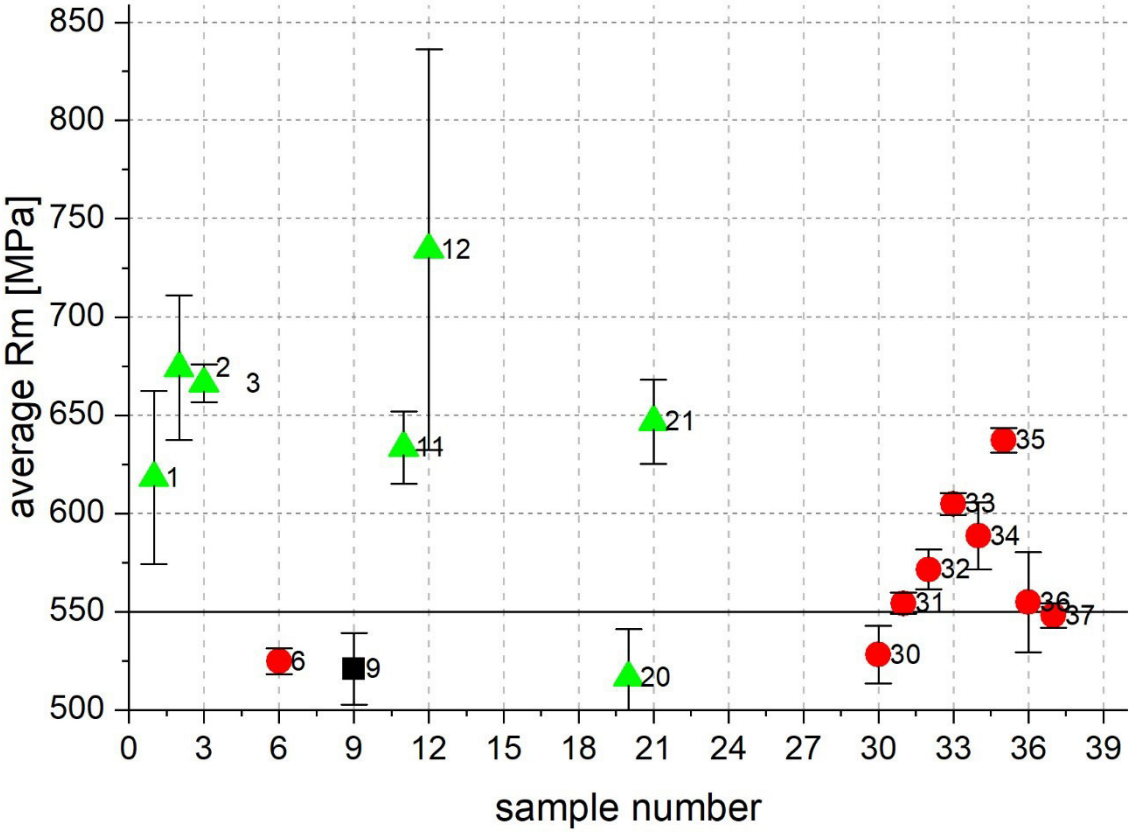

Figure 26: Sequence of sample numbers with an average R_m of more than 550 MPa. The layer thicknesses *s* are indicated by different symbols and colours: 20 µm – green triangles; 50 µm – red circles; 80 µm – black squares. The sample numbers are written next to the symbols.

4.4.2 Statistic impact of *P*, *v* and *s* on R_m

The response of the ultimate tensile strength R_m on the variation of the three input factors was again analysed by Minitab®. The main effects plot and the interaction effects plot of *P*, *v* and *s* are presented in Figure 27 and Figure 28, respectively.

Even though the parallel course of the graphs and the statistical analysis in Minitab® indicate, that there is no significant interaction between the input factors, the interaction effects diagram illustrates the following: The existence of the two separated levels in the interaction effects plot of *P*s* and *v*s* is well pronounced. This indicates, that the course of the layer thickness in the main effects diagram would theoretically lead to a step function with the presence of an upper and a lower shelf.

The statistical analysis showed further, that the layer thickness is the most influencing parameter within the full factorial studied region of the experiment. Reasonable ultimate tensile strength could only be achieved, if a certain layer thickness is not exceeded. The impact of the layer thickness is three times higher than the impact of *P* and *v*. Again, as already mentioned in the discussion of the surfaces' roughnesses, in practice, there is no sense to further decrease the layer thickness as the mean particle size was analyzed to be ~19µm.

The R_m dependencies on *P* and *v* exhibit positive and negative trends, respectively. Their significance is almost the same. All trends show, that R_m will increase, if *VED* increases.

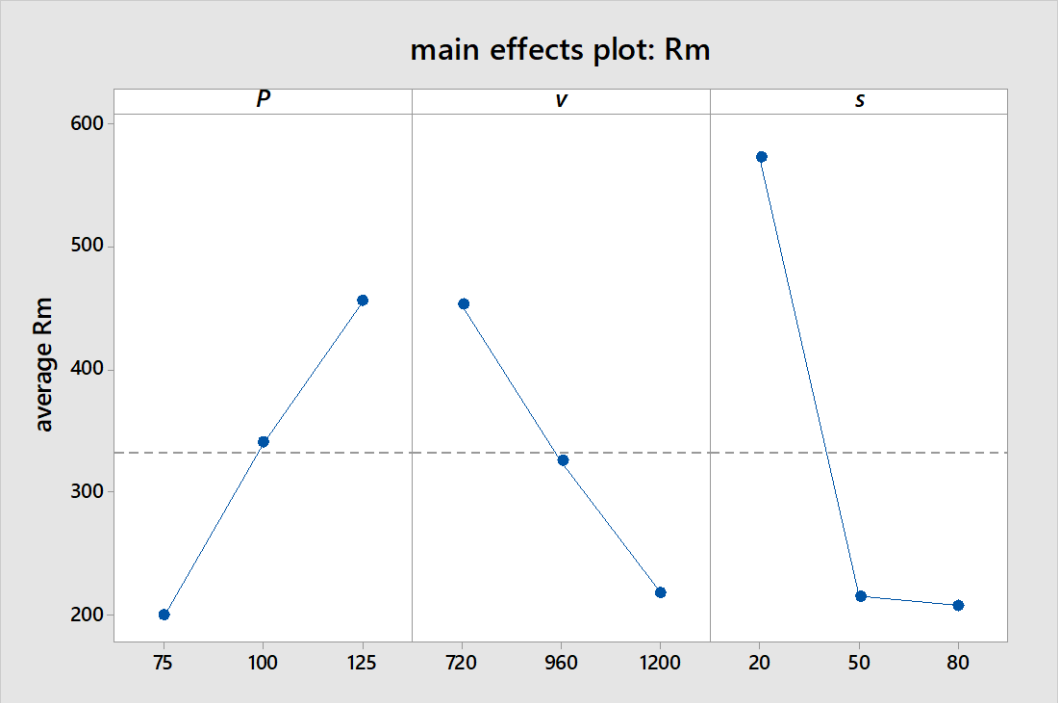

Figure 27: The main effect plot illustrates the response of the ultimate tensile strength on the variation of *P*, *v* and *s*. R_m increases with the increasing laser power and decreasing scanning velocity and layer thickness.

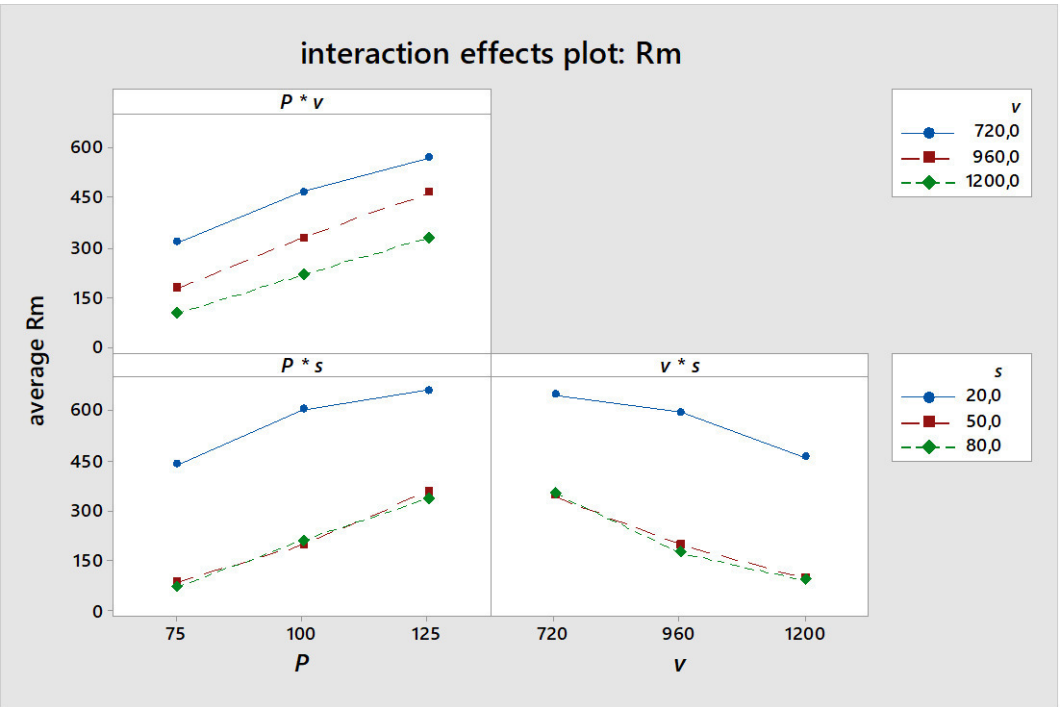

Figure 28: The almost parallel developments of the lines in the interaction effects plots indicate that the there is no significant interaction of the input factors. Also, the statistical analysis revealed that it is acceptable to interpret only the main effect diagram.

In the extremum region, where only one-factor-at-time was changed, while the second factor and the layer thickness of 50 µm were kept constant, non-linear trends were determined for *P* and *v*. From the deviation of *P*, again an upper shelf can be recognized. Based on Eq. 1, one would get to similar energy densities than before in the full factorial region by dividing P by a factor of 2.5. There, comparable mechanical properties were determined for the layer thickness of 20 µm. The conclusion is that a certain minimal energy input is necessary to push R_m values to a relevant mechanical strength range.

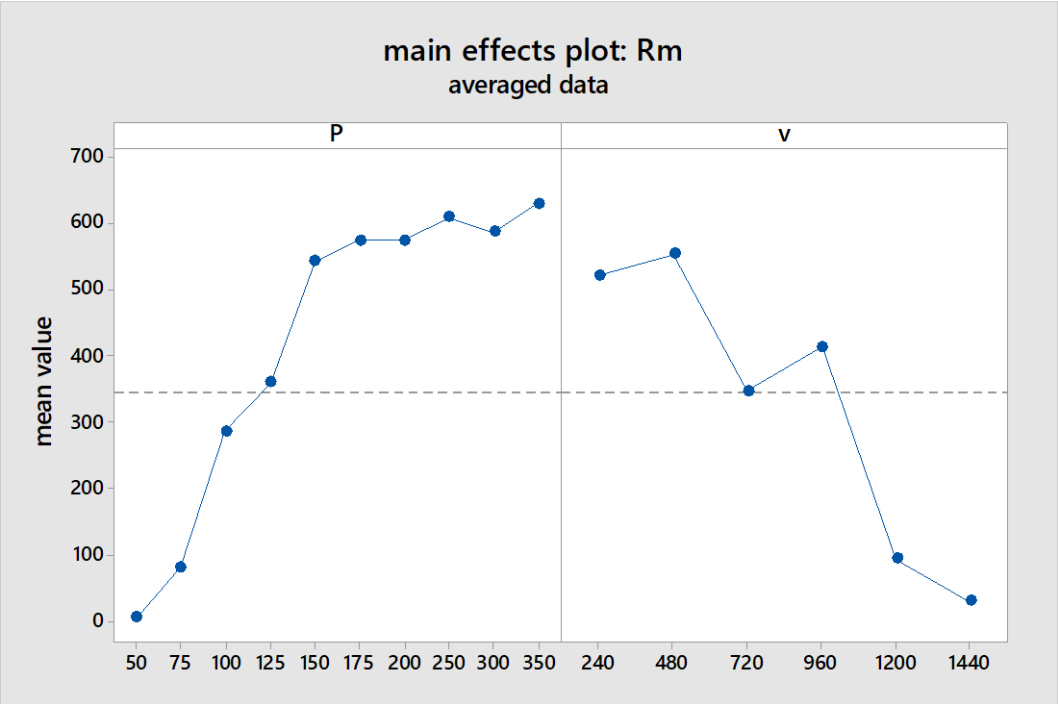

Figure 29: The one-dimensional, one-factor-at-time-test with a constant layer thickness of 50µm shows a non-linear progress of R_m.

At the end of this section, it should be stated, that a further improvement in the whole tensile test execution procedure would be a random specimen-taking plan, which was however not applied. In this way, external influences like e.g. temperature increase during several testing hours cannot be excluded.

4.4.3 Influence of energy input on mechanical strength

The influence of the energy input during the deposition process is expressed by *VED*. Its impact on the mechanical strength is illustrated in Figure 30. This diagram shows, that a minimum energy input is necessary to realize considerable mechanical properties in a solid. The reason therefore is, that a certain energy is needed to fuse the powder particles and joint the new layer to the preceding one. The optical microscope images of six representative samples show the differences in the microstructure. Reference [23] describes different defects and gives a short introduction to their origin. The shape of the pores is characteristic and enables the classification of energy regions. Below a certain energy limit, the pores appear as big voids with irregular shape due to lacks of fusion. Within a limited region of *VED*, the porosity is below 0.5 %. SLM deposition above a certain limit of energy input leads again to the decreasing mechanical strength due to vaporization of the alloying elements. The shape of the resulting gas pores is spherical. To achieve acceptable mechanical properties, for Inconel718 in this study a lower *VED* limit of 40 J/mm³ was determined. At the *VED* of 83 J/mm³, spherical gas pores with a diameter of up to 40 µm were detected. The highest *VED* that was used to produce specimens in this study was 87 J/mm³.

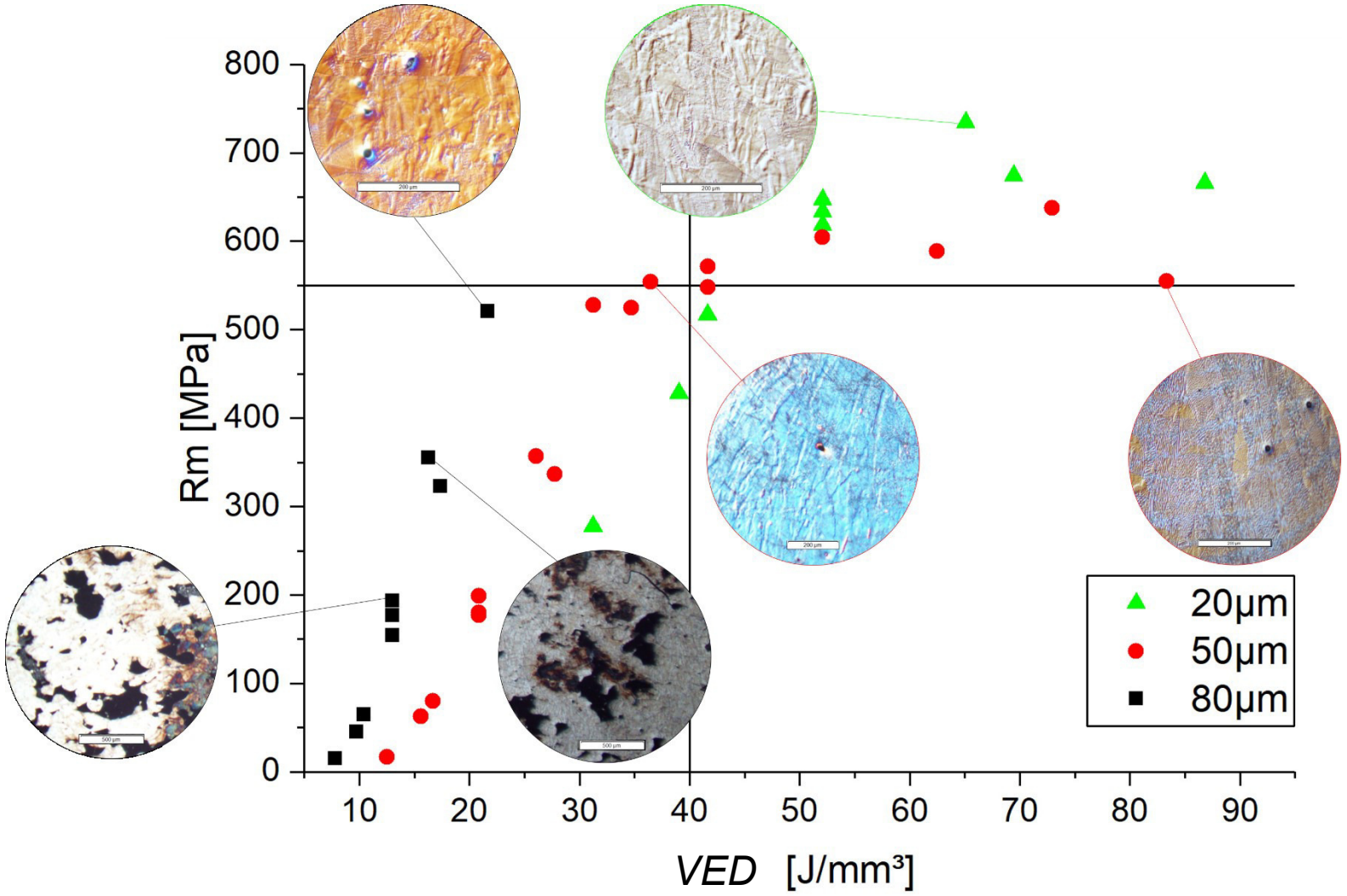

Figure 30: The graphic course of R_m as a function of *VED* indicates, that the mechanical strength of a SLM part is strongly influenced by the *VED* during the deposition. The shape and size of the pores, illustrated by the representative optical microscopy images, allows for the correlation between the mechanical properties and reasonable *VED* range. Different symbols and colours identify the three layer thicknesses.

The high fluctuation of ultimate tensile strength in Figure 30 above the lower limit of 40 J/mm³ indicates, that Eq. 1 can be used only as a rule of thumb for a quick estimation of the process conditions.

This approach does not allow for the comparison to other devices or even other manufacturing processes. Similar, many years' experiences in welding the materials, that are currently available as raw powders for SLM processing, cannot be transferred and used therefore. Currently, optimized parameters that were developed at a different type of SLM equipment cannot be adopted without verification. In fact, not even different, complex geometries can be built immediately at the first attempt, even if optimized parameter sets are ready. Of course, not all these problems can be solved just by calculating one single key value. Nevertheless, any improvement could be achieved by considering especially the following factors:

- **Beam diameter**

  The focus of the laser power *P* defines the beam diameter and therefore the local energy input. To improve Eq. 1, *P* could be replaced by a laser energy density function.

- **Base plate temperature**

  The energy that is transferred from the base plate via the powder bed contributes to the melting and cooling conditions of the produced part. This influence is even more relevant for materials with a low melting point (e.g. Al-alloys)

- **Absorption coefficient of the material**

  As described in chapter 1, mostly lasers with a wavelength of ~1 µm are used for SLM of metals. It is well known, that the absorption coefficient of metals is different for various wavelengths. Taking in account the specific absorption coefficient would help to adopt knowledge from other jointing processes.

- **Powder particle size**

  The size of powder particles has an impact on the energy transmission as the laser beam is being scattered in a different way by small and large powder particles, respectively.

- **Geometry factor**

  Heat transfer within a SLM specimen, that is just being produces, is changing with different geometry conditions. A geometry factor, which considers on geometrical changes and different support structures would contribute to the improvement.

- **Temperature of the protective gas**

  The flow of the protective gas (e.g. Ar or N) results in the cooling of the melting pool and its surrounding. Up to the end of this thesis, no information about any effort on the preheating of the protective gas was provided in any publication. Thus, this approach seems to be new. Preheating of the gas to temperatures of 400°C and even more is standard in the powder manufacturing processes like the gas

atomization process. Supplying gas at elevated temperatures could be an efficient way to stabilize the SLM deposition process and provide specific temperature conditions at different regions of a parts' geometry quickly, as the variation of the protective gas temperature can be realized much more effectively as e.g. the variation of base plate temperature or input factors during a building job. Changing geometrical effects could be compensated and thus, more homogenous deposition conditions within one specimen or product would be realized.

4.5 Synchrotron experiments

This section presents the phase plots, the stress profiles and texture data from six synchrotron samples. Three of them were homogenously deposited and the three were produced with a gradient of the *VED*.

4.5.1 Phase analysis

Figure 31 shows a phase plot from one representative specimen as a function of the built-up height *Z*. This sample was deposited with the parameter sets of the tensile sample number 12. The position of 0 mm corresponds to the surface of the substrate and the position of 11.4 mm to the very top of the sample. The comparison of the diffraction peak positions with the scattering angels given in Ref. [24] and with the peak positions that were calculated by the software *elastix* [25], enabled the indexing of the specific peaks.

Figure 32 presents the position resolved shift of the 200 diffraction peaks in in-plane (left picture) and out-of-plane orientation (right picture). The peak shift of the in-plane orientation to larger and smaller angles is clearly pronounced. It is a measure of the present in-plane residual compressive and tensile stresses. Even though it was assumed a priori, that residual stresses in out-of-plane orientation can relax and thus can be neglected, it is obvious from Figure 32, that this assumption is not fully correct. As the stress in Z-direction at the free surface on the very top of the structure must be zero, the origin of the dashed line was set at the peak maximum at the position of ~11.6 mm. The shift to larger diffraction angels towards the substrate surface indicates the decrease of the lattice plane distance and therefore the presence of compressive stresses. An additional synchrotron calibration experiment would enable the correct determination of the unstrained lattice parameter and would allow for the analysis of the residual stresses in Z-direction. However, the basic approach of the stress analysis as described in Sec. 3 was kept for residual stress analysis in this thesis. Further results will be presented now.

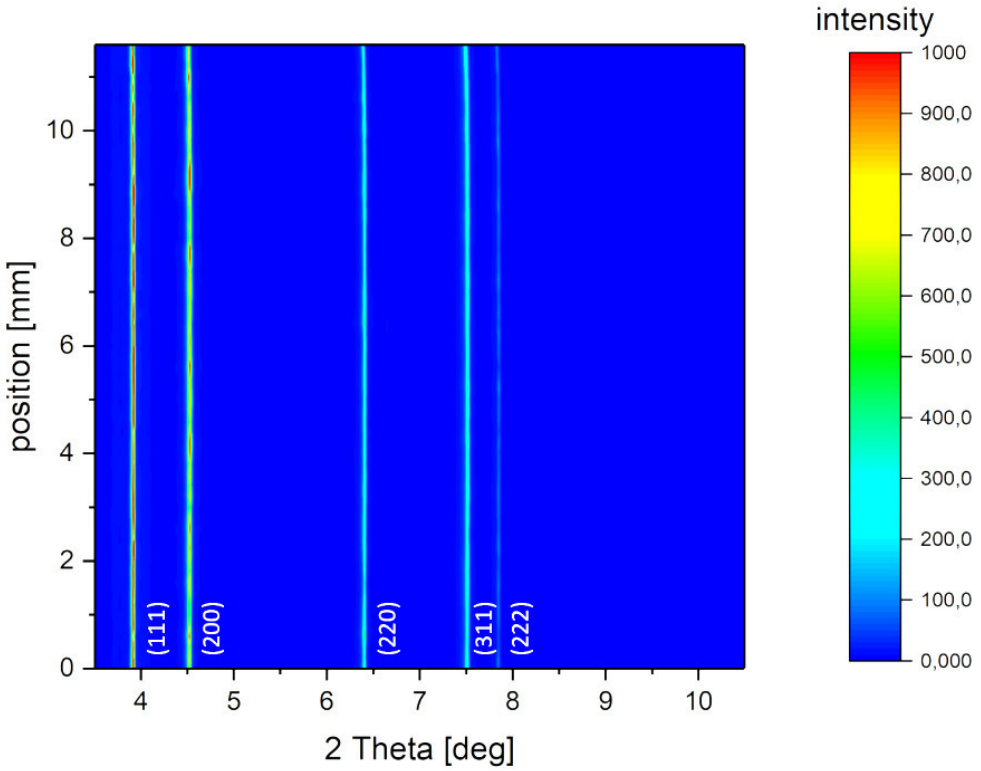

Figure 31: Phase plot from the sample S4 show the evolution of the diffraction peaks *hkl* as a function of the sample height Z.

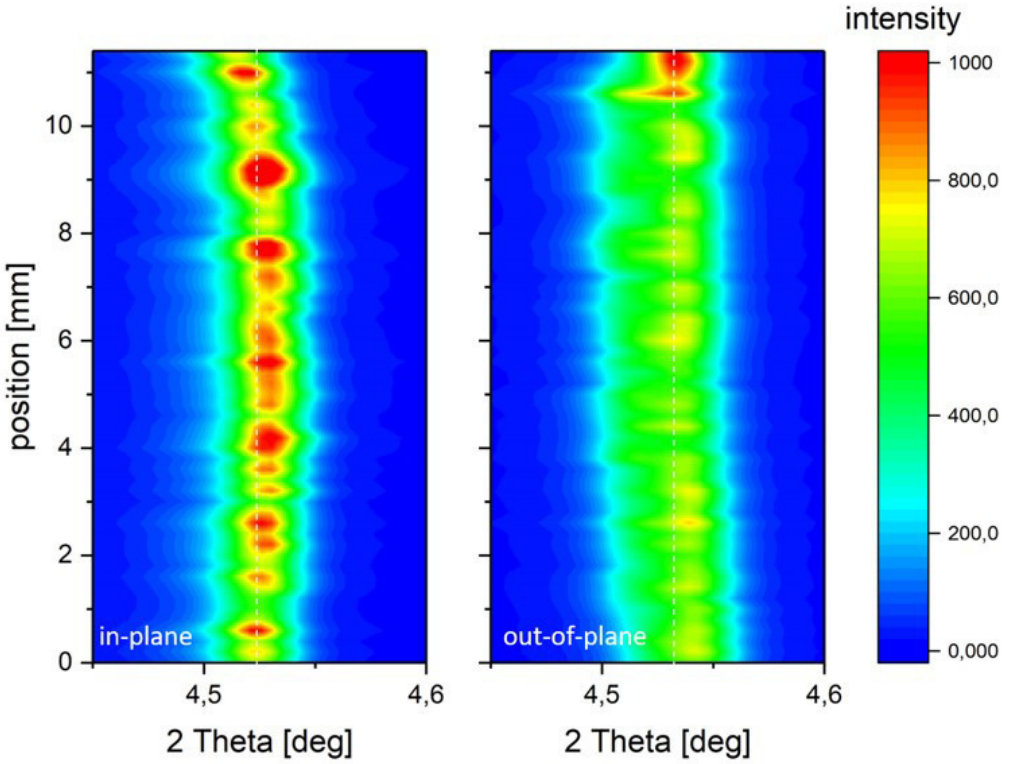

Figure 32: Detail of the Inconel718 200 reflections obtained by in-plane(left) and out-of-plane Debye-Scherer-ring integrations as a function of the sample height. The peak-shift of the in-plane orientation is more pronounced, as the in-plane stresses acting along Y direction are dominant.

4.5.2 Horizontal and vertical stress distributions

Horizontal synchrotron scans of the structures in the distance of 1 mm above the substrate surface were analysed and plotted using *Origin* software [26]. Thus, also for the gradient synchrotron specimens only one specific *VED* was examined. The overlay of the single-parameter structures is presented in Figure 33 and the plots of all gradient structures are illustrated in Figure 34. Except from the 80 µm gradient structure, the horizontal stress distributions are similar for all synchrotron samples.

For the homogenous structures, the parameter set of the sample number 36 (*VED* = 87 J/mm³), showing the highest elongation at fracture A_{max} in the tensile tests, was scanned horizontally. This parameter set revealed in the lowest tensile stresses. The averaged stress at the Y-positions 5.5 to 14.4 mm is ~200 ±51 MPa.

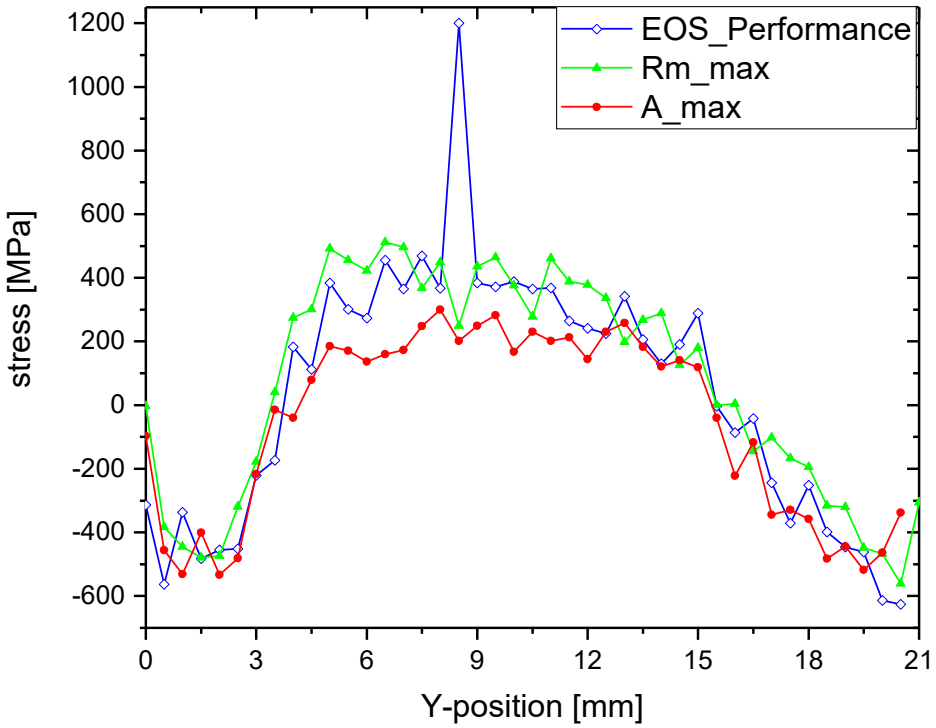

Figure 33: Horizontal stress distributions in Inconel718 structures that were deposited with one constant parameter set. Maximal compressive and tensile stresses are similar for the samples with the layer thickness of 20 µm (green triangles - parameter set of sample number 12) and the standard EOS-performance parameter set (*s* = 40 µm – blue dot-shells), whereas the sample produced with parameter set resulting in the maximal fracture strain (*s*=50 µm – red dots) shows the lowest tensile stress level from all synchrotron samples.

The horizontal stress distribution for the standard EOS-Inconel718-performance parameter set is illustrated by blue dot-shells in Figure 33. Excluding the outliner at the Y-position of 8.5 mm, the mean stress in the region of 5.5 to 14.5 mm is ~317 ±91 MPa.

The synchrotron sample deposited using the homogenous deposition conditions, which were equal to those of the tensile sample number 12 showing the maximal R_m (Figure 25b), revealed the highest tensile residual stress value of ~366 ±104 MPa.

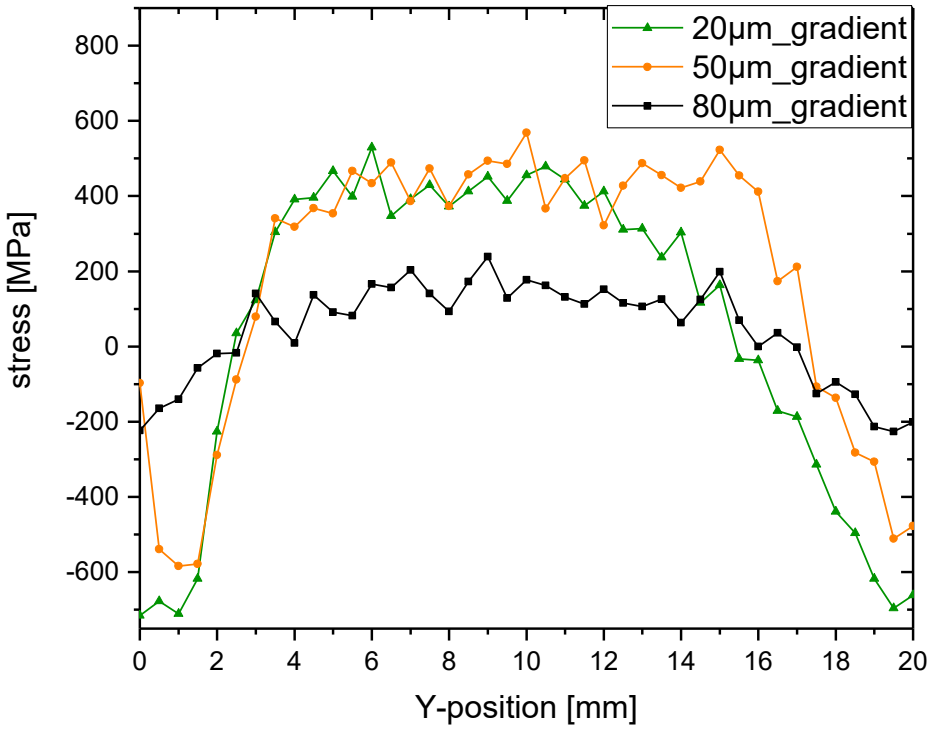

Figure 34: The stress dependencies obtained from the horizontal scanning experiments on Inconel718 gradient structures indicate the insufficient fusion of powder particles in the *s* = 80 µm structure (black squares). The stress distribution in the 20 µm gradient specimen (green triangles) differs from the course of the 50 µm structure (orange dots).

The stress curves from the gradient structures in Figure 34 show differences in their progress and extreme values. Black squares indicate the stress data from the specimen, that was deposited with *s* = 80 µm. It corresponds to the parameter set of sample number 17 (*VED* = 17 J/mm³) Even though this sample shows the minimal value of the residual stresses, this result cannot be taken as benefit because of the poor mechanical properties of the corresponding tensile specimens (cf. Appendix).

The maximum values of the tensile stresses obtained from both gradient structures, that were deposited with 20 µm (green triangles) and 50 µm (orange dots) are similar. The local position at 1mm above the substrate surface corresponds to a *VED* of 69 J/mm³ (sample number 2) for *s* = 20 µm and to a *VED* of 73 J/mm³ (sample number 35) for *s* = 50 µm. The significantly lower tensile residual stress level in the sample deposited with 20 µm layer thickness can be attributed to the more frequent sample remelting during the build-up. Furthermore, compressive stresses at a position of Y = 1mm are highest for the s = 20 µm sample and therefore the absolute change in the stress state (from the compressive to the tensile stress level) is largest from all samples.

Figure 35 presents the vertical stress profiles (collected from the scanning experiments along Z-axis) from the synchrotron specimens, produced with constant energy input over the whole structure height. The initial stress at the surface of the substrate seems to be correlated with the energy input to the first deposited layers - it increases with the increasing *VED*. The course of the three homogenous deposited structures is similar until a Z-position of ~9 mm. Afterwards, the tensile stresses in the specimens that were deposited using the standard EOS-performance parameter set (blue dot-shells) and the parameter set of sample number 36 (red dots; highest value for the strain at fracture in the tensile tests), increase. Residual stresses in the specimen that was deposited with the parameters of sample number 12 (resulting in maximal R_m (green triangles)) stay at the lower level. The probable reason for the stress saturation for Z > 5mm in this sample could be the structure relaxation during the building with 20 µm layer thickness. Tailored optimization of residual stresses in the built-up part would be possible by adjusting the energy densities in the first layers and using higher *VED* in the following layers.

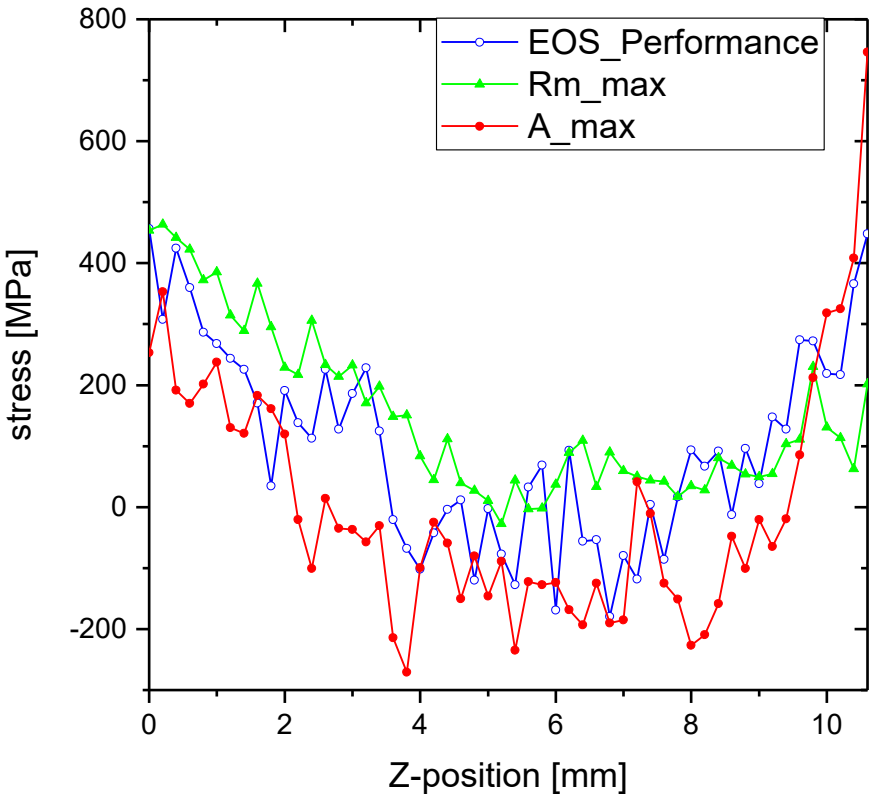

Figure 35: The vertical stress distributions across Inconel718 structures deposited using constant process parameters show a similar course for the standard EOS parameter set (blue dot-shells) and the set that indicated A_{max} (red dots). Stresses in sample number 12 (green triangles) remain relatively constant towards the top end of the structure.

The vertical stress profiles in the synchrotron structures that were produced with a gradient of the energy input are depicted in Figure 36. The results could suggest that the *VED* variation results in a zero stress level at the substrate surface in the sample produced using 20 µm layer thickness. Considering the horizontal stress distribution in

this sample, however, it is clear, that this behaviour originates from the geometrical effect, as it is indicated in Figure 37, where the tensile stresses diminish at the edge of the built structure.

The relaxation of the gradient structure with 50 µm layer thickness towards the surface is the result of incomplete fusion of the powder particles during the SLM. The same is valid for the 80 µm structure. A further validation for these outcomes provide the texture plots that will be presented in the next section.

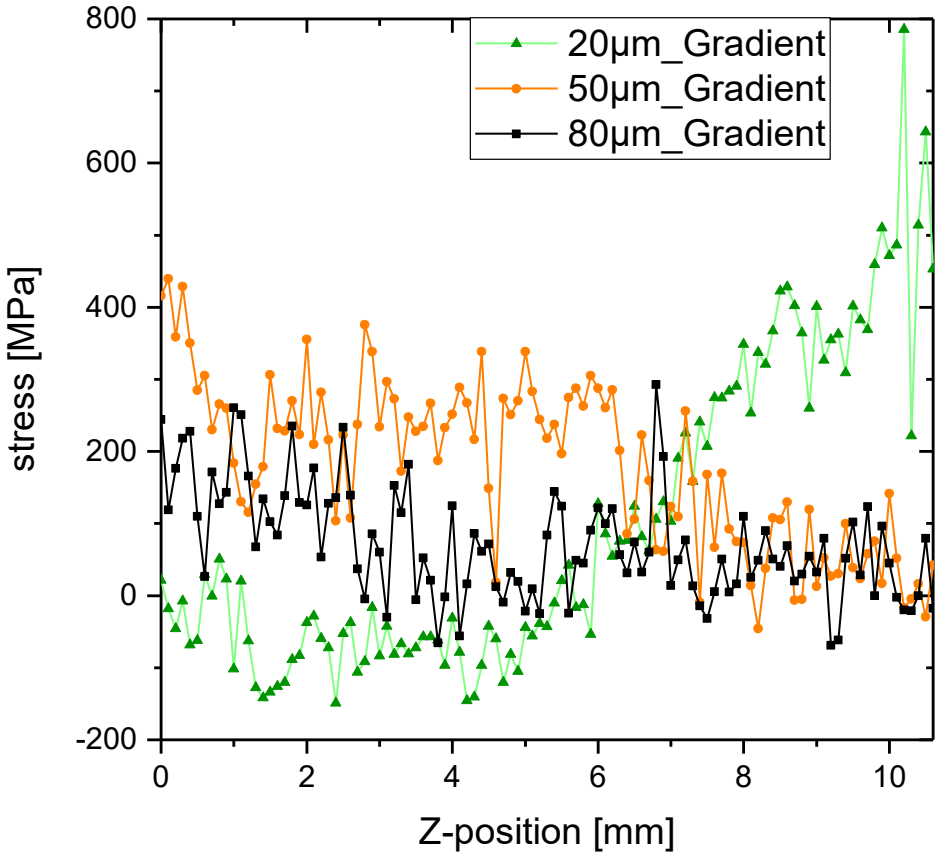

Figure 36: The vertical stress profiles from the gradient structures should be interpreted with respect to texture measurements and horizontal stress profiles.

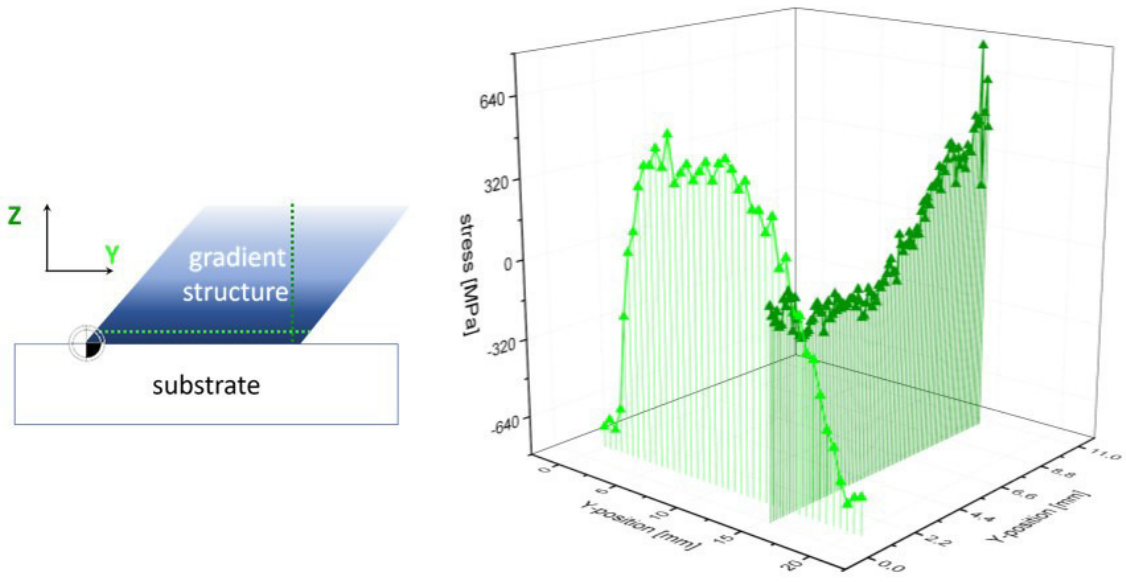

Figure 37: The course of the vertical stress distribution in the gradient structure of specimen S6 (corresponding to the sample produced with 20µm layer thickness in Figure 34) documents the effect of the sample geometry.

4.5.3 Texture characteristics of the synchrotron samples

The occurrence of a texture in solids results in anisotropic physical properties. Figure 38 illustrates the texture plots evaluated for 111 and 200 reflections of the Inconel718 sample, that was built using the standard EOS-Inconel718-performance parameter. The deposition conditions were kept constant during the production of this sample. Taking the stereographic projection of the crystal planes in a cubic structure in account, it can be deduced, that the grains possess <100> fibre texture with respect to the substrate. The texture analysis of the other two homogenously deposited synchrotron geometries revealed comparable results.

Figure 39 illustrates the texture plots for 200 diffraction peaks of the synchrotron samples that were produced with a gradient in the *VED*. The well pronounced texture all over the structure height in Figure 39 a indicates, that all energy levels were high enough to fuse the powder particles. Actually, the energy was even high enough to transfer a sufficient amount to the preceding layers, so that the minor microstructural changes do not coincide with the indicated *VED* levels (cf. minor tick labels on the left side in Figure 39a).

The texture plot of the gradient sample, deposited with the 50 µm layer thickness is presented in Figure 39b. The amount of randomly oriented grains increases with decreasing *VED*. Until the 10^{th} to 11^{th} energy level (corresponding to the *VED* of 26 to 28 J/mm³ and a structure height of 6.9 mm, respectively) a texture is clearly detectable. An energy input below 26 J/mm³ is not sufficient to melt and joint the powder particles in Inconel718.

The texture in the gradient synchrotron sample that was deposited with a *s* of 80 µm is random all over the sample height (Figure 39c). However, the minor visible intensity lines

coincide with the abrupt *VED* changes (cf. Figure 39c). This indicates, that the energy input during deposition did not affect the microstructure of preceding layers significantly.

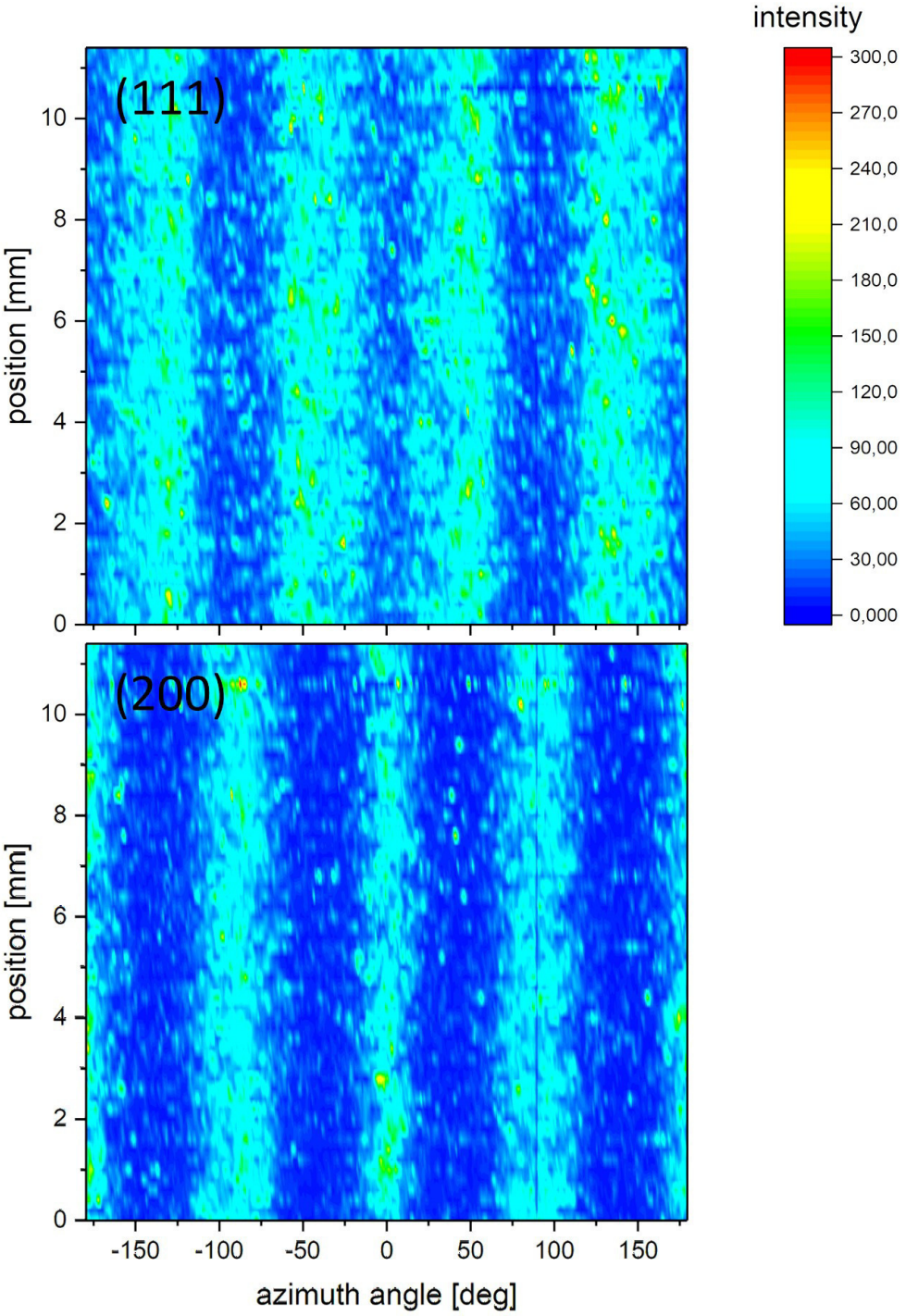

Figure 38: Sample height dependent texture plots indicate the intensity distributions of 111 and 200 diffraction peaks of Inconel718 sample and document the presence of <100> fibre texture.

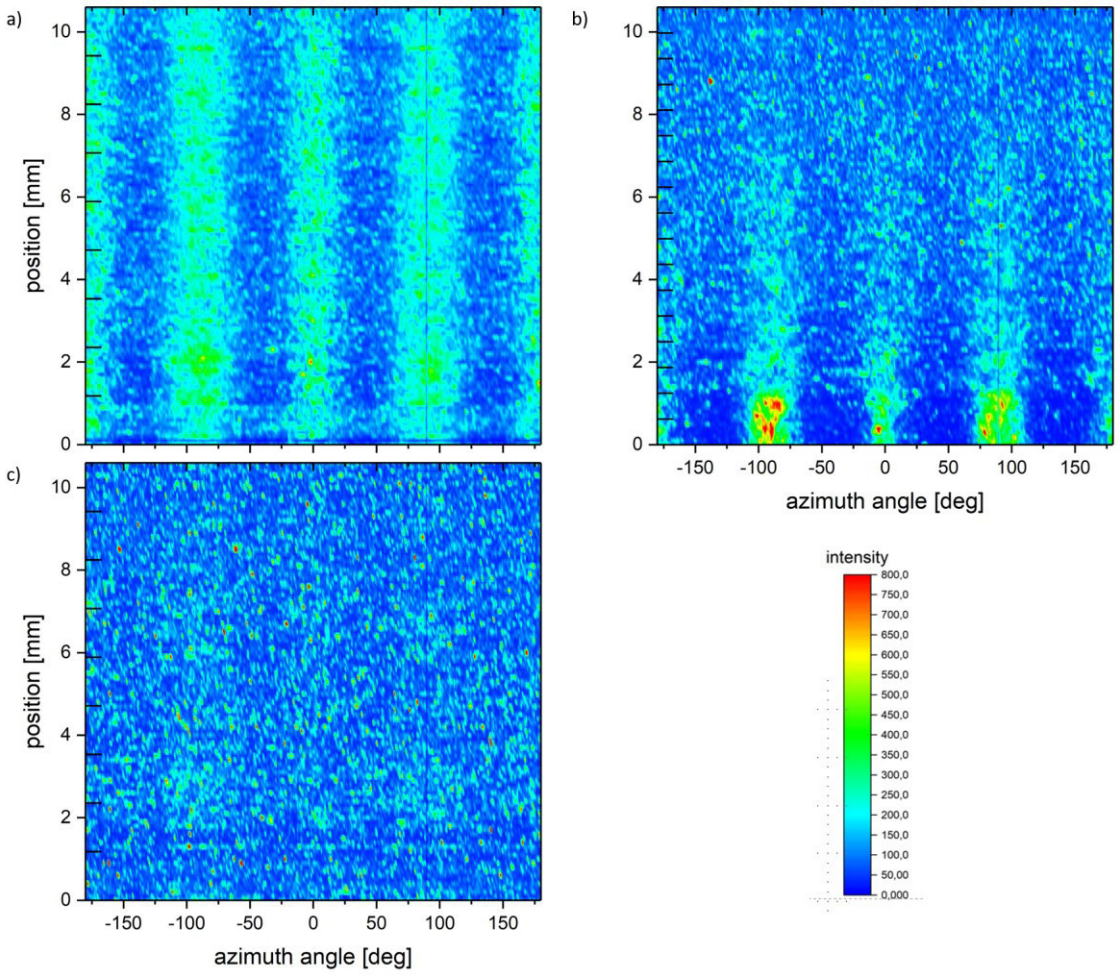

Figure 39: Texture plots of 200 diffraction peaks of the structures that were deposited with energy gradients and varying layer thicknesses of a) 20 µm, b) 50 µm and c) 80 µm. The degree of the preferred orientation depends on the energy input. The minor inner tick labels at the left edge of the images indicate the thresholds of the *VED* changes.

4.6 EBSD and EDX analysis

EBSD analysis were performed at the gradient-synchrotron specimen that was produced with a *s* of 20 µm, to understand the formation of the texture in the built structures. Figure 40 presents an SEM-overview image of the interface between the substrate and the built-up structure. For a selected sample region next to a HV indent imprint, an inverse pole figure was calculated. The microstructure of the substrate indicates, that the material was tempered to set the properties of Inconel718. The inverse pole figure map reveals, that the grains in the substrate are oriented randomly. The chemistry of precipitates at the grain boundaries was determined by EDX. These precipitates are Cr-carbides.

During the deposition of the first layer, some crystallites of the build-up adopted the orientations of the substrate grains. One example of a cube on cube epitaxy is labelled by B in the inverse pole map, showing a presence of a circular substrate grain and an elongated layer grain. In general, the orientation of the grains in the near-interface region is apparently random. Within a transition zone T, the grain orientation gradually changes. The width of T is ~100 µm. This thickness corresponds to a building height of approximately five layers.

Figure 41 presents an overlay of the inverse pole map and the EBSD image at a distance of about 600 µm from the substrate. This analysis approves the results of the synchrotron texture evaluation. The built-up shows a <100> texture. As the energy input is high enough to partially remelt the preceding layers, an epitaxial grain growth over several deposited layers is possible (see Figure 42).

Due to the partial remelting of the preceding layers, diffusion processes are activated. As Figure 42 depicts, these effects lead to the microstructure coarsening and furthermore to the segregation of Cb at the sub-grain boundaries. The Cb-segregation was again characterized by an EDX microanalysis.

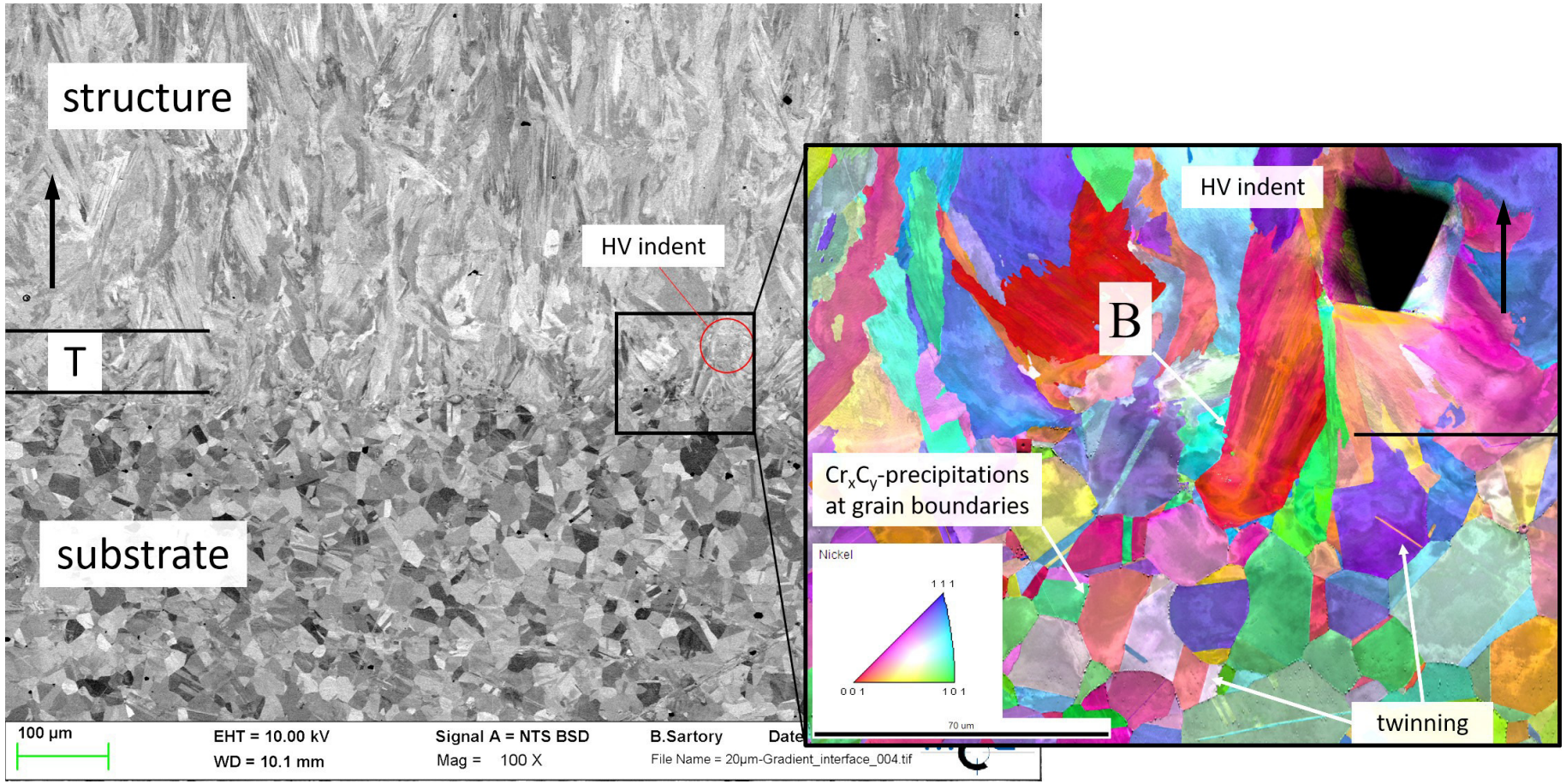

Figure 40: EBSD image and the corresponding inverse pole figure map of the interface between Inconel718 substrate and deposited structure in "as-built" condition. Within a transformation zone T, the orientation of the grains changes from random in the substrate to <100>-textured in the deposited structure. The building direction is indicated by arrows at the sides of the micrographs.

Figure 41: Overlay of an EBSD image with the inverse pole map of the SLM structure. If the energy input is high enough, large grains will grow epitaxially over several deposited layers. The building direction is indicated by an arrow.

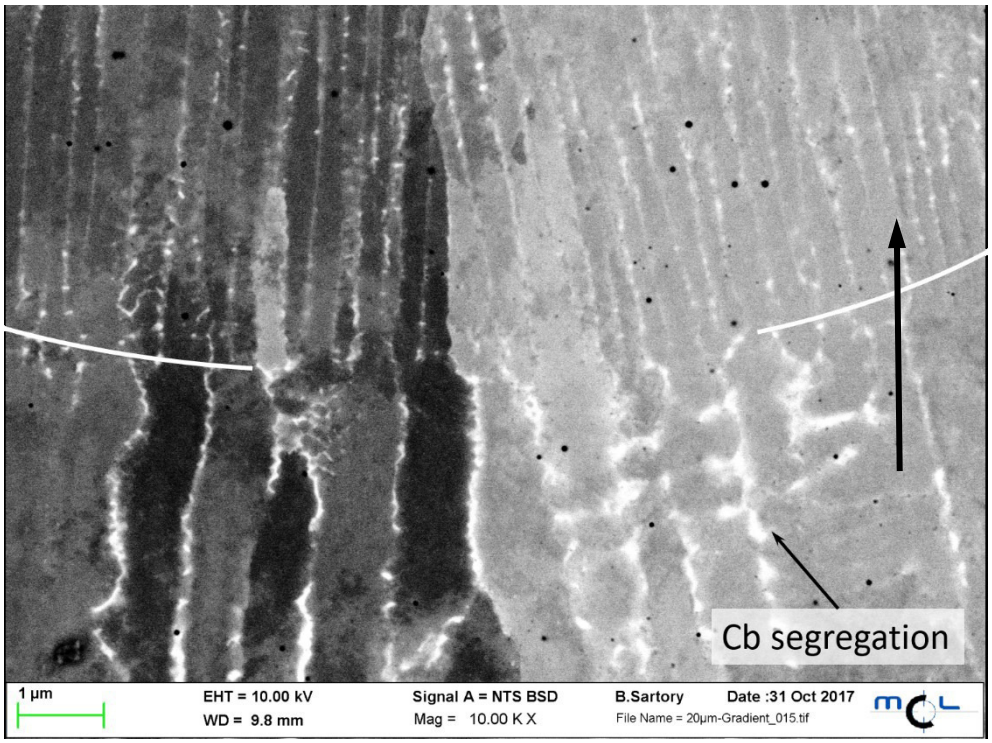

Figure 42: EBSD image of a single layer junction recorded with a magnification of 10.000 times. Cb segregates at low angle grain boundaries in the preceding layers. The interface between the two layers is marked at the sides of the image by white curves. The building direction is indicated by an arrow.

4.7 Correlation of the results

A comparison of the results from tensile experiments, texture analysis, HV0.3 hardness measurements and microscopic images opens the possibility to correlate the applied process conditions with the recorded mechanical data as well as microstructural parameters. Figure 43 provides an example of the structure-property correlation for the synchrotron sample S6 (deposited with the layer thickness of 20 µm).

The texture development is only slightly influenced by the changes in the deposition parameters, namely in *VED*. The porosity and materials' density depend obviously on the parameter combination during the SLM process. By applying lower *VEDs*, the sample porosity increases. The importance of the variation of single process parameters is clearly evident in the region with the constant *VED* of 52 J/mm³, in the center of the gradual structure from Figure 43. While the *VED* of 52 J/mm³ is constant for these three parameter sets, mechanical properties and porosity are different. The reason for this behavior is the variation of the laser power and scanning speed during the growth within these three parameter sets. This results emphasis the importance of the systematical determination of single process parameters by statistical analysis methods like the DoE.

The strain at fracture *A* decreases with the decreasing *VED*. This observation can be explained by the differences in the microstructure of the particular built-ups. The increase in *VED* results in microstructure coarsening, which in turn allows for the formation and movement of dislocations in large grains and finally contributes primarily to the sample deformability.

The distribution of hardness values shows clearly the differences between the substrate ($HV_{0.3}$ = 178 ±4) and the SLM fabricated structure ($HV_{0.3}$ = 300 ±13). The apparent hardness decrease towards the sample surface is caused by the sample porosity. These statistical outliners for the HV-values represent therefore invalid measurement points. In the region of low *VED*, the minimum distance to neighbored pores could not be taken in account as the porosity in these regions was too high.

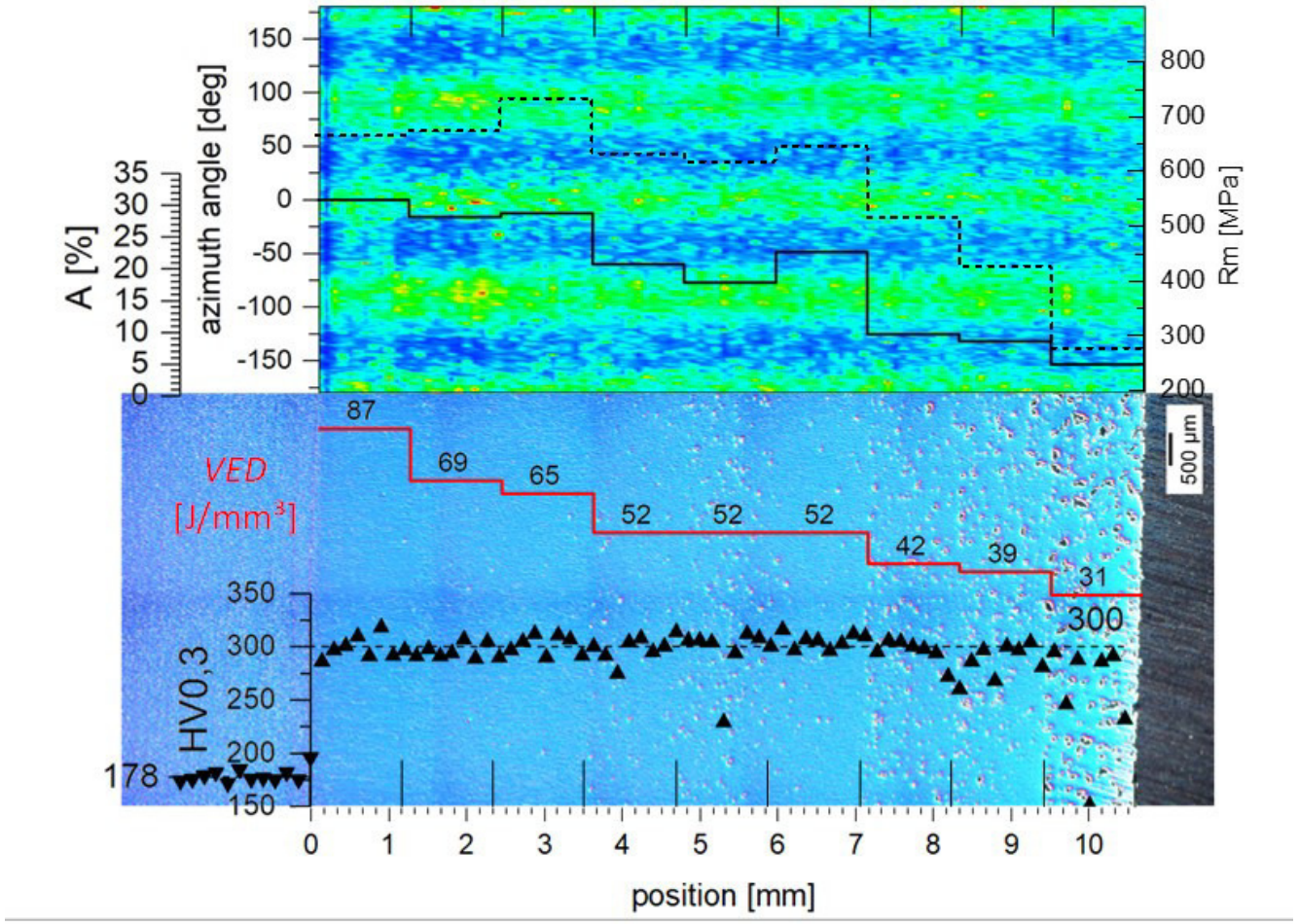

Figure 43: Combined display of tensile test results (strain at fracture *A* in continuous black line and ultimate tensile strength R_m in dashed black line), Inconel718 200 diffraction peak texture analysis, hardness values and optical microscopy for the gradual sample deposited using a *VED*. The sample was produced using a constant layer thickness *s* = 20 µm, whereas laser power *P* and scanning velocity *v* were varied during the deposition.

5 Conclusion

In this thesis, a variety of Inconel718 samples produced using SLM were characterized using XRD, SEM, EBSD, EDX, OM and mechanical tests. The experimental data of microstructure, residual stresses and mechanical properties were correlated with the SLM process conditions.

41 process parameter combinations were developed derived on the EOS standard parameter sets for Inconel718 using a 3^k full factorial design of experiments with one-dimensional extensions. The laser power *P*, the scanning velocity *v* and the layer thickness *s* were selected as experiment factors.

The developed parameter combinations were applied to manufacture three replicate series of micro-tensile samples. The analysis of the surfaces' roughnesses and the performed tensile tests in combination with the microstructural examinations indicated a complex correlation between the process parameters and the specimen functional properties.

Surfaces roughnesses were optimized to mean values of ~14µm and for vertical and 45°-upskin oriented surfaces and to values of 19 µm for 45°-downskin oriented surfaces. A maximal ultimate tensile strength of ~670 MPa and a strain at fracture of up to ~33.5 % were obtained in the particular as-built structures.

The results from the tensile experiments were used to design the samples for further synchrotron XRD experiments. The analysis of homogeneously deposited and VED-gradient built-up structures allowed for the determination of phase and texture plots as well as residual stress profiles. These parameters were correlated with the sample microstructure and hardness.

Finally, it was shown, that the deposition conditions during the SLM process can be purposefully selected to design the microstructures locally and thus influence the overall as well as local mechanical properties. In order words, the correlation of the experimental data allowed the understanding of the influence of the specific process parameters on the mechanical properties, the microstructure, the residual stress distributions and the surface quality. This multi-parameter study based on a variety of experimental techniques and applied process conditions demonstrate that it is possible to perform knowledge-based design of the functional properties of SLM structures.

Bibliography

[1] DIN, *DIN 8580:2003-09 - Fertigungsverfahren - Begriffe, Einteilung*. 2003.

[2] I. Gibson, D. Rosen, and B. Stucker, *Additive Manufacturing Technologies*. 2015.

[3] M. Greulich, “Entwicklung eines metallischen Pulversytems für die Anwendung im Lasersinter-Verfahren,” Technische Universität Clausthal, 1997.

[4] A. Basak and S. Das, “Epitaxy and Microstructure Evolution in Metal Additive Manufacturing,” *Annu. Rev. Mater. Res.*, vol. 46, no. 1, pp. 125–149, 2016.

[5] D. Gu, *Laser additive manufacturing of high-performance materials*. 2015.

[6] H. Göhler *et al.*, “Metallic hollow sphere structures - status and outlook,” *Proc. CELLMAT 2012*, no. 1, pp. 1–9, 2012.

[7] M. Berkmanns, Joachim; Färber, “Facts About Laser Technology.”

[8] L. N. Carter, C. Martin, P. J. Withers, and M. M. Attallah, “The influence of the laser scan strategy on grain structure and cracking behaviour in SLM powder-bed fabricated nickel superalloy,” *J. Alloys Compd.*, vol. 615, pp. 338–347, 2014.

[9] K. G. Prashanth, S. Scudino, and J. Eckert, “Defining the tensile properties of Al-12Si parts produced by selective laser melting,” *Acta Mater.*, vol. 126, pp. 25–35, 2017.

[10] K. Prashanth, L. Löber, H.-J. Klauss, U. Kühn, and J. Eckert, “Characterization of 316L Steel Cellular Dodecahedron Structures Produced by Selective Laser Melting,” *Technologies*, vol. 4, no. 4, p. 34, 2016.

[11] O. S. Es-Said, J. Foyos, R. Noorani, M. Mendelson, R. Marloth, and B. A. Pregger, “Effect of Layer Orientation on Mechanical Properties of Rapid Prototyped Samples,” *Mater. Manuf. Process.*, vol. 15, no. 1, pp. 107–122, 2000.

[12] S. M. Corporation, “INCONEL ® Alloy 718,” pp. 1–28, 2007.

[13] R. C. Reed, *The Superalloys Fundamentals and Applications*. 2006.

[14] M. Inc., “Minitab® Software,” 2017. [Online]. Available: www.minitab.com.

[15] C. Turk, “Ausscheidungsverhalten der Ni-Basis-Superlegierung 718,” Montanuniversität Leoben, Leoben, 2012.

[16] G. S. Schajer, *Practical Residual Stress Measurement Methods*. 2013.

[17] E. F. Bradley, *Superalloys - a technical guide*. ASM International, 1988.

[18] Bürgel, *Handbuch Hochtemperatur- Werkstofftechnik*, vol. 53, no. 9. 2013.

[19] U. Cihak, “Characterisation of Residual Stresses using Neutron Diffraction and Finite Element Simulation,” Montanuniversität Leoben, 2007.

[20] W. Rasband, “ImageJ,” *U. S. Natl. Institutes Heal. Bethesda, Maryland, USA*, p. //imagej.nih.gov/ij/, 2012.

[21] “EOS_IN718.pdf.” EOS GmbH, Krailling, München, 2014.

[22] M. Sadowski, L. Ladani, W. Brindley, and J. Romano, “Optimizing quality of additively manufactured Inconel 718 using powder bed laser melting process,” *Addit. Manuf.*, vol. 11, pp. 60–70, 2016.

[23] EPMA, “Introduction to Additive Manufacturing Technology,” *Epma*, p. 42, 2013.

[24] W. C. Liu, M. Yao, Z. L. Chen, and S. G. Wang, “Niobium segregation in Inconel 718,” *J. Mater. Sci.*, vol. 34, no. 11, pp. 2583–2586, 1999.

[25] S. Klein, M. Staring, K. Murphy, M. a. Viergever, and J. Pluim, “<emphasis emphasistype=‘mono’>elastix</emphasis>: A Toolbox for Intensity-Based Medical Image Registration,” *IEEE Trans. Med. Imaging*, vol. 29, no. 1, pp. 196–

205, 2010.

[26] OriginLab Corp., “OriginPro 2017G.” OriginLab Corporation, Northampton, MA, 2017.

Appendix

Sample nr. 1	***P* = 75 W**	***v* = 720 mm/min**	***s* = 20 µm**	***VED* = 52 J/mm³**

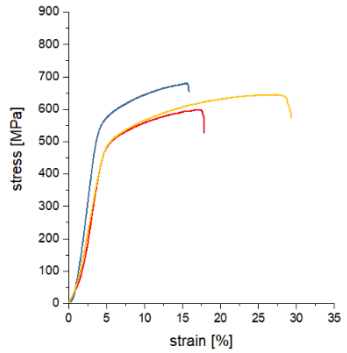

R_m	618 MPa
$R_{p0,2}$	462 MPa
A	17.8 %
R_{a_ver}	17 µm
R_{a_up}	22 µm
R_{a_down}	22 µm

Sample nr. 2	***P* = 100 W**	***v* = 720 mm/min**	***s* = 20 µm**	***VED* = 52 J/mm³**

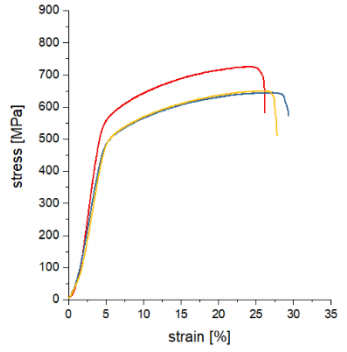

R_m	674 MPa
$R_{p0,2}$	474 MPa
A	28.2 %
R_{a_ver}	18 µm
R_{a_up}	16 µm
R_{a_down}	24 µm

Sample nr. 3	***P* = 125 W**	***v* = 720 mm/min**	***s* = 20 µm**	***VED* = 87 J/mm³**

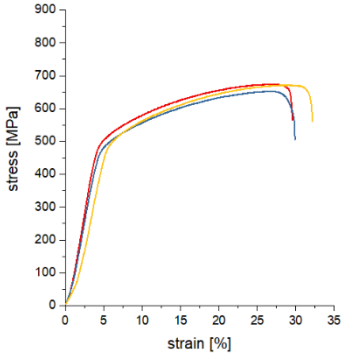

R_m	674 MPa
$R_{p0,2}$	474 MPa
A	30.9 %
R_{a_ver}	18 µm
R_{a_up}	14 µm
R_{a_down}	31 µm

Sample nr. 4	***P* = 75 W**	***v* = 720 mm/min**	***s* = 50 µm**	***VED* = 21 J/mm³**

R_m	177 MPa
$R_{p0,2}$	162 MPa
A	4.9 %
R_{a_ver}	29 µm
R_{a_up}	37 µm
R_{a_down}	40 µm

Sample nr. 5	***P* = 100 W**	***v* = 720 mm/min**	***s* = 50 µm**	***VED* = 28 J/mm³**

R_m	337 MPa
$R_{p0,2}$	196 MPa
A	6.2 %
R_{a_ver}	23 µm
R_{a_up}	33 µm
R_{a_down}	34 µm

Sample nr. 6	***P* = 125 W**	***v* = 720 mm/min**	***s* = 50 µm**	***VED* = 35 J/mm³**

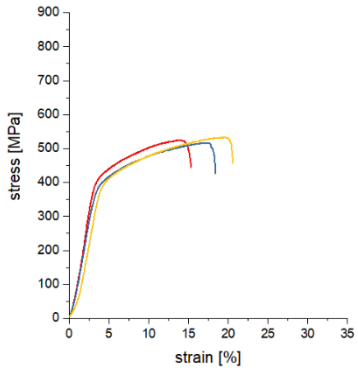

R_m	525 MPa
$R_{p0,2}$	372 MPa
A	18.3 %
R_{a_ver}	19 µm
R_{a_up}	18 µm
R_{a_down}	38 µm

Sample nr. 7	***P* = 75 W**	***v* = 720 mm/min**	***s* = 80 µm**	***VED* = 13 J/mm³**

R_m	154 MPa
$R_{p0,2}$	143 MPa
A	4.9 %
R_{a_ver}	25 µm
R_{a_up}	28 µm
R_{a_down}	35 µm

Sample nr. 8	*P* = 100 W	*v* = 720 mm/min	*s* = 80 µm	*VED* = 17 J/mm³

R_m	322 MPa
$R_{p0,2}$	208 MPa
A	5.5 %
R_{a_ver}	27 µm
R_{a_up}	27 µm
R_{a_down}	39 µm

Sample nr. 9	*P* = 125 W	*v* = 720 mm/min	*s* = 80 µm	*VED* = 22 J/mm³

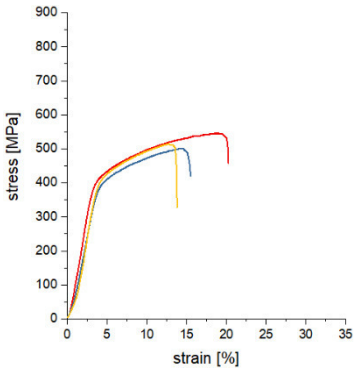

R_m	521 MPa
$R_{p0,2}$	371 MPa
A	16.9 %
R_{a_ver}	20 µm
R_{a_up}	15 µm
R_{a_down}	42 µm

Sample nr. 10	*P* = 75 W	*v* = 960 mm/min	*s* = 20µm	*VED* = 39 J/mm³

R_m	428 MPa
$R_{p0,2}$	364 MPa
A	8.6 %
R_{a_ver}	21 µm
R_{a_up}	21 µm
R_{a_down}	23 µm

Sample nr. 11	*P* = 100 W	*v* = 960 mm/min	*s* = 20µm	*VED* = 52 J/mm³

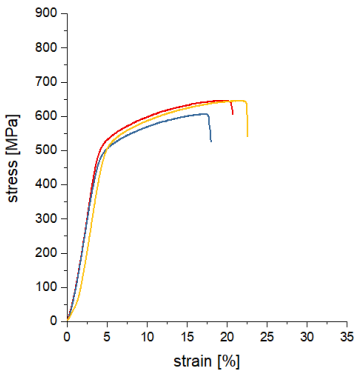

R_m	634 MPa
$R_{p0,2}$	470 MPa
A	20.7 %
R_{a_ver}	19 µm
R_{a_up}	17 µm
R_{a_down}	24 µm

Sample nr. 12	***P* = 125 W**	***v* = 960 mm/min**	***s* = 20 µm**	***VED* = 65 J/mm³**

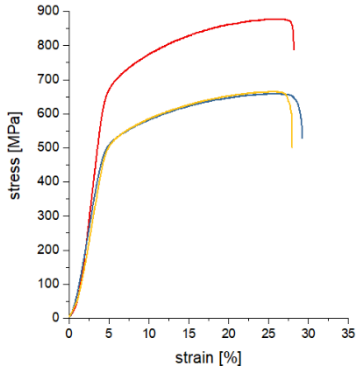

R_m	734 MPa
$R_{p0,2}$	523 MPa
A	28.7 %
R_{a_ver}	17 µm
R_{a_up}	25 µm
R_{a_down}	26 µm

Sample nr. 13	***P* = 75 W**	***v* = 960 mm/min**	***s* = 50 µm**	***VED* = 16 J/mm³**

R_m	62 MPa
$R_{p0,2}$	27 MPa
A	8.4 %
R_{a_ver}	25 µm
R_{a_up}	43 µm
R_{a_down}	30 µm

Sample nr. 14	***P* = 100 W**	***v* = 960 mm/min**	***s* = 50µm**	***VED* = 21 J/mm³**

R_m	180 MPa
$R_{p0,2}$	161 MPa
A	7.7 %
R_{a_ver}	30 µm
R_{a_up}	34 µm
R_{a_down}	36 µm

Sample nr. 15	***P* = 125 W**	***v* = 960 mm/min**	***s* = 50µm**	***VED* = 26 J/mm³**

R_m	357 MPa
$R_{p0,2}$	115 MPa
A	6.3 %
R_{a_ver}	29 µm
R_{a_up}	28 µm
R_{a_down}	35 µm

Sample nr. 16	***P* = 75 W**	***v* = 960 mm/min**	***s* =80 µm**	***VED* = 10 J/mm³**

R_m	45 MPa
$R_{p0,2}$	5 MPa
A	5.3%
R_{a_ver}	41 µm
R_{a_up}	42 µm
R_{a_down}	28 µm

Sample nr. 17	***P* = 100 W**	***v* = 960 mm/min**	***s* = 80 µm**	***VED* = 13 J/mm³**

R_m	177 MPa
$R_{p0,2}$	114 MPa
A	5.5 %
R_{a_ver}	27 µm
R_{a_up}	33 µm
R_{a_down}	31 µm

Sample nr. 18	***P* = 125 W**	***v* = 960 mm/min**	***s* = 80µm**	***VED* = 16 J/mm³**

R_m	355 MPa
$R_{p0,2}$	225 MPa
A	6.2 %
R_{a_ver}	26 µm
R_{a_up}	19 µm
R_{a_down}	31 µm

Sample nr. 19	***P* = 75 W**	***v* = 1200 mm/min**	***s* = 20µm**	***VED* = 31 J/mm³**

R_m	278 MPa
$R_{p0,2}$	248 MPa
A	5.0 %
R_{a_ver}	20 µm
R_{a_up}	20 µm
R_{a_down}	23 µm

Sample nr. 20	***P* = 100 W**	***v* = 1200 mm/min**	***s* = 20 µm**	***VED* = 42 J/mm³**

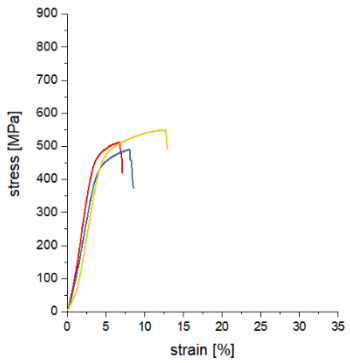

R_m	517 MPa
$R_{p0,2}$	420 MPa
A	9.7 %
R_{a_ver}	24 µm
R_{a_up}	23 µm
R_{a_down}	µm

Sample nr. 21	***P* = 120 W**	***v* = 1200 mm/min**	***s* = 20 µm**	***VED* = 52 J/mm³**

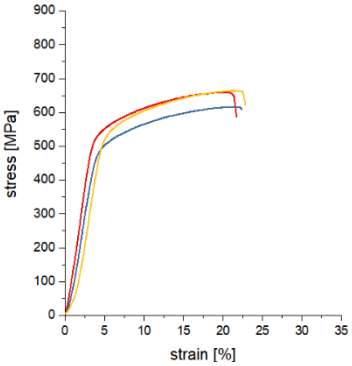

R_m	647 MPa
$R_{p0,2}$	468 MPa
A	22.7 %
R_{a_ver}	19 µm
R_{a_up}	20 µm
R_{a_down}	38 µm

Sample nr. 22	***P* = 75 W**	***v* = 1200 mm/min**	***s* = 50µm**	***VED* = 13 J/mm³**

R_m	17 MPa
$R_{p0,2}$	5 MPa
A	5.0 %
R_{a_ver}	26 µm
R_{a_up}	34 µm
R_{a_down}	38 µm

Sample nr. 23	***P* = 100 W**	***v* = 1200 mm/min**	***s* = 50µm**	***VED* = 17 J/mm³**

R_m	80 MPa
$R_{p0,2}$	35 MPa
A	5.7 %
R_{a_ver}	28 µm
R_{a_up}	34 µm
R_{a_down}	38 µm

Sample nr. 24	***P* = 125W**	***v* = 1200 mm/min**	***s* = 50 µm**	***VED* = 21 J/mm³**

R_m	199 MPa
$R_{p0,2}$	184 MPa
A	5.6 %
R_{a_ver}	25 µm
R_{a_up}	33 µm
R_{a_down}	36 µm

Sample nr. 25	***P* = 75 W**	***v* = 1200 mm/min**	***s* = 80 µm**	***VED* = 8 J/mm³**

R_m	15 MPa
$R_{p0,2}$	5 MPa
A	5.1 %
R_{a_ver}	32 µm
R_{a_up}	45 µm
R_{a_down}	55 µm

Sample nr. 26	***P* = 100 W**	***v* = 1200 mm/min**	***s* = 80µm**	***VED* = 10 J/mm³**

R_m	64 MPa
$R_{p0,2}$	5 MPa
A	6.1 %
R_{a_ver}	29 µm
R_{a_up}	33µm
R_{a_down}	27 µm

Sample nr. 27	***P* = 125 W**	***v* = 1200 mm/min**	***s* = 80µm**	***VED* = 13 J/mm³**

R_m	194 MPa
$R_{p0,2}$	176 MPa
A	9.5 %
R_{a_ver}	28 µm
R_{a_up}	27 µm
R_{a_down}	29 µm

<table>
<tr><td>Sample nr. 28</td><td>P = 25W</td><td>v = 960 mm/min</td><td>s = 50 µm</td><td>VED = 5 J/mm³</td></tr>
<tr><td colspan="5">No sample production possible due to too low VED.</td></tr>
<tr><td>Sample nr. 29</td><td>P = 50W</td><td>v = 960 mm/min</td><td>s = 50 µm</td><td>VED =10 J/mm³</td></tr>
<tr><td colspan="2"> </td><td colspan="3">No test results available as the specimens broke by touching.</td></tr>
<tr><td>Sample nr. 30</td><td>P = 150 W</td><td>v = 960 mm/min</td><td>s = 50 µm</td><td>VED = 31 J/mm³</td></tr>
<tr><td colspan="2"> </td><td colspan="2"> 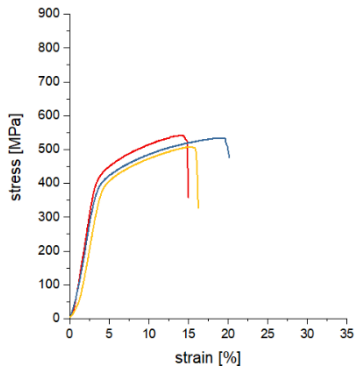
</td><td>
<table>
<tr><td>R_m</td><td>528 MPa</td></tr>
<tr><td>$R_{p0,2}$</td><td>375 MPa</td></tr>
<tr><td>A</td><td>17.4 %</td></tr>
<tr><td>R_{a_ver}</td><td>18 µm</td></tr>
<tr><td>R_{a_up}</td><td>29 µm</td></tr>
<tr><td>R_{a_down}</td><td>31 µm</td></tr>
</table>
</td></tr>
<tr><td>Sample nr. 31</td><td>P = 175 W</td><td>v = 960 mm/min</td><td>s = 50µm</td><td>VED = 36 J/mm³</td></tr>
<tr><td colspan="2"> </td><td colspan="2"> 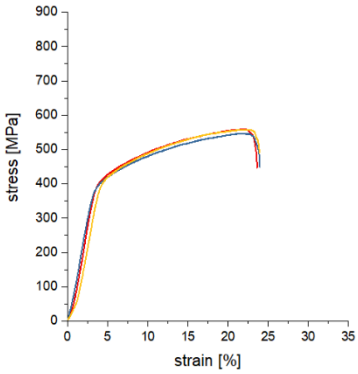
</td><td>
<table>
<tr><td>R_m</td><td>554 MPa</td></tr>
<tr><td>$R_{p0,2}$</td><td>378 MPa</td></tr>
<tr><td>A</td><td>24.2 %</td></tr>
<tr><td>R_{a_ver}</td><td>17 µm</td></tr>
<tr><td>R_{a_up}</td><td>26µm</td></tr>
<tr><td>R_{a_down}</td><td>32 µm</td></tr>
</table>
</td></tr>
</table>

Sample nr. 32	*P* = 200 W	*v* = 960 mm/min	*s* = 50 µm	*VED* = 42 J/mm³

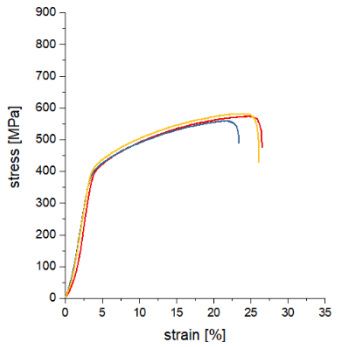

R_m	571 MPa
$R_{p0,2}$	385 MPa
A	25.6 %
R_{a_ver}	17 µm
R_{a_up}	39 µm
R_{a_down}	19 µm

Sample nr. 33	*P* = 250 W	*v* = 960 mm/min	*s* = 50 µm	*VED* = 52 J/mm³

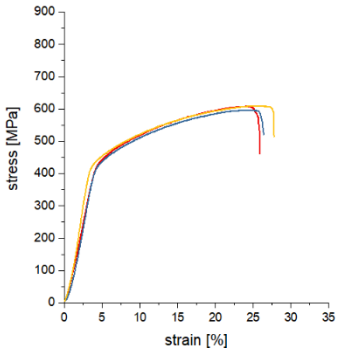

R_m	605 MPa
$R_{p0,2}$	407 MPa
A	27.0 %
R_{a_ver}	19 µm
R_{a_up}	43 µm
R_{a_down}	49 µm

Sample nr. 34	*P* = 300 W	*v* = 960 mm/min	*s* = 50 µm	*VED* = 63 J/mm³

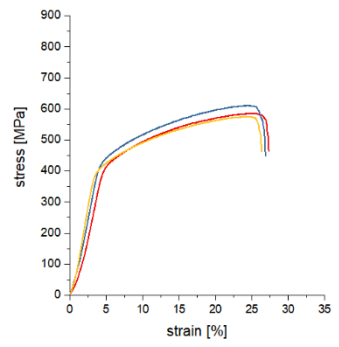

R_m	588 MPa
$R_{p0,2}$	397 MPa
A	27.2 %
R_{a_ver}	19 µm
R_{a_up}	19 µm
R_{a_down}	28 µm

Sample nr. 35	*P* = 350 W	*v* = 960 mm/min	*s* = 50 µm	*VED* = 73 J/mm³

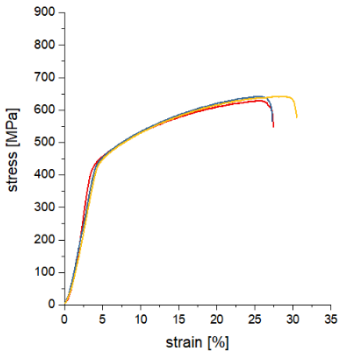

R_m	637 MPa
$R_{p0,2}$	422 MPa
A	28.7 %
R_{a_ver}	14 µm
R_{a_up}	18 µm
R_{a_down}	52 µm

Sample nr. 36	*P* = 100 W	*v* = 240 mm/min	*s* = 50 µm	*VED* = 83 J/mm³

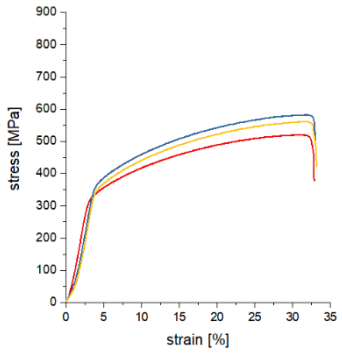

R_m	555 MPa
$R_{p0,2}$	337 MPa
A	33.5 %
R_{a_ver}	18 µm
R_{a_up}	43 µm
R_{a_down}	51 µm

Sample nr. 37	*P* = 100 W	*v* = 480 mm/min	*s* = 50 µm	*VED* = 42 J/mm³

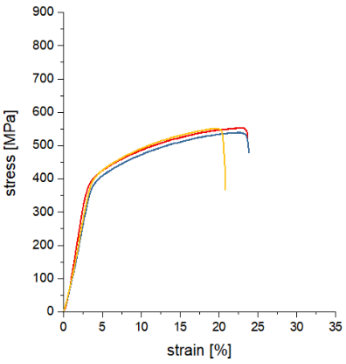

R_m	548 MPa
$R_{p0,2}$	371 MPa
A	23.0 %
R_{a_ver}	22 µm
R_{a_up}	34 µm
R_{a_down}	36 µm

Sample nr. 38	*P* = 100 W	*v* = 1440 mm/min	*s* = 50 µm	*VED* = 14 J/mm³

R_m	92 MPa
$R_{p0,2}$	16 MPa
A	5.0 %

Sample nr. 39	*P* = 100 W	*v* = 1680 mm/min	*s* = 50 µm	*VED* = 12 J/mm³

No test results available as the specimens broke by touching.

Sample nr. 40	***P* = 100 W**	***v* = 1920 mm/min**	***s* = 50 µm**	***VED* = 10 J/mm³**
	No test results available as the specimens broke by touching.			
Sample nr. 41	***P* = 100 W**	***v* = 2880 mm/min**	***s* = 50 µm**	***VED* = 7 J/mm³**
	No test results available as the specimens broke by touching.			

substrate

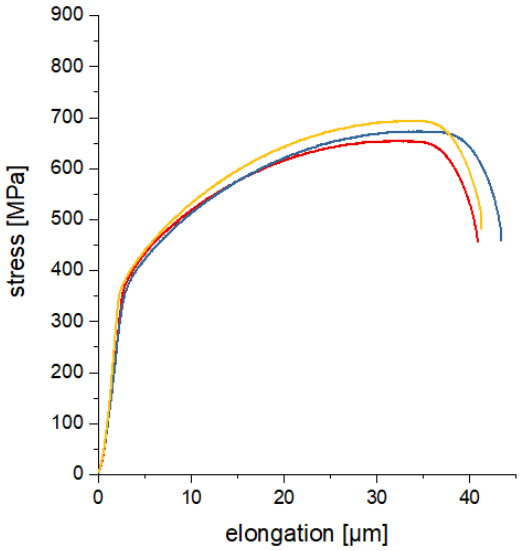

R_m	674 MPa
$R_{p0.2}$	354 MPa
A	41.8 %
E	190 GPa